FLUMINENSE FEDERAL UNIVERSITY
INSTITUTE OF GEOSCIENCES
DEPARTMENT OF GEOLOGY AND GEOPHYSICS
MASTER'S PROGRAM IN OCEAN AND EARTH DYNAMICS

TESS BOSS

IDENTIFICATION OF IGNEOUS BODIES USING SPECTRAL DECOMPOSITION IN THE PRE-SALT INTERVAL OF THE MERO FIELD, SANTOS BASIN

Niterói, RJ
2025

TESS BOSS

IDENTIFICATION OF IGNEOUS BODIES USING SPECTRAL DECOMPOSITION IN THE PRE-SALT INTERVAL OF THE MERO FIELD, SANTOS BASIN

A dissertation submitted to the Graduate Program in Ocean and Earth Dynamics in partial fulfillment of the requirements for the degree of Master of Science in the field of Geology and Geophysics.

Advisor: Prof. Dr. Wagner Moreira Lupinacci

Niterói, RJ
2025

TESS BOSS

IDENTIFICATION OF IGNEOUS BODIES USING SPECTRAL DECOMPOSITION IN THE PRE-SALT INTERVAL OF THE MERO FIELD, SANTOS BASIN

A dissertation submitted to the Graduate Program in Ocean and Earth Dynamics in partial fulfillment of the requirements for the degree of Master of Science in the field of Geology and Geophysics.

Approved on December 16th, 2025.

EXAMINING COMMITTEE

_____

Ph. D. Leonardo Costa de Oliveira (Petrobras)

_____

Ph. D. Ricardo Jahnert (Independent Consultant)

_____

Ph. D. Francisco Romério Abrantes Júnior (UFF)

_____

Ph.D. Wagner Moreira Lupinacci – Advisor (UFF)

Niterói, RJ
2025

Ficha Catalográfica

Ficha catalográfica automática - SDC/BIG
Gerada com informações fornecidas pelo autor

B745i Boss, Tess
Identification of igneous bodies using spectral decomposition in the pre-salt interval of the Mero Field, Santos Basin / Tess Boss. - 2025.
111 f.: il.

Orientador: Wagner Moreira Lupinacci.
Dissertação (mestrado)-Universidade Federal Fluminense, Instituto de Geociências, Niterói, 2025.

1. Spectral Decomposition. 2. Igneous Intrusions. 3. Pre-Salt Carbonates. 4. Mero Field. 5. Produção intelectual. I. Moreira Lupinacci, Wagner, orientador. II. Universidade Federal Fluminense. Instituto de Geociências. III. Título.

CDD - XXX

Bibliotecário responsável: Debora do Nascimento - CRB7/6368

Acknowledgements

I would first like to express my gratitude to my master's supervisor, Wagner Lupinacci, for accepting to guide me and for proposing a "tailor-made" dissertation topic that truly matched my interests and abilities. Thank you for welcoming me so kindly on the first day, for always being supportive and available, and for showing great understanding and kindness regarding my limited availability due to work, always respecting my pace. Thank you, Wagner, for giving me the opportunity to carry out this work under your guidance.

I would also like to warmly thank Zoraida, who showed incredible generosity towards me, helping me every time I needed it, even on weekends or in the evenings. You were a lifeline more than once, and I am sincerely grateful to you.

My thanks also go to Professor Jahnert, who was always willing to share his knowledge and consistently generous with his time. A big thank-you to Wanderson for all the help he provided in response to my countless requests related to remote access to my computer, always with great efficiency and availability. Thank you to João for his willingness and enthusiasm to exchange knowledge and for the in-depth technical discussions. Thank you for your patience and persistence in achieving a good deconvolution result. Thank you to Tone for the insightful feedback during my second seminar.

My thanks also go to those who gave me a helping hand at one moment or another—through insightful discussions, material support, or help with software — especially Andres Gordon, Mathilde, João, and Felipe Melo. Thank you to Mario Carminatti for his understanding, the trust he placed in me, and for his kindness and continuous support.

Thank you to François Lafferriere, who was the first person to encourage the idea of doing a master's degree in geophysics, and who also gave me my first opportunity to enter the Oil and Gas industry, opening completely new horizons when I first worked with seismic data.

Thank you to Michelle Whymark, who offered great support and remarkable understanding. Your words, even through messages, gave me strength in the moments when I needed courage the most.

Thank you to my friends—whether in Switzerland, Brazil, or elsewhere—who always supported me with their kind words, especially Thiaguinho and Thiago. Thank you to Duda, who over these last years has been my partner in work, in the master's program, and in many other things. This journey was sometimes a bit of a challenge and sometimes a source of joy and resilience, but fortunately always shared between us two. Thanks to you, even the struggles came with laughter.

Thank you to my family in Switzerland for their support, understanding, and kindness, and to my in-laws, Rose and Júnior, who have also been very supportive.

And finally, thank you from the bottom of my heart to Bruno for his constant support, for always encouraging me to give my best, and for the understanding and patience required by these two years of work and dedication. Thank you to him and to Duna for being my greatest joy and comfort every day.

ABSTRACT

The Mero Field lies in ultradeep waters in the northeastern part of the Santos Basin, along Brazil's southeastern margin. This giant oil field represents the northwestern portion of the Libra Block, where magmatic activity has significantly influenced reservoir evolution and CO_2 distribution. Two magmatic suites are recognized in Mero: a tholeiitic one of Barremian–Aptian age and an alkaline suite of Santonian–Campanian age. Diabase intrusions and subaerial lava flows occur at different stratigraphic levels and show distinct emplacement styles. Owing to extensive well control, the field offers an excellent opportunity to test methodologies for identifying igneous bodies in seismic data. This is particularly relevant because, while igneous rocks are easily detected when intruding post-salt sediments—due to their strong acoustic impedance contrast with the sedimentary host rocks—discrimination becomes far more challenging within the pre-salt interval, where anhydrite, igneous rocks, and low-porosity carbonates of the Barra Velha Formation exhibit overlapping impedance ranges. In such cases, interpreters cannot rely solely on amplitude-based attributes; additional attributes sensitive to other physical properties must be considered to distinguish igneous from non-igneous lithologies. This study aims to define the spectral signature and spatial distribution of igneous occurrences in the Mero Field using a high-resolution spectral decomposition approach. A Reverse Time Migration (RTM) seismic volume was analysed through a workflow involving Matching Pursuit decomposition. To extend the analysis beyond the reservoir interval, the spectral response of each feature of interest was characterized on spectrograms: concordant diabase sills at the base of the salt typically display low- to medium-frequency responses, whereas non-intruded areas show higher-frequency signatures. Intrusions beyond seismic resolution are recognized by their strong impedance contrast, discordant geometry, and low- to medium-frequency spectral responses that delineate their edges. The combination of shale layers overlying lava flows at the base of the Itapema Formation yields low-frequency anomalies. In the Piçarras Formation, intrusive bodies show low-frequency characteristics, whereas lava flows display predominantly high-frequency responses. After performing RGB and HSV spectral blend analyses on seismic lines and horizon slices, geobodies were subsequently extracted to better represent the occurrence of igneous features within

each relevant interval. Methodological considerations and limitations are also discussed. Overall, Matching Pursuit decomposition proved efficient for detecting igneous bodies within pre-salt sequences, providing a useful tool for exploration-oriented workflows.

Keywords: Santos Basin; Mero Field; Pre-Salt carbonates; Igneous intrusions; Spectral decomposition; Matching Pursuit.

RESUMO

O Campo de Mero situa-se em águas ultraprofundas na porção nordeste da Bacia de Santos, ao longo da margem sudeste do Brasil. Este campo gigante de petróleo corresponde à porção noroeste do Bloco de Libra, onde a atividade magmática exerceu influência significativa sobre a evolução do reservatório e a distribuição de CO_2. Duas suítes magmáticas são reconhecidas no Campo de Mero: uma suíte toleítica de idade Barremiano–Aptiano e uma suíte alcalina de idade Santoniano–Campaniano. Soleiras de diabásio e derrames de lava subaéreos ocorrem em diferentes níveis estratigráficos e apresentam estilos de intrusão distintos. Devido ao extenso controle por poços, o campo oferece uma excelente oportunidade para a avaliação de metodologias voltadas à identificação de corpos ígneos em dados sísmicos. Tal aspecto é particularmente relevante, pois, embora as rochas ígneas sejam facilmente detectadas quando intrudem sedimentos pós-sal — em razão do forte contraste de impedância acústica com as rochas sedimentares encaixantes —, sua discriminação torna-se significativamente mais desafiadora no intervalo pré-sal, no qual anidrita, rochas ígneas e carbonatos de baixa porosidade da Formação Barra Velha apresentam faixas de impedância sobrepostas. Nesses casos, os intérpretes não podem se basear exclusivamente em atributos sísmicos baseados em amplitude; torna-se necessário considerar atributos adicionais sensíveis a outras propriedades físicas, de modo a distinguir litologias ígneas de não ígneas. Este estudo tem como objetivo definir a assinatura espectral e a distribuição espacial das ocorrências de ígneas no Campo de Mero por meio de uma abordagem de decomposição espectral de alta resolução. Um volume sísmico migrado por Reverse Time Migration (RTM) foi analisado a partir de um fluxo de trabalho que envolve a decomposição por Matching Pursuit. Com o intuito de estender a análise para além do intervalo reservatório, a resposta espectral de cada feição de interesse foi caracterizada por meio de espectrogramas: soleiras de diabásio concordantes na base do sal tipicamente exibem respostas de baixa a média frequência, enquanto áreas não intrudidas apresentam assinaturas de frequência mais elevada. Intrusões acima da resolução sísmica são reconhecidas por seu forte contraste de impedância, geometria discordante e respostas espectrais de baixa a média frequência, que delineiam suas

extremidades. A associação de camadas de folhelho sobrepostas a derrames de lava na base da Formação Itapema resulta em anomalias de baixa frequência. Na Formação Piçarras, corpos intrusivos apresentam características de baixa frequência, ao passo que os derrames de lava exibem predominantemente respostas de alta frequência. Após a realização de análises de blend espectral RGB e HSV em linhas sísmicas e horizontes, geocorpos foram subsequentemente extraídos com o objetivo de representar de forma mais adequada a ocorrência de feições ígneas em cada intervalo relevante. Considerações metodológicas e limitações também são discutidas. De maneira geral, a decomposição por Matching Pursuit mostrou-se eficiente na detecção de corpos ígneos em sequências pré-sal, constituindo uma ferramenta útil para fluxos de trabalho orientados à exploração.

Palavras-chave: Bacia de Santos; Campo de Mero; Carbonatos do Pré-Sal; Intrusões ígneas; Decomposição espectral; Matching Pursuit.

TABLE OF CONTENTS

LIST OF FIGURES

LIST OF TABLES

1. Introduction

1.1 The Libra Block and Mero Field

The Mero Field is located in the northeastern part of the Santos Basin, southeastern margin of Brazil, in ultradeep waters, approximately 175 kilometers from the coastal boundary of the municipality of Rio de Janeiro (Fig. 1). This giant oil field represents the northwestern sector of the Libra Block, which was discovered in 2010 by Petrobras and ANP. The first well drilled, 2-ANP-2A-RJS, had the purpose of exploring the pre-salt play by reaching the Barra Velha and Itapema Formations and was successful, as an oil column about 300 meters thick was encountered, in carbonates that show high porosity and permeability qualities. This discovery led to the delineation of the Libra Block, characterized by a four-way structural closure spanning over 500 km² and oriented in a northwest–southeast direction. Libra Block constitutes the first Production Sharing Contract in Brazil, and it was acquired in 2013 by the consortium constituted of Petrobras as operator (with a 40% interest), Shell (20%), TotalEnergies (20%), CNPC (10%) and CNOOC (10%). PPSA acted as the entity responsible for managing Brazil's Production Sharing Contract. The well W735, drilled in the central part of the block, revealed a compartmentalization of the reservoir expressed by different pressure regimes and fluid. Since, a lot of efforts were made to delineate the northeastern area. Several other wells were drilled to better understand the reservoir characteristics by collecting rocks and fluid data. Formation tests as well as extended well test campaigns were conducted. Also, new high resolution seismic data was acquired taking advantage of OBN technology. In 2017, the Mero's field declaration of commerciality was released, and the first oil was produced in early 2022. To date, a total of 32 wells has been drilled in the Libra Block, and four FPSO units are undergoing installation (Chagas et al., 2024).

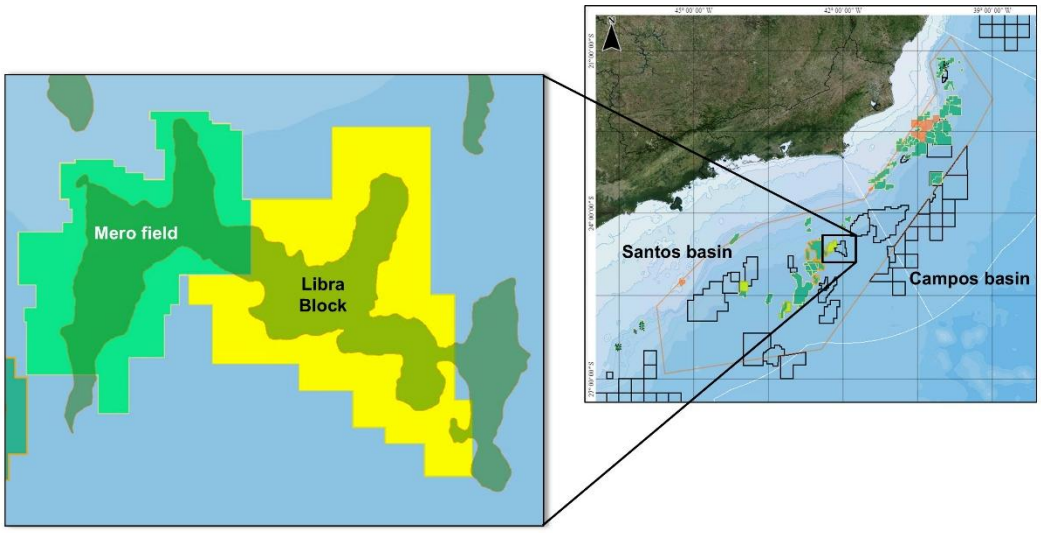

Figure 1. Location of the Libra Block and Mero Field, Santos Basin.

The Mero Field is located in an offshore region defined by water depths ranging from 1,700 to 2,400 meters. It is characterized by a thick salt layer that can reach 2000 meters, as well as an important Aptian carbonate reservoir thickness. The main reservoir rocks of the field are owing to Barra Velha and Itapema Formation. Bivalve rudstones, well-known as *Coquinas* in Brazilian pre-salt, represents the reservoir rocks of Itapema Formation, while stromatolites and grainstones are characteristic for the Barra Velha Formation. Nevertheless, the carbonate reservoir in Mero presents a large heterogeneity that sums with the structural complexity, making challenging reservoir properties prediction. Despite this major challenge, the high productivity of these reservoirs remains noteworthy, and the oil column attains a thickness of 500 meters. In addition, the hydrocarbon fluid exhibits excellent quality: oil 27º API, a gas-oil ratio between 375 and 448 m3/m3 std and a low H2S content (less than 0,5 to 16 ppm). However, the uniqueness of this oil field lies in the high CO_2 content of the fluid (~44%), as well as the presence of igneous rocks interbedded within the carbonate reservoir (Chagas et al., 2024; Rancan et al., 2018).

Two suites of magmatic rocks are recognized in the field today. The first one, dated from Barremian to Aptian, has tholeiitic affinity and occurs mainly as basalts, but occasionally also as diabases and hyaloclastites, which suggest subaqueous magmatism. These rocks are found within the Itapema Formation and,

less frequently, the Piçarras Formation. 40Ar/39Ar analyses indicate ages of approximately 127.8 ± 1.5 Ma, with alteration occurring around 114 Ma. The second suite comprises hypoabyssal alkaline rocks of Santonian to Campanian age. These occur mainly as diabases, but also include gabbros, alkaline basalts, and lamprophyres. They intrude carbonate reservoirs overlying the Barra Velha Formation and are also found within the Itapema Formation. In the southeastern area of the Libra Block, these rocks are genetically associated with small Upper Cretaceous volcanoes, which they fed with magma, while themselves being connected to—and recharged by—a deeper-seated intrusive complex. The age of this suite ranges from approximately 83.3 ± 0.7 Ma to 72.4 ± 4.9 Ma, with alteration during the Eocene at 49.9 Ma (Rancan et al., 2018; Marins et al., 2025).

1.2 Impacts of Magmatism on the Petroleum System

Understanding the occurrence of igneous rocks in sedimentary basins is crucial, as magmatism exerts broad and significant impacts—either positive or negative— that can affect any element of the petroleum system, from the source rock charge to hydrocarbons trapping.

Source rock maturity can be promoted, sometimes leading to early generation, by contact metamorphism with sill intrusions (Pongwa-pee et al., 2020; Schofield et al., 2015). On the other hand, the source rock interval can become overcooked, resulting in thermogenic gas generation (Milani & Zalán., 1999). Also, contact metamorphism associated with intrusions has the potential to release CH_4 and CO_2 into the atmosphere or lock them in subsurface reservoirs (Svensen et al., 2004; Oliveira et al., 2024).

Igneous rocks, when sufficiently fractured, and hydrothermal vents—fracture-related structures formed by the escape of fluids and gases—can act as migration pathways. By contrast, dykes can also act as impermeable barriers. (Penna et al., 2019; Eide et al., 2018)

Hydrothermal circulation, coupled with CO_2-rich fluids, has the potential to promote dissolution processes and karst formation, improving the reservoir quality (Szatmari & Milani., 2016; Moreira Lima et al., 2022). In addition, fractured

igneous rocks, volcaniclastics or even autobreccia can exhibit good porosity and permeability properties, with good fluid flow capacity, making them suitable reservoir rocks (oral information from R. Jahnert). On the other hand, hydrothermalism can also negatively affect carbonate reservoirs by modifying water-pore composition, which would impact the diagenetic evolution of the reservoirs by causing cement precipitation of dolomite, silica or calcite and other minerals (Moreira Lima et al., 2022; Sartorato et al., 2020). In pre-salt, Barra Velha Formation is mainly affected by dolomitization, while Itapema Formation by calcite precipitation. The silicification of the carbonate rocks occurs in both formations (Sartorato et al., 2020).

Intrusive rocks can contribute to trap formation, for instance when producing forced-fold anticline traps (Pongwa-pee et al., 2020), but they can also destroy pre-existing ones. They can act as the main seal of the petroleum system (Ren et al., 2020). Sometimes, they drive reservoir compartmentalization, which reduces field productivity.

Magmatism also significantly influences the amount of CO_2 in the pre-salt oil fields. Along with representing a technical challenge and risk factor for the production, it also diminishes the economic value of the produced oil (Baptista et al., 2023; Gamboa et al., 2019).

The impacts on the petroleum system associated with the presence of igneous rocks in a sedimentary basin—and, more broadly, the diverse implications linked to magmatism—are far more numerous than those discussed above. The occurrence and abundance of igneous rocks within an exploration block significantly increase exploratory geological risk, potentially affecting each element of the petroleum system. Consequently, they exert substantial influence on relinquishment decisions, as exemplified by the southern sector of the Libra Block.

1.3 Igneous Rocks Identification in Pre-Salt: the Geological-Geophysical Problem

Igneous rocks within sedimentary basins are usually highly expressive in seismic data due to the strong acoustic impedance contrast between them and the

surrounding sedimentary background. In fact, their typical velocities range between 5,000 and 7,000 m/s. By contrast, the velocities of the siliciclastic background sediments are generally on the order of 2,500–3,500 m/s (Planke et al., 2015). As a result, igneous bodies in the post-salt section of the Santos Basin can be readily identified in amplitude data and are strongly highlighted through the use of amplitude-contrast-based seismic attributes.

In contrast, magmatic rocks in the pre-salt section pose a far greater challenge. This is largely due to the significant overlap in acoustic impedance between these rocks and the anhydrite situated at the base of the Ariri Formation, as well as the cemented carbonates that, in many areas, define the top of the Barra Velha Formation. Differentiating these lithologies is further hindered by seismic imaging difficulties beneath the very thick, stratified salt layer that characterizes this area, which may reach up to 2,000 meters in thickness. Such conditions create a highly complex imaging environment that strongly impacts the quality of the seismic data available for interpretation.

Moreover, pre-salt magmatic rocks are highly diverse. They occur both as extrusive flows and as intrusive bodies (diabase sills), the latter often displaying geometries that, in most cases, deviate from the classical “Victoria Regia” sill model. In many situations, they are concordant or sub-concordant with the stratigraphy. The thickness of these igneous features also represents a major limitation for their seismic detection. According to Oliveira et al. (2024), citing Mark et al. (2018), most sills range between 5 and 40 meters in thickness—well below the seismic resolution of 93–113 m (as calculated by Oliveira using RTM seismic data). This implies that a large proportion of these bodies are not detectable in seismic data, or if detectable, their top and base cannot be properly mapped (Fig.2).

Other geological processes also impact rock density, further complicating the differentiation of pre-salt lithologies. For example, fracturing at the base of igneous bodies may reduce density, while contact metamorphism between intrusions and carbonates tends to seal pore spaces, thereby increasing acoustic impedance. Similarly, hydrocarbon interaction with anhydrite may raise the acoustic impedance of this interface. These factors contribute to the significant impedance overlap observed among pre-salt lithologies.

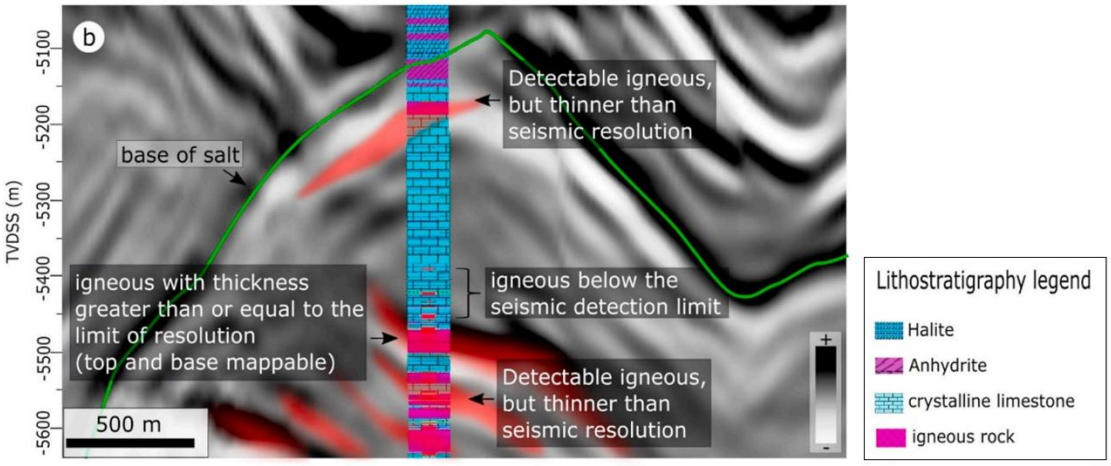

Figure 2. Interpreted seismic profile near well 3-BRSA-1322_RJS in the Mero field, illustrating variations in igneous body thicknesses. Some bodies are mappable, others are only detectable, while some fall below the detection limit (after Oliveira et al., 2024).

Identifying magmatic rocks in the Brazilian pre-salt is, therefore, a major challenge. It cannot be resolved solely through amplitude-based seismic attributes but requires the integration of complementary methods that incorporate additional physical and geological characteristics.

1.4 Review of Previous Works

The igneous rocks of the Mero Field have been identified and characterized through a combination of seismic interpretation, quantitative analysis, and machine learning. Oliveira et al. (2024) integrated manual seismic interpretation, elastic inversion, Bayesian volumetric classification, and seismic attribute mapping—specifically amplitude-thickness maps and the Energy Ratio attribute—calibrated with well data, to differentiate intrusive and extrusive facies as well as hydrothermal vents. Maas et al. (2023) applied unsupervised machine learning (SOM, GTM, K-means) to a suite of seismic attributes—including Hilbert transform of amplitude (HTAM), interval velocity (FWI-derived VEL), energy ratio similarity (ERS), Hilbert transform of Lambda-Rho (HTLR), GLCM texture attributes, and curvature (K1, K2)—which revealed the distinct high-impedance, continuous, and planar signatures of igneous bodies, later validated against well control. In

their study, Penna et al. (2019) integrated advanced subsalt imaging (FWI and TTI-RTM) with elastic inversion and Bayesian facies classification based on P- and S-impedance cross plots, complemented by the use of geometric attributes to infer fracturing and flow behaviour. Collectively, these studies highlight how advanced seismic imaging, elastic property analysis, probabilistic classification, and machine learning complement each other to robustly map and characterize igneous rocks in the Santos Basin pre-salt.

However, these methods also carry uncertainties, limitations, and challenges in terms of reproducibility—particularly during the exploratory phase, when reprocessing, high-resolution velocity models, or elastic data may not yet be available. Most existing studies rely on large datasets, especially well data, which are rarely accessible in early-stage or frontier exploration. This underscores the need for alternative approaches better adapted to data-limited scenarios. In this context, seismic attributes and multi-attribute analyses have become essential tools in the interpreter's workflow, enabling the identification and characterization of geological features even under high uncertainty. Importantly, alternative workflows—based on creative and deeper use of available attributes—should not be seen only as substitutes in data-sparse contexts. In many cases, such approaches can yield insights as valuable as those derived from inversion volumes, Bayesian classification, or other data-intensive methods, providing complementary perspectives that enrich the overall geological understanding.

1.5 Spectral Decomposition Method

Spectral decomposition is a method that decomposes the seismic signal into its frequency components, from which different attributes can be derived. Because the seismic signal results from the superposition of frequencies whose responses are modulated by the thickness of geological events, amplitude analysis only displays the integrated response of these components. Spectral decomposition, in contrast, enables the estimation and enhancement of the relative contribution of specific frequency bands over time, allowing for the identification of geological and stratigraphic features not readily discernible through conventional amplitude-based approaches.

Traditionally, spectral decomposition has been applied in siliciclastic settings, where it has proven highly effective in characterizing depositional system elements such as fluvial channels and submarine turbiditic lobes. When displayed as attribute maps, it provides valuable insights into relative thickness, lateral extension, internal architecture, complex geometry, connectivity—features and facies distribution that are often less evident in attributes based solely on amplitude contrast. Results are commonly visualized through RGB blending of three frequency bands, allowing the interpreter to separate frequency ranges by color contrast. This approach can also highlight, for instance, very thin channels that become evident when higher frequencies are isolated.

In Brazil, some studies have explored the application of spectral decomposition in offshore settings in non-siliciclastic depositional environments. Costa Correia et al. (2019) applied the method in time slices to characterize sill geometries in the Campos Basin. Jesus et al. (2020) combined Hybrid Spectral Decomposition (HSD) with geometric attributes to propose a workflow for identifying pre-salt carbonate mounds, successfully distinguishing reservoir-prone carbonates from low-amplitude shales. While spectral decomposition has shown potential in characterizing igneous intrusions and in multi-attribute analysis of carbonate settings, its most widespread use in the hydrocarbon industry remains in siliciclastic environments. This is largely due to the relative ease with which it yields significant, sometimes even striking, results. By contrast, applications in pre-salt carbonate reservoirs remain relatively marginal.

1.6 Research Proposal and Objectives

In the specific context of the Mero Field, spectral decomposition could provide valuable insights into the identification of magmatic intrusions, particularly given the significant overlap in acoustic impedance between igneous rocks, cemented carbonates, and anhydrite. By exploiting the effect of relative reflector thickness—even for igneous bodies smaller than seismic resolution—it may be possible to distinguish areas where this impedance overlap occurs from those where it does not. Seismic sections suggest that, where anhydrite is in direct contact with the reservoir, the reflector interpreted as the reservoir top beneath the anhydrite is

thinner than in areas where a diabase layer is intercalated between the two. This impedance overlap often results in a strong positive reflector followed by a thick negative one. Spectral decomposition may capture this variability in the seismic response of the Barra Velha Formation top, enabling the definition of specific frequency ranges sensitive to such changes. The methodology could also prove useful in identifying intrusive and extrusive bodies occurring in other intervals of the Mero Field.

The aim of this study is to propose a methodology applicable already at the exploratory stage, using spectral decomposition, to support the identification of igneous bodies in pre-salt. To this end, the most suitable spectral decomposition method will be defined, and the spectral signature of the magmatic bodies of interest will be characterized through spectrogram analysis. The visualization and extraction procedures used to represent the results will also be discussed.

The Mero Field provides an ideal case study due to the abundance of igneous bodies within the pre-salt interval, occurring both inside and outside the reservoir, and related to different magmatic events with varying morphologies (intrusive and extrusive). Furthermore, the number of drilled wells in the field provides a robust control dataset for testing and calibrating results. Finally, the Mero context is particularly relevant for testing such a methodology, given the challenges posed by magmatism in reservoir characterization and the implications it may have for issues such as CO_2 production.

2. Geological Setting

PART 1 – SANTOS BASIN

2.1.1 Formation and Evolution of the Southeastern Brazilian Margin

The Santos Basin, together with the adjacent Campos and Espírito Santo basins, occupies a central segment of the southeastern Brazilian passive margin. Its origin is tied to the fragmentation of Gondwana and the diachronous opening of the South Atlantic Ocean, initiated during the Late Jurassic to the Early Cretaceous. The tectonic architecture of this margin was profoundly influenced by long-lived Precambrian structural fabrics, particularly those of the Ribeira and Dom Feliciano belts formed during the Brazilian/Pan-African orogeny (600–510 Ma). These orogenic systems imparted a dominant NE–SW and NW–SE structural grain that acted as zones of weakness during lithospheric stretching and rift propagation (Mohriak, 2001; Szatmari & Milani, 2016). Similar interpretations had been proposed earlier by Chang et al. (1992).

In addition to this inherited basement anisotropy, deep seismic imaging suggests that beneath the pre-salt succession lies a thick Paleozoic sedimentary package, potentially correlatable with Paraná Basin formations such as the Silurian–Devonian Ponta Grossa shales, the Permian Irati source rocks, and the Triassic–Jurassic Pirambóia and Botucatu sandstones. These strata may be preserved beneath the Early Cretaceous Serra Geral basalts (Zalán, 2016). If correct, this model implies that the “basement” of the Santos Basin is not exclusively crystalline but includes an older sedimentary succession whose pre-existing geometry influenced the location of later rift depocenters and transfer zones (Zalán, 2016; Freitas et al., 2022).

The onset of rifting between South America and Africa was accompanied by extensive magmatism related to the Tristan da Cunha mantle plume, expressed through the Paraná–Etendeka Large Igneous Province (LIP), with flood basalt eruptions dated between 134 and 129 Ma (Peate, 1997, cited in Szatmari & Milani, 2016). This plume-derived activity produced voluminous continental

tholeiitic flows, extensive dyke swarms aligned with inherited crustal fabrics (e.g., Ponta Grossa, Serra do Mar, Vitória–Colatina), and seaward-dipping reflectors (SDRs) seismically imaged along the distal volcanic margin (Mohriak, 2001; Gordon et al., 2023). Later alkaline intrusive complexes along the coastal region (e.g., Cabo Frio, Poços de Caldas) are younger, post-rift manifestations attributed to lithospheric reactivation and residual mantle melting rather than to the main Paraná–Etendeka event (Louback et al., 2021; Mohriak et al., 2022). The intensity of magmatism was not uniform across the margin; it increased southward toward the Pelotas Basin, producing a pronounced north–south asymmetry in crustal thickness and rift architecture (Szatmari & Milani, 2016; Mohriak & Barros, 1990).

Crustal-scale studies further reveal the hybrid character of the Santos margin. Based on gravity, magnetic, and deep seismic data, Zalán et al. (2011) identified significant crustal tapering, strong lower-crustal reflectivity (interpreted as mafic granulites or eclogites), and shallow serpentinized mantle exposures near the continent–ocean transition. These features typify magma-poor margins, where lithospheric thinning is accommodated not only by brittle faulting but also by ductile flow and exhumation of the lower crust and upper mantle. However, the Santos margin also displays localized volcanic features — including intrusive complexes, SDR wedges, and seamount chains, particularly near the Florianópolis Fracture Zone and the Abimael propagator (Gomes et al., 2002; Gomes et al., 2008; Mohriak et al., 2021). This combination of features supports the interpretation that Santos represents a transitional (or “hybrid”) margin type, with both volcanic and magma-poor characteristics (Mohriak, 2001; Zalán et al., 2011; Gordon et al., 2023).

2.1.2 Main Tectonic Phases

The tectono-stratigraphic evolution of the Santos Basin records the progressive transition from continental rifting to oceanic spreading along the southeastern Brazilian margin. Four main phases can be distinguished—pre-rift, rift, sag (post-rift), and drift—each characterized by distinct tectonic and geodynamic processes that shaped the basin’s structural architecture and depositional framework

(Moreira et al., 2007; Mohriak, 2001; Szatmari & Milani, 2016; Freitas et al., 2022).

Pre-rift Phase

The pre-rift phase, spanning the Late Jurassic to Early Cretaceous, reflects the initial mechanical stretching of the lithosphere prior to the onset of significant fault-bounded subsidence (Zalán et al., 2011). This period was dominated by regional crustal doming and widespread tholeiitic magmatism associated with the Paraná–Etendeka Large Igneous Province (LIP). Basaltic flows and dike swarms dated between 134 and 129 Ma are correlated with the Serra Geral Formation and represent the first manifestation of lithospheric rupture during Gondwana breakup (Szatmari & Milani, 2016; Moreira et al., 2007). The Top Basalt Unconformity, marking the upper boundary of these volcanic sequences, forms a prominent seismic reflector across the basin and represents a key regional surface separating the magmatic basement from the overlying syn-rift siliciclastic successions (Zalán et al., 2019).

During this phase, crustal extension was guided by inherited Precambrian anisotropies of the Ribeira and Dom Feliciano belts, defining the principal rift orientation and future sub-basin boundaries (Mohriak, 2001; Szatmari & Milani, 2016).

Rift Phase

The rift phase (Barremian to early Aptian) corresponds to the main period of crustal faulting and subsidence, resulting in the development of asymmetric half-graben systems. Normal faulting produced structurally controlled depocenters separated by transfer zones trending NE–SW and NW–SE, where the greatest subsidence and sediment accumulation occurred (Freitas et al., 2022). During this stage, continental to lacustrine sedimentation filled the grabens, recording the peak of extensional activity and the establishment of internal drainage systems (Moreira et al., 2007).

The Pre-Alagoas Unconformity represents the upper limit of this phase and coincides with the cessation of major faulting. It separates the syn-rift sequences from the overlying sag carbonates and records a significant tectono-stratigraphic

break associated with the transition from active rifting to passive thermal subsidence (Pedrinha et al., 2018, cited in Cruz, 2023).

Sag (Post-rift) Phase

The sag or post-rift phase (Aptian) developed under conditions of regional thermal subsidence following the cessation of active faulting. During this interval, the basin evolved into a broad, laterally extensive lacustrine depression that accumulated mixed carbonate–siliciclastic sediments under fluctuating hydrological and chemical conditions. This phase was characterized by the progressive stabilization of tectonic activity, an increase in accommodation space, and the establishment of restricted lacustrine to evaporitic environments (Moreira et al., 2007; Gomes, 2020).

The Intra-Alagoas Unconformity, dated at approximately 117 Ma, divides the lower and upper parts of the sag succession and represents a period of base-level fluctuation and localized subaerial exposure, possibly related to short-lived tectonic pulses or climatic oscillations (Pedrinha et al., 2018, cited in Cruz, 2023). The sag sequence terminates with the deposition of the Aptian evaporites of the Ariri Formation, whose basal surface corresponds to the Base of Salt Unconformity—a major stratigraphic boundary marking the onset of hypersaline conditions and the end of lacustrine deposition (Mohriak, Szatmari & Anjos, 2012; Zalán, 2016).

Drift Phase

The drift phase (Albian–Cenozoic) marks the establishment of open-marine conditions and the full development of a passive margin following the initiation of seafloor spreading in the South Atlantic. The earliest drift deposits consist of shallow- to open-marine carbonates that gradually gave way to marine shales and siliciclastic progradational wedges (Moreira et al., 2007; Freitas et al., 2022).

Thermal subsidence continued through the Late Cretaceous and Cenozoic, accompanied by local magmatic reactivation and intraplate deformation (Mohriak et al., 2021; Gordon et al., 2023). During the Cenomanian–Turonian, global anoxic conditions favored the deposition of organic-rich marine shales associated with the Oceanic Anoxic Event 2 (Schlanger & Jenkyns, 1976). From the Campanian

onward, the margin recorded progradational siliciclastic wedges and turbidite systems whose accumulation and geometry were strongly influenced by halokinesis and differential subsidence (Freitas et al., 2022; Mohriak, Szatmari & Anjos, 2012).

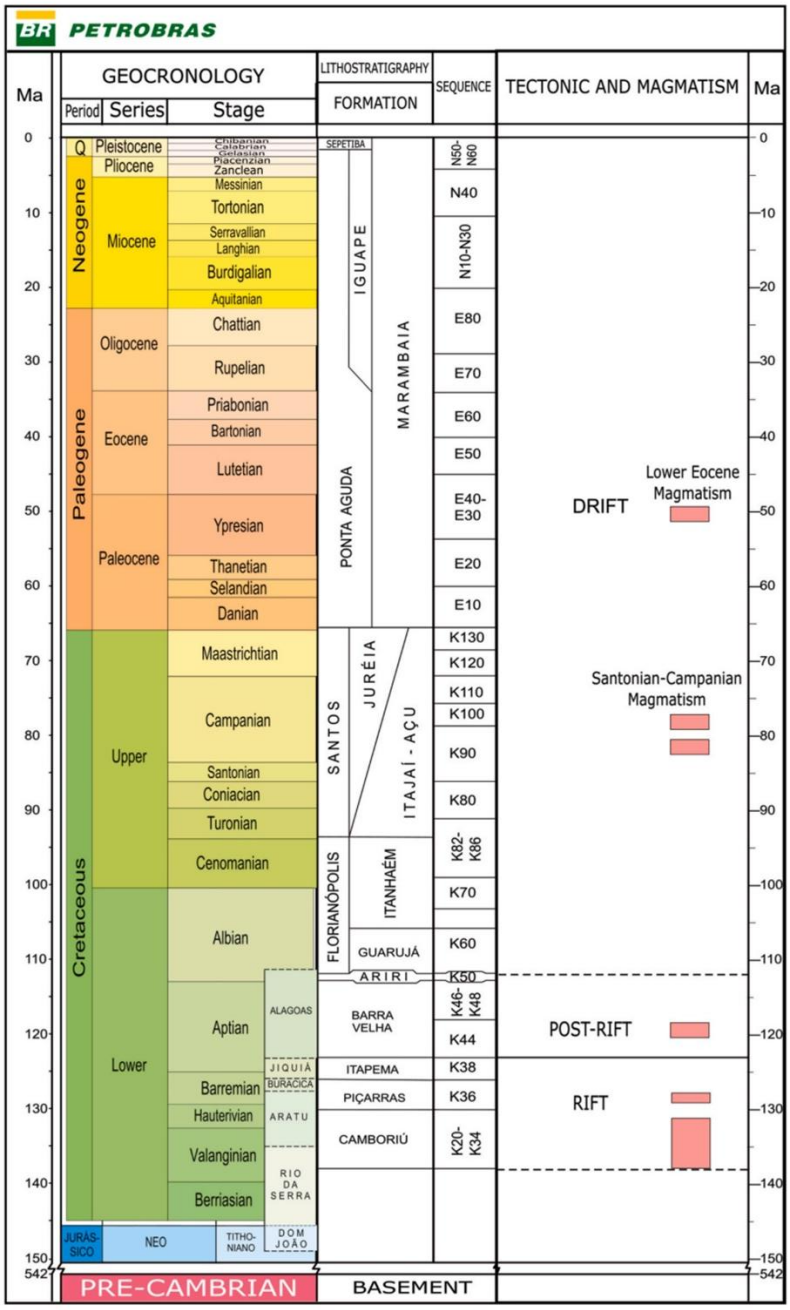

Figure 3. Santos Basin chronostratigraphic chart (from Marins et al., 2025, originally after Moreira et al., 2007).

2.1.3 Structural Framework

At the crustal scale, the Santos Basin is segmented into several first-order structural domains that record distinct stages of extension and crustal thinning. From west to east, these include the Internal Rift, the External Rift, and the Transitional and Oceanic Domains (Zalán et al., 2011). The Internal Rift Domain is characterized by rotated fault blocks and half-graben systems filled during the Barremian–Aptian syn-rift phase. These structures accommodated major subsidence and delineated the depocenters of early lacustrine sedimentation (Zalán et al., 2011; Moreira et al., 2007). Further basinward, the External Rift Domain represents the final stage of crustal thinning and exhumation, displaying hyperextended crust and localized mantle serpentinization (Zalán et al., 2011).

The basin is further compartmentalized into three main sub-basins—the Southwest Santos (SWSB), Central Santos (CSB), and Southeast Santos (SESB) sub-basins—bounded by basement highs and major lineaments (Moreira et al., 2007; Mohriak, Szatmari & Anjos, 2012; Zalán et al., 2011; Rigoti, 2015). These structural divisions reflect long-lived segmentation inherited from rift propagation and transfer zone activity. Among the most prominent structural highs is the Abimael Ridge, a basement-controlled feature that acted as a transfer structure separating syn-rift depocenters (Rigoti, 2015). Another key element is the External High, which delineates the transition between the Internal and External Rift domains. It represents a long-lived hinge zone that controlled accommodation and salt thickness variations (Zalán et al., 2011; Rigoti, 2015).

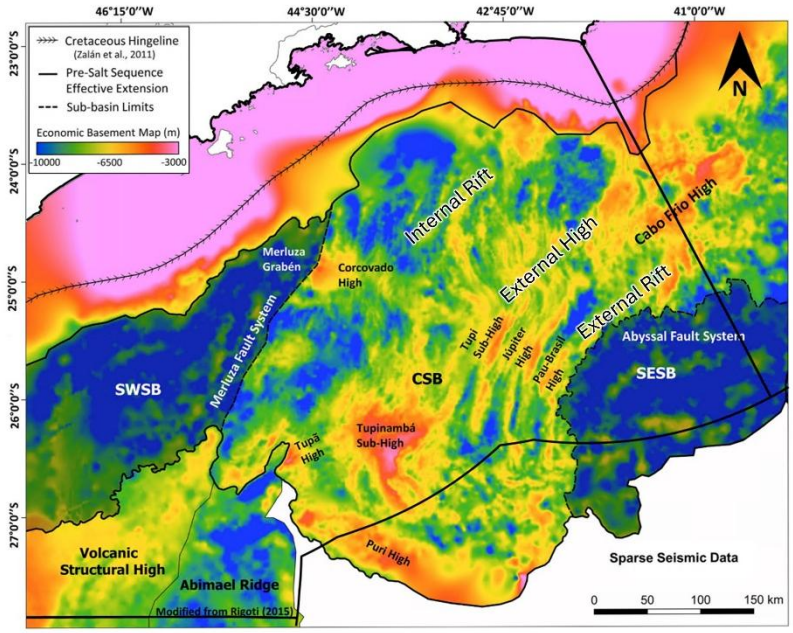

Figure 4. Economic Basement Map, from ANP. The indications of Internal Rift, External High and External Rift were added based on the interpretation of Gordon et al., 2023; Rigoti, 2015 and Zalán et al., 2019.

2.1.4 Overview of the Pre-Salt Stratigraphy

Rift stage: Camboriú, Piçarras, and Itapema Formations

The Camboriú Formation, located at the base of the pre-salt succession, records the onset of rifting during the initial stages of Gondwana breakup in the Early Cretaceous, around 133–127 Ma (Moreira et al., 2007). In the stratigraphic framework, Camboriú marks the beginning of rift deposition, separating the Precambrian basement from the overlying siliciclastic–volcaniclastic rift infill (Terra et al., 2010). Regionally, this formation includes tholeiitic basalt flows correlated with the Paraná–Etendeka Large Igneous Province, equivalent to the Serra Geral volcanism (Moreira et al., 2007; Mohriak, Szatmari & Anjos, 2012). These volcanic rocks are often interbedded with reworked volcaniclastic sediments and continental clastics, including oxidized red beds and alluvial sandstones (Cruz, 2023). Collectively, these deposits form the economic basement of the Santos Basin, providing the structural and stratigraphic foundation upon which the subsequent rift depocenters of the Piçarras Formation developed (Moreira et al., 2007; Mohriak, Szatmari & Anjos, 2012; Freitas et al., 2022).

The Piçarras Formation represents the peak of rift activity. It is characterized by lacustrine siliciclastics interbedded with talc–stevensite-bearing mudstones and shales, locally rich in organic matter (Moreira et al., 2007; Freitas et al., 2022). Restricted lacustrine environments developed under pronounced tectonic segmentation, producing organic-rich facies with source-rock potential together with volcaniclastic inputs and occasional carbonate lenses. Although its overall reservoir quality is limited, geochemical datasets confirm that Piçarras contributes to the source-rock system of the basin (Moreira et al., 2007). Thickness variations within Piçarras reflect segmentation along NW–SE transfer zones, which compartmentalized depocenters and controlled sediment accumulation (Freitas et al., 2022). The upper boundary of Piçarras corresponds to the Pre-Jiquiá Unconformity, a basin-wide surface marking a significant tectonic reorganization prior to the deposition of Itapema (Pedrinha et al., 2018, cited in Cruz, 2023).

The Itapema Formation records lacustrine deposition in fault-bounded lakes during the Barremian–Early Aptian. It consists of organic-rich shales, Coquinas, and talc–stevensite deposits (Moreira et al., 2007; Zalán et al., 2019). The Coquinas, dominated by bivalve and ostracod shells, form important reservoirs, while the shales represent prolific source rocks. Among these, the so-called Folhelho Jiquiá (Jiquiá Shale) is recognized as one of the main petroleum source rocks in the basin (Cruz, 2023; Freitas et al., 2022). Well data reveal average TOC contents around 4% and elevated hydrogen indices, confirming its high generative potential (Freitas et al., 2022). The upper limit of Itapema is defined by the Pre-Alagoas Unconformity, which marks the onset of more stable post-rift lacustrine conditions (Pedrinha et al., 2018, cited in Cruz, 2023).

Sag stage: Barra Velha Formation

The Barra Velha Formation (Aptian) is the most economically important carbonate reservoir of the pre-salt. It consists primarily of microbialites, laminated micrites, and spherulitic carbonates, locally interbedded with reworked grainstones and rudstones (Moreira et al., 2007; Gomes, 2020; Cruz, 2023). Facies distribution within Barra Velha shows strong structural control: microbial buildups preferentially developed on structural highs, while interbedded laminites siand spherulitites accumulated in deeper, low-energy settings (Chagas et al., 2024).

Reservoir quality in Barra Velha is highly heterogeneous. Shrubby boundstones and spherulitic packstones typically retain intercrystalline or vuggy porosity with good connectivity, whereas laminated micrites and dense microbial boundstones are generally tight unless fractured (Saller et al., 2016; Gomes, 2020). Fracturing, dolomitization, and hydrothermal overprinting can either enhance or degrade permeability depending on local diagenetic conditions (Farias et al., 2019; Ren et al., 2019). Thickness varies from less than 60 m on structural highs to more than 500 meters in sag depocenters (Carminatti et al., 2009; Zalán et al., 2019), reflecting strong structural and accommodation variations across the basin.

A main unconformity subdivides the Barra Velha succession: the Intra-Alagoas Unconformity (DIA, ~117 Ma), distinguishing lower K44 carbonates from the upper K46–K48 package (Pedrinha et al., 2018, cited in Cruz, 2023).

Within the uppermost portion of the Barra Velha, immediately below the Aptian evaporites of the Ariri Formation, an interval informally known as the “Marco Lula” (BVE110 sub-unit) has been widely recognized (Souto, 2010, cited in Chagas et al., 2024). This marker comprises ~30 m of alternating laminites and reworked laminitic grainstones/breccias, producing a serrated gamma-ray signature (Chagas et al., 2024).

Evaporitic sequence (Ariri Formation)

Capping the pre-salt succession, the Ariri Formation consists of thick Aptian evaporites dominated by halite and anhydrite, locally interbedded with gypsum and carnallite. Deposited in a restricted sag basin under arid conditions, these evaporites reach thicknesses exceeding 2 km in some depocenters (Mohriak, Szatmari & Anjos, 2012; Zalán, 2016). The Ariri salt provided a highly effective regional seal and established the conditions for salt tectonics that later reshaped basin morphology during post-salt evolution. Diapirism, salt walls, and related deformation strongly modified structural traps and controlled the distribution of overlying Cretaceous–Cenozoic sequences (Hudec & Jackson, 2007).

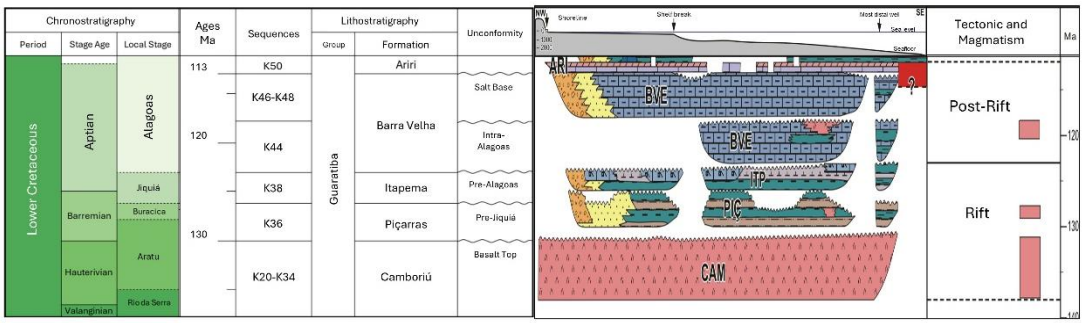

Figure 5. Segment of the stratigraphic chart of the pre-salt section of the Santos Basin (adapted from Chagas et al., 2024 and Moreira et al., 2007).

PART 2 – MAGMATIC EPISODES IN SANTOS BASIN

2.2.1 Overview and Regional Context

The Santos Basin, together with the Campos and Pelotas basins, forms the southeastern segment of the Brazilian passive margin, where contrasting styles of crustal extension and magmatism define a marked along-strike variability. According to Zalán et al. (2011) and Zalán (2015), the Pelotas Basin, located south of the Florianópolis Fracture Zone, represents a volcanic passive margin, characterized by thick basaltic accumulations and the presence of seaward-dipping reflectors associated with the Paraná–Etendeka Large Igneous Province (LIP).

By contrast, the Santos–Campos–Espírito Santo system to the north constitutes a magma-poor passive margin, in which rifting was dominated by ductile stretching of the lower crust and exhumation of serpentinized mantle, rather than by voluminous volcanic activity. As emphasized by Zalán (2015), the Santos Basin provides one of the most complete examples of a magma-poor passive margin, where magmatism is late, localized, and structurally controlled, and where the crust–mantle transition is marked by exhumed mantle domains instead of thick volcanic wedges. In this way, the magmatic evolution of the Santos Basin fits within a regional south-to-north gradient of decreasing magmatic intensity, placing it in an intermediate position between the highly volcanic Pelotas margin to the south and the magma-poor Campos margin to the north. Within the basin itself, however, magmatic centers are distributed from south to north, extending from the Santonian volcanic province in the southern sector to the Eocene alkaline complexes near the Cabo Frio High (Schattner et al., 2020; Mohriak et al., 2021; Louback et al., 2021).

Despite its limited volume, magmatism in the Santos Basin was persistent and multi-phase, accompanying nearly all major stages of tectono-stratigraphic evolution.

Gordon et al. (2023) proposed a three-stage classification that captures the main temporal and compositional trends of magmatic activity of the basin: (1) a pre-rift or rift-onset stage (~130–125 Ma) associated with initial crustal

stretching and represented by subaerial basaltic flows, forming the Camboriú Formation, regarded as the economic basement of the basin. (2) a syn- to post-rift stage (130–112 Ma) characterized by tholeiitic magmatism, expressed as subaqueous basalts interbedded within the Piçarras and Itapema Formations in the rift section (121-130 Ma) and then during the post-rift stage, within the lower Barra Velha Formation (118Ma). Both events were dated by $^{40}Ar/^{39}Ar$ method (Moreira et al., 2007). (3) a drift-stage phase (Albian to Cenozoic) dominated by alkaline volcanism and intrusive activity concentrated along deep crustal discontinuities lineaments such as the Cruzeiro do Sul, Capricórnio, Merluza, Aquarius and SAMA magnetic anomalies (Gordon et al., 2023; Ferreira et al., 2023).

This drift-related magmatism persisted through the Late Cretaceous and into the Cenozoic, evolving toward more alkaline compositions and showing a stronger structural control along reactivated basement lineaments (He et al., 2025; Louback et al., 2021; Mohriak et al., 2021). In seismic reflection data, these magmatic bodies exhibit a wide range of expressions—from tabular, high-amplitude reflectors associated with sills and lava flows, to chaotic or mounded facies corresponding to volcanic cones and hydrothermal vents. Numerous intrusive bodies related to the Late Cretaceous and Cenozoic volcanic events occur as diabases and dykes within the pre-salt layers, often cross-cutting the stratigraphy, or being emplaced between the top of the Barra Velha Formation and the overlying Ariri evaporites. Although less abundant, localized volcanic edifices and vent complexes have also been identified within the pre-salt interval (Fornero et al., 2019; Gordon et al., 2023), indicating that eruptive processes were not confined to post-salt strata. In the Eocene, Moreira et al. (2007) described submarine stratovolcanoes with chaotic internal seismic facies, composed mainly of hyaloclastites and volcaniclastic material, confirmed by drilling in both the Santos and Campos basins.

2.2.2 Rift–to–Post-Rift Magmatism within the Pre-Salt Sequence of the Santos Basin

Magmatism recorded in the pre-salt of the Santos Basin comprises (i) Early Cretaceous rift/syn-rift basalts and associated rocks, (ii) Aptian post-rift volcanic successions emplaced during sag-phase carbonate deposition, and (iii) younger drift-stage intrusions that locally affect the pre-salt interval. Magmatic activity from (i) and (ii) are reported in Fig.6.

Rift / Syn-rift magmatism (Early Cretaceous)

Serra Geral (~134–130 Ma)

Subaerial tholeiitic basalt flows form the economic basement of the basin and are contemporaneous with the Paraná–Etendeka continental flood basalts and the Serra do Mar dike swarm in SE Brazil. In the Santos stratigraphic framework these basalts represent the Camboriú Formation and are described as Early Cretaceous lava flows positioned beneath most of the basin's sedimentary fill (Moreira et al., 2007). The typical lithology of these basalts, as described by Moreira et al. (2007), is dark-gray, holocrystalline, medium grained, and shows an ophitic texture, composed mainly of plagioclase and augite pyroxene.

Libra Central (~125 Ma)

The Late Barremian to Early Aptian igneous rocks of the Mero Field and Libra Block consist mainly of basalts, with minor occurrences of diabase and hyaloclastic rocks of tholeiitic affinity. They occur predominantly as intrusions within the Itapema Formation in the Central compartment, but are also found in the Piçarras Formation, filling depressions between basement structural highs (half-grabens) in the Northwestern compartment. $^{40}Ar/^{39}Ar$ dating of tholeiitic rocks from the central sector yielded minimum ages of 125.5 ± 0.7 Ma, with evidence of alteration at 114.3 ± 1.1 Ma. (Rancan et al., 2018)

Post-rift (sag-phase) magmatism (Aptian)

Tupi (~120 Ma)

Extensive evidence from the Lula Field documents the Tupi magmatic event, identified in twelve wells as postdating the Camboriú Formation, with $^{40}Ar/^{39}Ar$

ages ranging from 121 to 117 Ma. This magmatic phase occurs predominantly within the clay-rich sediments of the Piçarras Formation, overlying the basaltic flows of the Camboriú Formation, and locally within the Itapema Formation. It consists of igneous rocks displaying varied compositions and textures, including volcaniclastic intervals such as pyroclastic and ignimbritic facies that show porosity and hydrocarbon indications. In many instances, the top of the Tupi magmatic interval defines the base of the carbonate reservoirs (Cruz, 2023).

Parati (~115)

Basin-scale syntheses identify a post-rift Aptian magmatic pulse informally referred to as the “Parati event,” associated with the early sag-phase stratigraphy and dated at approximately 115 Ma (Brito et al., 2024). The event was first recognized in well RJS-617A, which drilled volcanic rocks in the Parati prospect. Hunt et al. (2022) also identified magmatic rocks correlated with the Parati event in the Bacalhau Field, overlain by a slightly younger post-Parati episode termed the Picinguaba magmatic event.

Post-Paraty Picinguaba (< 115 Ma)

The Bacalhau Field exhibits volcanic-pedestal edifices that formed paleotopographic highs, which significantly impacted platform architecture of the overlying Barra Velha carbonate platforms. These volcanic bodies occur stratigraphically above the basalts of the Parati event and are interpreted as a post-Parati magmatic phase. Syndepositional faulting affected both volcanic and carbonate reservoir deposition. Well 3-EQNR-1-SPS penetrated igneous rocks linked to this event, for which no formal radiometric ages have been reported (Hunt et al., 2022).

Bacalhau Field appears to record multiple magmatic events according to different studies. In addition to the post-Parati Picinguaba and Parati phases described by Hunt et al. (2022), Louback et al. (2023) documented in well 4-BRSA-971B-SPS a ~500 m-thick sequence of low-Ti tholeiitic basalts interbedded with marl layers, dated by $^{40}Ar/^{39}Ar$ between 116.9 ± 0.1 Ma and 109.9 ± 0.2 Ma. Likewise, Gordon et al. (2023) reported that wells SPS-104DA and SPS-105 in the same field penetrated 150–216 m of basaltic and volcaniclastic rocks, with $^{40}Ar/^{39}Ar$ ages ranging from approximately 123 Ma to 118 Ma, according to ANP well file. The volcanic

successions are described as occurring beneath or interlayered with the pre-salt carbonates of the Barra Velha Formation.

Iguape (~113 Ma)

The Iguape magmatic event, also referred to as the Southern Santos magmatism, represents an Aptian volcanic episode in the southern sector of the Santos Basin, corresponding to the sag phase of basin evolution. In this region, well SCS-15 drilled approximately 390 m of alternating basaltic and coarse-grained volcaniclastic rocks arranged in a flat-lying reflector configuration (Gordon & Mohriak, 2015, cited in Gordon et al., 2023), suggesting an explosive magmatic character for this event. The volcanic succession rests on steeply dipping seaward-dipping reflectors (SDRs) and is overlain by the Aptian evaporites of the Ariri Formation. Ages reported in the literature place this activity at around 113 Ma.

Pāhoehoe lava flow units in southeastern deep-water sector

A pile of subaerial basaltic flows in the southeastern deep-water sector of the Santos Basin, located some 27 km west of the Abimael Ridge according to Gordon et al. (2023), was penetrated by well 1-BRSA-1050-SPS (SPS-90), which drilled approximately 400 m of pāhoehoe lava flows directly beneath the Ariri evaporites. These volcanic rocks, mainly of tholeiitic affinity, are assigned to the Early Cretaceous post-rift stage, with an estimated age of about 117 Ma (Fornero et al., 2018; Fornero et al., 2019). In their study, Fornero et al. (2019) described several types of subaerial basaltic lava flows, including compound, sheet, and rubbly pāhoehoe facies, and reported the occurrence of various structures such as massive volcanic rocks, volcaniclastic deposits, vesicular basalts, lava lobes, and breccias.

Drift-stage within the pre-salt

Two younger pulses overprint parts of the pre-salt section: a Santonian–Campanian phase (reported ages in Libra between 83.3 ± 0.66 and 72.4 ± 4.9 Ma) characterized by alkaline hypabyssal rocks (diabase, gabbro, alkaline basalt, lamprophyre) occurring mainly near the top of the Barra Velha Formation and locally in the Itapema Formation; and an Eocene phase documented as hydrothermal alteration affecting earlier intrusions (e.g., 49.9 ± 0.45 Ma in Libra) (Rancan et al.,

2018). Louback et al. (2021) report the occurrence of Eocene (41.06 to 38.62 ± 0.02 Ma) alkaline intrusions within pre-salt carbonate reservoir rocks of the Santos Basin, near the Cabo Frio Structural High. The magmatic suite ranges from alkaline lamprophyres representing the least evolved compositions to phonolites as the most evolved endmembers. These Late Cretaceous and Eocene events are treated in detail in the following sections.

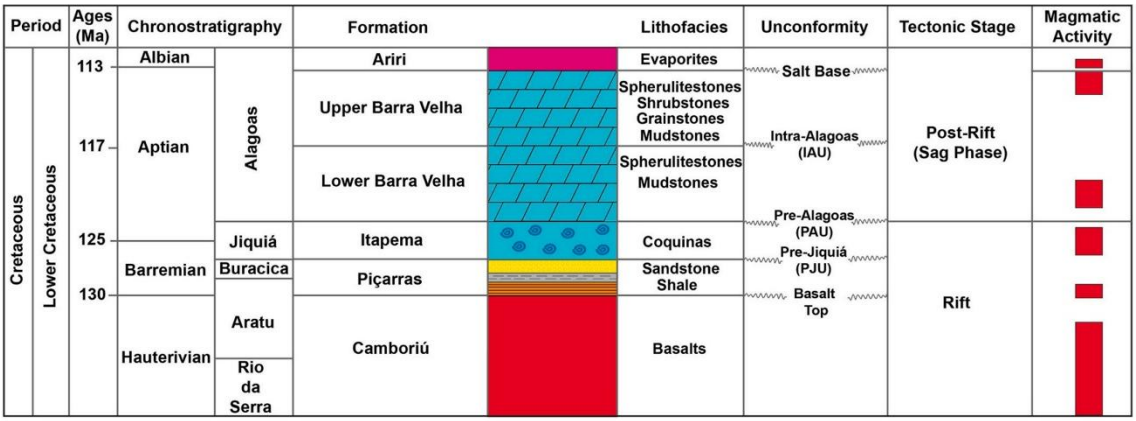

Figure 6. Lower Cretaceous stratigraphic section of the Santos Basin (after Brito et al., 2024 and adapted from Moreira et al., 2007).

2.2.3 Late Cretaceous (Santonian–Campanian) Magmatism

The Late Cretaceous marks a distinct phase of magmatic activity within the Santos Basin, subsequent to the Aptian–Albian rifting and early post-rift volcanism. The Santonian–Campanian episode (~86–77 Ma) is represented by scattered volcanic and intrusive centers extending from the southern Santos sector to the Cabo Frio–Libra area. Although volumetrically limited, this magmatism indicates that tectono-magmatic processes remained active during the drift stage, likely influenced by lithospheric reactivation and regional mantle dynamics (Schattner & de Mahiques, 2020; Magee et al., 2021; Mahiques et al., 2023; Gordon et al., 2023; Mitchell et al., 2021).

Distribution and Offshore Evidence

High-resolution seismic and well data reveal that Santonian–Campanian intrusions are distributed throughout the basin, occurring in both pre- and post-salt

intervals. In the southern Santos Basin, a 150 × 110 km magmatic complex—the *Santos Cluster*—comprises conical volcanic edifices, saucer-shaped plutons, and extensive sill networks developed between the top Basement and top Campanian (~72 Ma) reflectors. This cluster records a submarine tholeiitic volcanic province emplaced contemporaneously with halokinetic deformation of the Ariri salt, highlighting a strong structural coupling between magmatism and salt mobility (Schattner & de Mahiques 2020). Later dredging of exhumed diapirs confirmed the presence of altered tholeiitic basaltic xenoliths dated to 82.23 ± 0.35 Ma ($^{40}Ar/^{39}Ar$), providing direct geochronological evidence for this Early Campanian volcanic pulse (Mahiques et al., 2023).

Toward the central Santos Basin, the SPS-10 well penetrated multiple sills and dikes intruding Santonian–Campanian shales, sandstones, and siltstones, with K–Ar ages of 77 ± 3 Ma (ANP well file; Gordon et al., 2023). Geochemical analyses indicate alkali basalts enriched in TiO_2 (Fodor et al., 1983). Nearby seismic lines display several volcanic cones and intrusive feeders, characterized by positive reflectivity contrasts for sills and negative impedance for volcanic cones, diagnostic of dense intrusive versus vesicular extrusive lithologies (Gordon et al., 2023).

In the northern Santos basin, the RJS-566 and RJS-587 wells encountered extensive magmatic facies—including lava flows, volcaniclastic layers, dikes, and sills—within Albian carbonates and Santonian–Campanian siliciclastic intervals (Gordon et al., 2023). Seismic and borehole data reveal vertical to sub-vertical dikes and saucer-shaped sills forming part of the volcano's plumbing system. These intrusions are expressed by strong reflectivity contrasts—negative for the envelope reflectors of volcanic cones, consistent with a softer composition than the host rock, and positive for the denser dikes and sills (Gordon et al., 2023). Detailed studies by Moreira et al. (2006) dated these units from $^{40}Ar/^{39}Ar$ method at 82 ± 1 Ma and 48.1 Ma, showing their association with two volcanic episodes of Santonian and Eocene ages respectively.

Further east, pre-salt magmatic intrusions of Late Cretaceous age have been identified in the Libra Block and Mero Field, where diabase sills and dikes occur within the carbonate succession of the Barra Velha Formation (Oliveira et al.,

2019). $^{40}Ar/^{39}Ar$ dating from the RJS-741 well (Libra/Mero) yielded plateau ages of 85.9 ± 0.9 Ma, 85.3 ± 0.5 Ma, 85.2 ± 0.7 Ma, and 84.0 ± 0.4 Ma (Rancan et al., 2018; Gordon et al., 2023). These values place the magmatism squarely within the Santonian period, suggesting that Drift magmatic activity, by penetrating pre-salt carbonates, possibly interacted with hydrothermal systems within the Barra Velha reservoirs.

In the Cabo Frio Magmatic Province, around the Libra block, magnetic and seismic data reveal numerous intra-salt and post-salt intrusions and volcanoes, producing high frequency positive magnetic anomalies often of semi-circular shapes (Gordon et al., 2023).

Salt–Magma Interactions

3-D seismic analysis of the Merluza Graben area (Magee et al., 2021) further demonstrates that post-Ariri intrusions are abundant between the Albian and Santonian horizons, reflecting the interplay between halokinesis and magma emplacement. Thirty-eight intrusions were identified—roughly half within, and half above, the salt layer—showing how the evaporites guided magma distribution. The ductile salt acted as both barrier and conduit, localizing magma flow in regions of reduced thickness and redirecting intrusions laterally into sills or vertically along faulted corridors. This study constrains the timing of the main emplacement phase to the Albian–Santonian (~110–80 Ma) and shows that salt–magma coupling controlled both diapir growth and the final configuration of the intrusive system (Magee et al., 2021). Such interactions corroborate earlier observations of contemporaneous halokinetic deformation and volcanism in the southern basin (Schattner & de Mahiques, 2020; Mahiques et al., 2023).

Broader Tectono-Magmatic Significance

The spatial and temporal coherence of Santonian–Campanian intrusions across the basin indicates a regional magmatic pulse rather than isolated local events. Mitchell et al. (2021) proposed that this timing coincides with a global true-polar-wander (TPW) oscillation (86–78 Ma), reflecting a major reorganization of mantle convection and plume distribution. Such deep-mantle adjustments could have transiently enhanced thermal upwelling beneath thinned lithosphere, favoring partial melting and rejuvenating magmatism along the South Atlantic margins,

including Santos (Mitchell et al., 2021; Magee et al., 2021). This global mechanism provides a coherent geodynamic explanation for the Santonian–Campanian post-rift volcanism, suggesting that the Santos Basin's magmatic renewal was linked not only to local structural controls but also to planet-scale mantle processes.

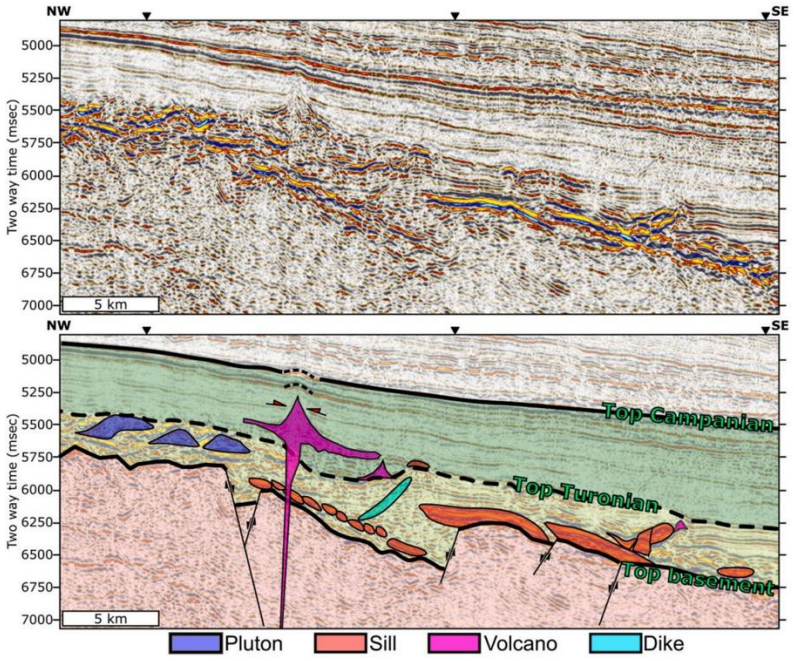

Figure 7. Seismic and interpreted profiles showing Campanian intrusive and extrusive structures in the Santos Cluster, southern Santos Basin. The magmatic bodies intrude sediments from the top basement to the lower Campanian level (after Schattner and de Mahiques, 2020).

2.2.4 Eocene Magmatism in the Northern Santos Basin

In the northern Santos Basin, magmatic activity did not end with the Santonian–Campanian volcanic phase but continued into the Paleogene. While Late Cretaceous intrusions and volcanic edifices are widely recognized along the Cabo Frio High and the Libra–Mero sector, a younger magmatic pulse during the Eocene (ca. 50–39 Ma) marks the final stage of post-rift tectono-magmatic reactivation across this region (Moreira et al., 2006; Oreiro et al., 2008; Mohriak et al., 2021; Gordon et al., 2023).

Distribution and Stratigraphic Context

The Eocene magmatism is concentrated in the northern and northeastern portions of the basin, particularly within the Cabo Frio Magmatic Province and the Santos–Campos transition zone, extending westward toward the Libra and Mero blocks (Gordon et al., 2023). Seismic and magnetic data show that magmatic bodies are aligned along deep crustal discontinuities—most notably the Cabo Frio/Cruzeiro do Sul and Guapiara/Capricórnio lineaments—which connect onshore fault systems of the Ribeira Belt to their offshore extensions (Oreiro et al., 2008; Mohriak et al., 2021; Gordon et al., 2023).

Borehole Evidence and Chronology

Several wells confirm the occurrence of Eocene intrusions and volcanic sequences in the Cabo Frio area. Well RJS-99 drilled through basaltic and diabase units dated at 50 ± 7 Ma (K–Ar, plagioclase) (Mizusaki et al., 1992, cited in Gordon et al., 2023), while RJS-104 intersected a complete volcanic edifice composed of roughly 750 m of basaltic and volcaniclastic rocks (Mohriak et al., 2022). Well RJS-685 penetrated multiple intrusive intervals from the post-salt to the pre-salt section, including a lamprophyre body dated at 38.6 ± 0.01 Ma, and a phonolite showing combined Campanian–Eocene ages (75.5–41.1 Ma) (Louback et al., 2021).

In the Libra Field, an $^{40}Ar/^{39}Ar$ plateau age of 49.9 ± 0.45 Ma obtained from well RJS-741 is interpreted as the age of hydrothermal alteration affecting older Santonian diabases within the Barra Velha Formation, confirming that magmatic and thermal activity persisted into the Eocene (Rancan et al., 2018).

Morphology and Composition

Seismic interpretation reveals that these Eocene intrusions consist of vertical to funnel-shaped high-amplitude anomalies, saucer-shaped or lily-pad sills, and associated feeder dikes, often connected to deeper crustal levels (Moreira et al., 2006; Mohriak et al., 2021). Petrographic descriptions identify diabase, phonolite, lamprophyre, and nepheline-bearing alkaline rocks, which locally crosscut both pre- and post-salt sequences and may generate small domal uplifts or fault reactivation in overlying strata (Mohriak et al., 2021; Gordon et al., 2023). These rocks exhibit strongly alkaline compositions, with feldspathoid-bearing assemblages

and EM1–OIB-type isotopic affinities, suggesting derivation from an enriched mantle source (Louback et al., 2021; Mohriak et al., 2021).

Structural and Genetic Controls

Across all studies, Eocene magmatism is interpreted as tectonically controlled rather than plume-related. According to Oreiro et al. (2008), the intrusions concentrate where SE–NW strike-slip faults intersect SW–NE normal faults, reflecting zones of pressure-release melting within a reactivated lithosphere. Similarly, Mohriak et al. (2021) attributes the Eocene magmatism to mantle reactivation along inherited crustal discontinuities, enhanced by halokinetic deformation and mild transtensional stress during the late drift stage. These processes favored partial melting of an enriched mantle and localized magma ascent along fault corridors extending from the crust–mantle boundary to the upper drift succession (Mohriak et al., 2021; Gordon et al., 2023).

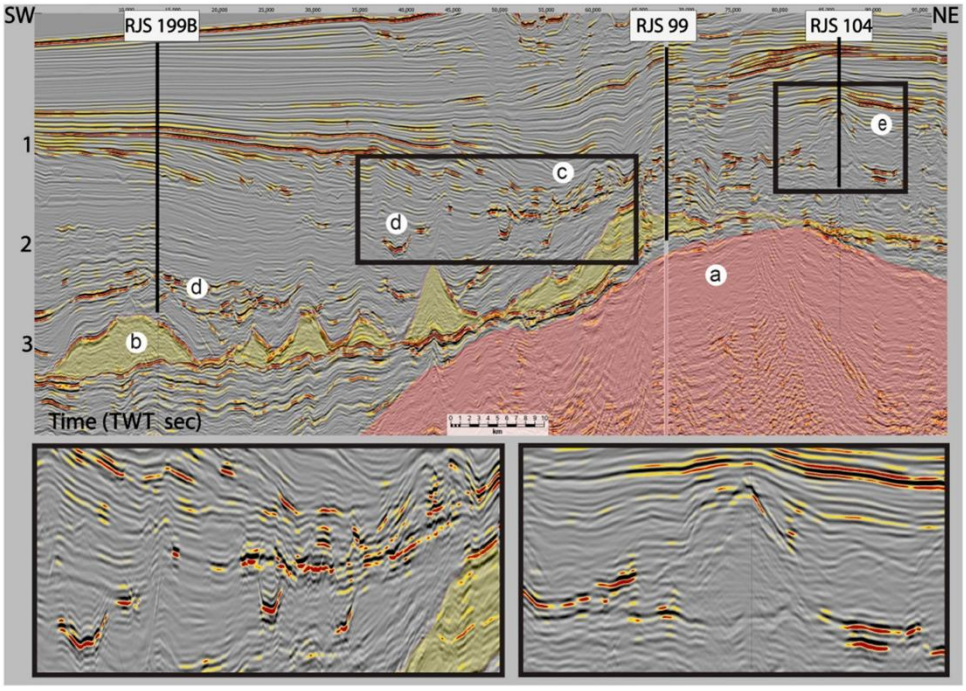

Figure 8. Seismic cross section across the Cabo Frio High area illustrating the numerous magmatic features associated with the Eocene event. Red corresponds to the acoustic basement and yellow to salt deposits. Letters c and e indicate volcanic cones, whereas letter d marks sills and dikes (after Gordon et al., 2023).

PART 3 – MERO FIELD / LIBRA BLOCK

2.3.1 Structural Framework

The structural configuration of the Libra exploration block is primarily controlled by normal faults trending NNE–SSW, a pattern that aligns with the regional tectonic framework associated with the rifting process. This fault orientation plays a key role in defining the overall geometry and compartmentalization of the block. Within this structural context, it is possible to distinguish three major compartments: northwest, central, and southeast. These domains are bounded by fault systems and exhibit distinct sedimentary architectures as well as varying structural styles, highlighting the complexity of the subsurface framework (Chagas et al., 2024).

Two major basement-rooted linear features contribute to the compartmentalization of the area: the Libra Transfer Zone (LTZ), a NW–SE-trending sinistral transtensive structure and the Curitiba Lineament (CL), which trends WSW–ENE (Fig. 9). They exert a significant influence on the spatial distribution and orientation of faults within the block. Notably, it induces a progressive rotation in fault direction—from a predominantly N–S trend in the northern sector to a NE–SW orientation in the southern portion. This rotation is fundamental to the development of structural highs and depocenters and has a direct impact on the configuration of the major faults that separate the three structural compartments (Dehler & Yamato, 2015, cited in Chagas et al., 2024; Rancan et al., 2018).

Focusing on the Mero Field, located within the northwestern structure, the fault pattern is generally N–S-oriented, but shifts to NE–SW in its eastern sector (Andrade et al., 2016, cited in Chagas et al., 2024). The structural framework of this field is composed of three main features: a gently dipping central platform, referred to as the median plateau, and two narrow, elongated structural highs trending N–S—namely, the Setentrional High to the north and the Meridional High to the south. These highs are separated by major structural elements, specifically the WSW-ENE-oriented Curitiba Lineament, and the NW–SE-oriented Libra

Transfer Zone, both of which further contribute to the internal segmentation of the field (Chagas et al., 2024).

The tectonic compartmentalization of the Libra Block exerted a first-order control on the distribution and emplacement of magmatic bodies. Magmatism occurs predominantly within the pre-salt section of the northwestern compartment, in the pre- and intra-salt intervals of the central compartment, and across the pre-, intra, and post-salt sections in the southeastern compartment (Fig. 10). This spatial variation reflects the influence of major basement structures—particularly the Libra Transfer Zone (NW–SE) and the Curitiba Lineament (WSW–ESE)—which acted as preferential zones for magma ascent (Rancan et al., 2018). Fault evolution also played a significant role: according to Zhao et al. (2019), the main regional faults remained active throughout the rift phase, from the Piçarras to the Barra Velha formations, showing delayed peak activity from west to east, while their later reactivation was crucial for the localization of Santonian intrusive bodies. In contrast, secondary faults were mostly active during the Piçarras and Itapema stages, controlling emplacement of early volcanic features that subsequently guided the distribution of extrusive rocks.

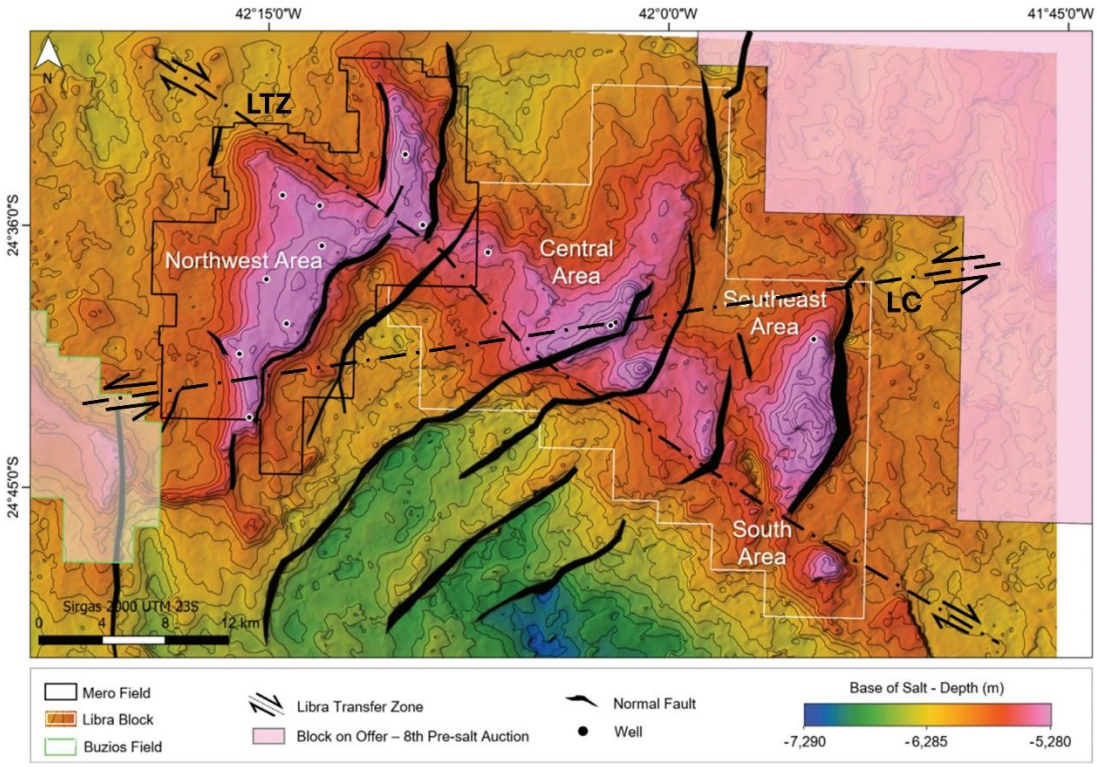

Figure 9. Base of salt structural map of the Libra Complex. Modified from Petersohn et al., 2021; additional annotation (Curitiba Lineament LC) added by the author based on the interpretation of Chagas et al., 2024.

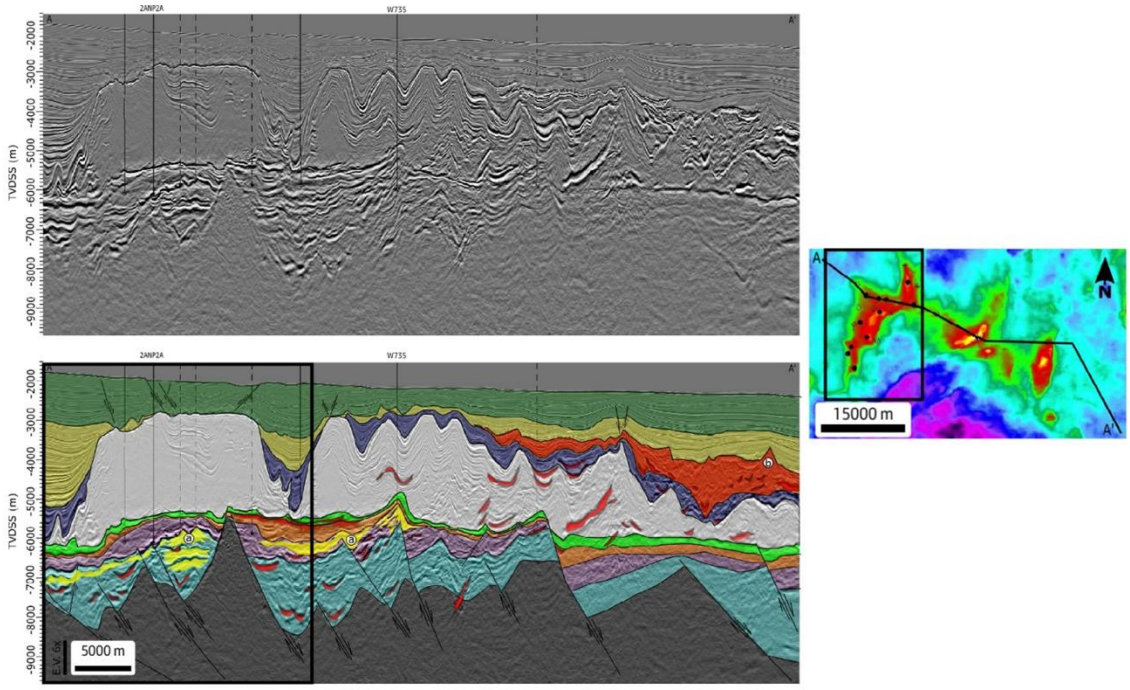

Figure 10. Seismic section in amplitude and corresponding interpretation across the Libra Complex, focusing on the Mero Field. Features highlighted in red represent igneous intrusions, whereas those in yellow correspond to subaerial lava flows. The figure illustrates the stratigraphic distribution of magmatic bodies as controlled by tectonic compartmentalization (after Chagas et al., 2024).

2.3.2 Stratigraphy

The stratigraphic sequence of the Mero Field begins over the crystalline basement and is represented by Eocretaceous rocks of the Camboriú Formation (Moreira et al., 2007). This unit, composed predominantly of basalts, constitutes the economic basement of the Santos Basin and records the onset of rifting. Overlying it, the K36 sequence filled the structural depressions formed during the rift phase, being characterized by igneous and pelitic rocks deposited in early lacustrine contexts. On the eastern flank of the Mero median plateau, intercalations of pelites with igneous rocks are observed, whereas in higher sectors, especially in the northern high, sandstones and lithic conglomerates containing basement fragments also occur, associated with igneous material (Chagas et al., 2024).

The following sequence, K38, corresponds to the Itapema Formation, whose sedimentary thickness is highly irregular in the area. This unit, bounded by the Pre-Jiquiá Unconformity at the base and the Pre-Alagoas Unconformity at the top, is

composed predominantly of coquinas, which represent the most characteristic lithofacies of the formation. These deposits are interpreted as having originated in high-energy lacustrine environments developed during transgressive–regressive cycles. The main reservoirs associated with the Itapema Formation consist of bioclastic rudstones and grainstones, frequently interbedded with subordinate pelitic levels (Chagas et al., 2024).

Above the Itapema Formation lie the rocks of the Barra Velha Formation, which represent the main reservoir unit of the pre-salt. Traditionally interpreted as the product of sedimentation within a shallow lacustrine system (Carminatti et al., 2009), these rocks, however, reflect the coexistence of two distinct depositional environments: a deeper system, characterized by non-reservoir facies rich in argillaceous sediments, and a shallower system, restricted to structural highs, where the carbonate facies with better reservoir quality developed (Gomes et al., 2020). Recent evidence also indicates a significant hydrothermal contribution to the deposition of the carbonates in this unit (Farias et al., 2019).

The lower portion of the Barra Velha, corresponding to the K44 sequence, is bounded by the Pre-Alagoas and Intra-Alagoas Unconformities and is composed of intraclastic grainstones interbedded with stromatolites, with smaller proportions of spherulites and laminites (Chagas et al., 2024).

The upper portion of the Barra Velha Formation, corresponding to sequences K46–K48, is bounded at the base by the Intra-Alagoas Unconformity (DIA) and at the top by the base of the evaporites of the Ariri Formation. This interval represents the transition between the lacustrine system and the shallow-marine to evaporitic environment. The Upper Barra Velha facies exhibit strong structural control: on narrow and elongated highs, stromatolites and carbonate breccias forming large towers are found, whereas on the median plateau, laminites and spherulites occur together with these facies. Regardless of the structural position, grainstones and rudstones derived from the reworking of in situ facies are common (Chagas et al., 2024).

The rocks of the Barra Velha Formation include both in situ deposits—such as shrub-like and dendritic stromatolites, spherulites, and laminites—and reworked facies composed of stromatolitic fragments, intraclasts, and peloids. Several

depositional models—biotic, abiotic, or hybrid—have been proposed to explain the occurrence and development of the Barra Velha Formation carbonates (Carminatti et al., 2009; Dorobek et al., 2012; Wright & Barnett, 2015; Saller et al., 2016; Farias et al., 2019). It is now recognized that their characteristics reflect a complex carbonate system formed by the interaction between biotic and abiotic processes, including organic activity and ascending hydrothermal fluid flows along fractures, which influenced the lake's chemistry (Wright & Barnett, 2015; Chafetz et al., 2018).

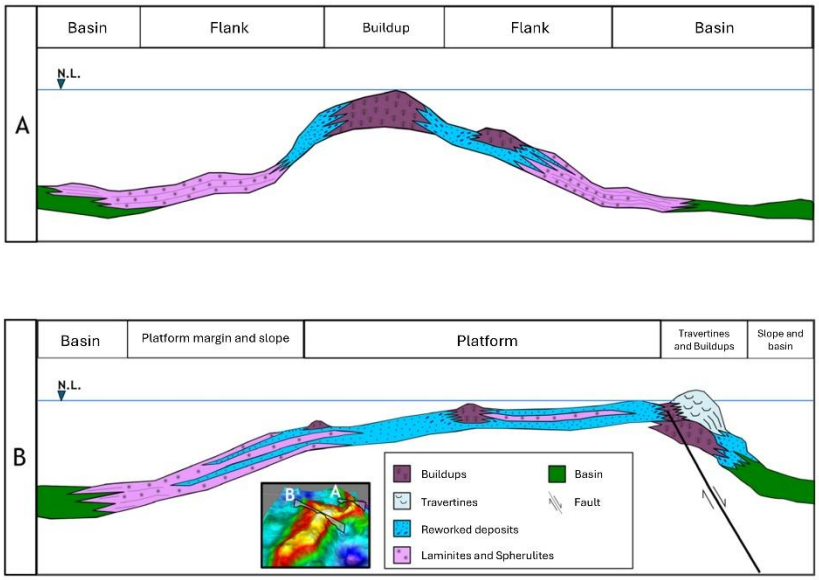

Figure 11. Schematic cross-sections illustrating the depositional model of the Barra Velha Formation in the Mero Field (after Chagas et al., 2024).

2.3.3 Igneous Rocks

Two magmatic suites have been identified in the Libra block. The first, of Barremian–Aptian age, has tholeiitic affinity and is composed predominantly of basalts—massive or vesicular—with minor diabase, hyaloclastite, and redeposited hyaloclastite facies, indicative of subaqueous volcanism (Chagas et al., 2024; Rancan et al., 2018). These tholeiitic rocks were dated by the $^{40}Ar/^{39}Ar$ method in the central sector where they yield minimum ages of 125.5 ± 0.7 Ma and evidence of alteration at ~114 Ma (Rancan et al., 2018). Well data indicate that they are mainly emplaced within the Itapema Formation and locally within the

Piçarras Formation. Seismic data suggest that in the northwestern compartment, these rocks are concentrated within depressions between basement structural highs—rift-related half-grabens—where they form lenticular seismic facies or thin, plane-parallel/subparallel facies with divergent patterns interpreted as lava deltas filling rift depressions (Rancan et al., 2018). Rancan et al. (2018) report a magmatic structural high at the intersection of the Libra Transfer Zone and the Curitiba Lineament in the central compartment. In seismic data, part of these early intrusions exhibits saucer-shaped forms associated with hydrothermal venting and layered/stratified forms tied to volcanic edifices (Oliveira et al., 2019; Oliveira et al., 2024).

The second suite, of Santonian–Campanian age, comprises hypabyssal alkaline rocks such as diabase, gabbro, alkaline basalt, and lamprophyre. Their $^{40}Ar/^{39}Ar$ ages range from 83.3 ± 0.7 Ma to 72.4 ± 4.9 Ma, with alteration dated at ~49.9 ± 0.4 Ma, suggesting probable Eocene hydrothermal overprinting (Rancan et al., 2018). These intrusions are generally located near the top of the Barra Velha Formation (K46–48) but also occur within the Itapema Formation (Chagas et al., 2024; Rancan et al., 2018). Marins et al. (2025) proposed an emplacement model where the alkaline suite is linked to a deep complex plumbing system concentrated within lithospheric discontinuities, from which the magma differentiates and migrates through reactivated basement faults (Fig. 12). According to the authors, magma emplacement was also guided by stratigraphic controls, preferentially exploiting rudstone–laminite contacts and laminite beds of the “Lula’s Fingers Stratigraphic Marker” (LFSM). These intrusions locally compartmentalize the carbonate reservoirs into box-work blocks, affecting their internal connectivity and flow behavior. On seismic data, alkaline igneous bodies commonly appear as medium to high-impedance reflections and have been organized into three main groups by geometry and stratigraphic position: (i) pre-salt sills, spanning flat to canopy-like and transgressive forms; (ii) intrusions within the evaporitic interval—most prominent in the central and southeastern sectors—where they follow stratified salt layers and gradually transgress upward into younger levels; and (iii) post-salt bodies, where inclined and branching intrusions form sill complexes that are locally associated with volcanic edifices (Rancan et al., 2018; Oliveira et al., 2019) (Fig. 13).

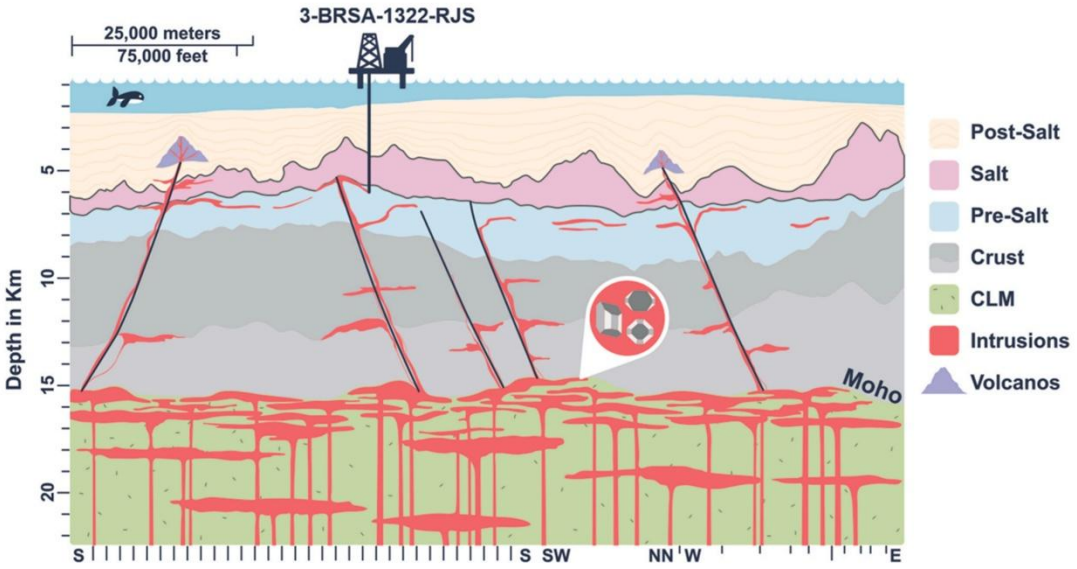

Figure 12. Schematic model illustrating the emplacement of Santonian–Campanian intrusions in the Mero Field (after Marins et al., 2025).

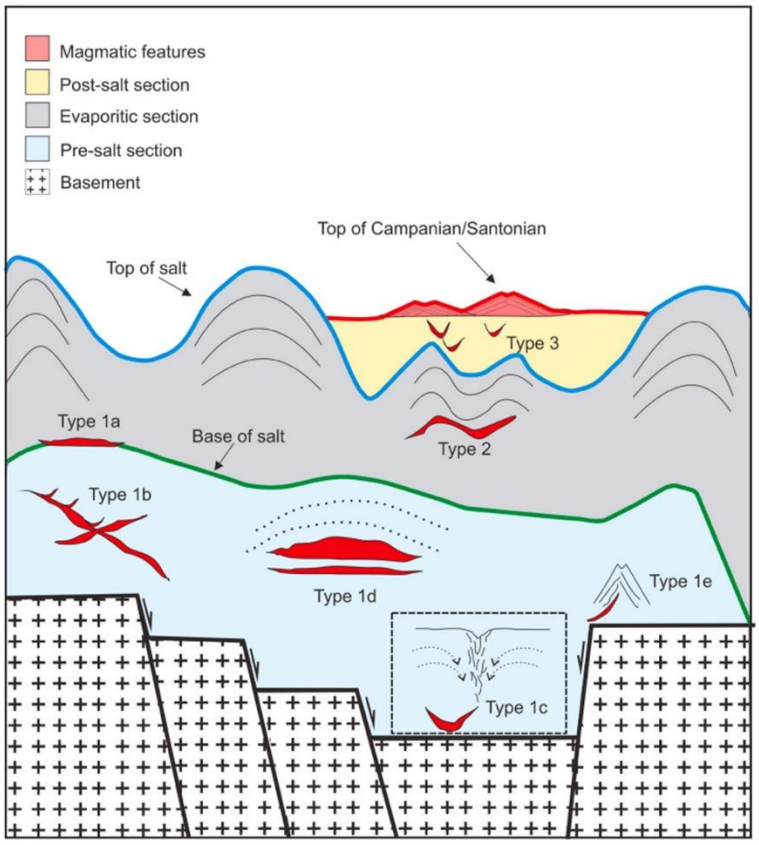

Figure 13. Types of sills from the two magmatic suites found in the Libra area (after Oliveira et al., 2019).

3. Spectral Decomposition: Principles and Main Approaches

The following discussion is primarily based on the works of Chopra and Marfurt (2024) and Barnes (2016), with adaptations and reformulations for the present study.

Spectral decomposition is a seismic interpretation technique that analyses how the frequency content of a seismic signal varies through time. A seismic trace can be regarded as a superposition of multiple frequency components generated by constructive and destructive interference between reflection events. The objective of spectral decomposition is to separate these components and evaluate their temporal and spatial distribution. By transforming the data into the time–frequency domain, it becomes possible to identify frequency-dependent variations in amplitude and phase that relate to thin-bed tuning, lithological contrasts, and subtle stratigraphic changes — features that are often obscured in conventional broadband amplitude data.

This mathematical operation is made possible by the Fourier transform, which converts a time-domain function into its frequency-domain representation through the Fourier integral. In practice, it transforms a seismic trace into its frequency spectrum, showing how the signal's energy is distributed across the available bandwidth. In its most general form, a transform is composed of two complementary operations: a forward transform (or decomposition), which expresses the seismic signal as a sum of simpler components, and an inverse transform (or reconstruction), which reassembles these components to reproduce the original signal. Fourier analysis is the simplest example, where the data are cross-correlated with a set of sine and cosine functions of fixed frequencies. Each correlation coefficient defines a complex frequency component, and the collection of these coefficients constitutes the signal spectrum. When all components are equally weighted in reconstruction, the transform is said to be linear. In contrast, nonlinear transforms introduce adaptive weighting or selection of the dominant components to enhance temporal or spectral resolution and better highlight meaningful features in the data.

Most spectral decomposition techniques can be viewed as applications of filter banks, where the seismic signal is analysed through a suite of narrow-band filters, each centered at a particular frequency and collectively spanning the full seismic bandwidth (Barnes, 2016). In practice, filter banks are implemented using complex wavelets—such as Morlet or Gabor wavelets—that act as band-pass filters centered on discrete frequencies. The filtered outputs represent the energy or reflection strength within each frequency range and can be displayed as frequency-specific amplitude maps or as three-dimensional volumes. These frequency attributes are commonly combined using RGB corendering, in which low, intermediate, and high frequencies are assigned to the red, green, and blue color channels, respectively. The resulting composite images emphasize subtle stratigraphic variations: red hues generally indicate thicker packages (dominant low frequencies), green intermediate thicknesses, and blue thinner beds dominated by high frequencies.

Because seismic signals are nonstationary—their frequency content varies with time due to attenuation and scattering—the classical Fourier transform, which assumes stationarity, cannot capture these local variations. To overcome this, time-localized transforms are used. Three approaches are particularly common in seismic applications: the Short-Time Fourier Transform (STFT), the Continuous Wavelet Transform (CWT), and the Matching Pursuit Decomposition (MPD).

3.1 Short-Time Fourier Transform (STFT)

The STFT applies the Fourier transform to successive, overlapping segments of the seismic trace, defined by a fixed-length time window—typically of rectangular or Gaussian shape and often around 100 ms in practical applications (Chopra & Marfurt, 2024). This approach improves the localization of spectral information compared to the standard Fourier transform but imposes a constant trade-off between time and frequency resolution. A shorter window provides better temporal localization but blurs the frequency content, while a longer window sharpens the spectral resolution at the expense of temporal precision. Moreover, because the same window length is used for all frequencies, the STFT cannot adapt to the differing temporal scales of high- and low-frequency components. As a result, high-frequency reflections may be smeared, and low-frequency ones truncated

(Sun et al., 2002). The fixed analysis window also leads to vertical stratigraphic mixing on time slices, sometimes giving a false impression of lateral continuity (Leppard et al., 2010, cited in Chopra & Marfurt, 2023).

3.2 Continuous Wavelet Transform (CWT)

The CWT overcomes the fixed-window limitation by using variable-length wavelets whose duration is proportional to their period. In this way, low frequencies are analysed with longer windows and high frequencies with shorter ones, ensuring that each wavelet contains an approximately constant number of oscillations. This property allows both narrow-band ringing and broadband impulsive reflections to be positioned more accurately in time. Mathematically, the CWT consists of convolving the seismic trace with a scaled and shifted version of a chosen mother wavelet ψ(t,τ,s), where τ represents time translation and s is a scaling factor controlling frequency. The transform thus produces a two-dimensional time–scale representation for each trace, equivalent to applying a bank of band-pass filters spanning the seismic spectrum.

Several mother wavelets can be employed, including Morlet, Ricker, Mexican Hat, Derivative of Gaussian (DoG), Shannon, and Chakraborty wavelets (Fig. 14). Among these, the Morlet and Ricker wavelets are most common because their shapes resemble typical seismic wavelets. The Morlet wavelet, in particular, consists of a complex sinusoid modulated by a Gaussian envelope, offering a good balance between temporal and spectral localization. In practice, the choice of the mother wavelet depends on data characteristics and may vary between datasets. The Morlet wavelet often yields more stable and interpretable results, but no single wavelet can be considered universally optimal. The CWT's frequency-dependent windowing makes it particularly well suited to nonstationary seismic data, offering a better balance of time and frequency localization than the STFT. It can also be regarded as a bank of logarithmically spaced band-pass filters, which naturally adapts to the scale of the analysed frequencies. Nevertheless, some degree of vertical mixing and interference may still occur, especially in the presence of thin beds or noise.

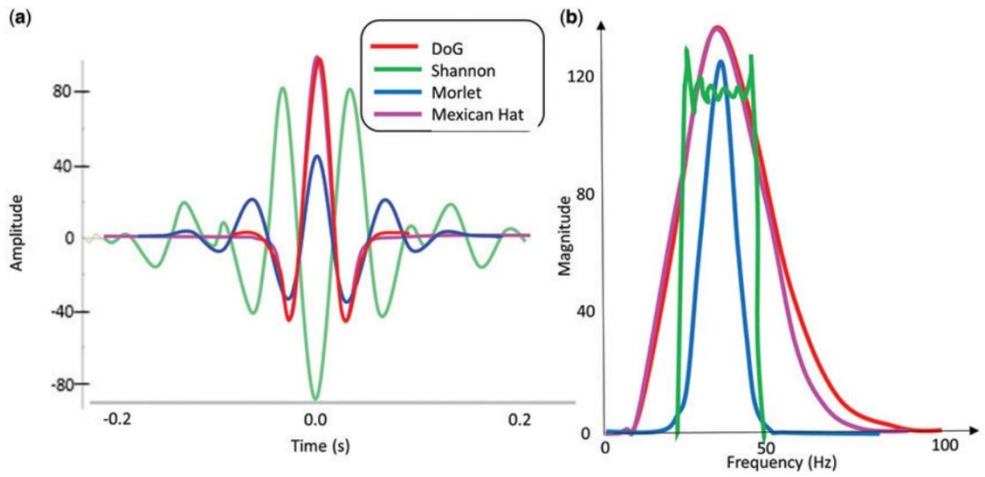

Figure 14. Diagram showing the Morlet (blue), Mexican Hat (purple), DoG (red), and Shannon (green) wavelets in (a) the time domain and (b) the frequency domain, together with their spectra (after Chopra and Marfurt, 2024).

3.3 Matching Pursuit Decomposition (MPD)

The Matching Pursuit Decomposition is a more recent and computationally demanding method designed to achieve higher time–frequency resolution. It is based on the concept of sparse representation, where the seismic trace is modeled as a sum of a small number of localized wavelets ("atoms") drawn from a predefined dictionary, typically composed of complex Morlet or Ricker wavelets defined at discrete frequency intervals (e.g., every 0.5 Hz) (Fig. 15). The algorithm iteratively identifies and subtracts the most energetic event from the data, then repeats the process on the residual signal until the remaining energy is negligible. At each iteration, the selected wavelet maximizes the projection of the residual signal onto the dictionary, ensuring that the residual energy decreases progressively (Mallat & Zhang, 1993). In doing so, MPD reconstructs the signal as a sequence of significant reflections while minimizing redundancy. Because it adaptively selects the wavelets that best fit the data, MPD yields time–frequency representations with less vertical smearing and stratigraphic mixing than the CWT or STFT (Leppard et al., 2010, cited in Chopra & Marfurt, 2023). The resulting spectral volumes are often more continuous and better defined, although the method is more sensitive to noise and computationally intensive.

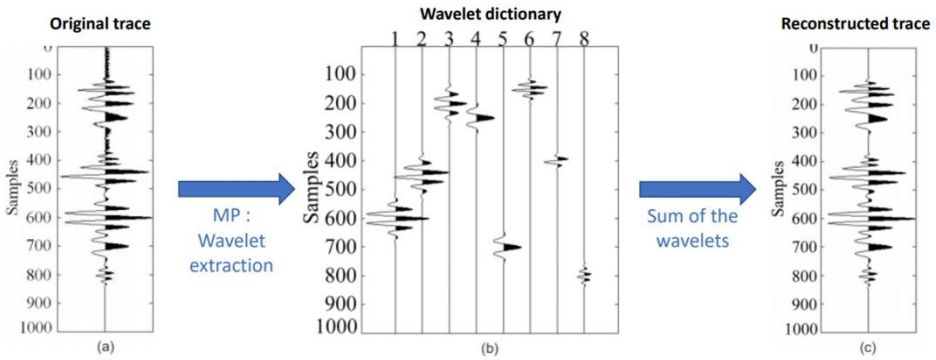

Figure 15. Schematic illustration of the Matching Pursuit decomposition process. Starting from the original seismic trace, individual wavelets of different frequencies are iteratively extracted and summed to reconstruct the signal. The resulting trace is nearly identical to the original but with reduced noise content (after Eliis material).

3.4 Comparison of Time–Frequency Decomposition Methods

Different spectral decomposition methods yield results that may vary in sharpness, continuity, and interpretability. The Short-Time Fourier Transform (STFT), Continuous Wavelet Transform (CWT), and Matching Pursuit Decomposition (MPD) all transform the seismic signal into the time–frequency domain, but the nature of their filter banks—and whether the transform is linear or nonlinear—controls the character of the resulting images and attributes (Fig. 16).

A key aspect influencing the interpretability of spectral volumes is vertical mixing, which occurs when reflections from different stratigraphic levels interfere within the same analysis window. In map view, this effect may cause unrelated geological events to appear blended together, producing apparent lateral continuity or “echoes” of deeper reflectors at shallower levels. The extent of this mixing depends directly on the type of filter bank applied: the STFT, with its fixed-length sliding window, behaves as a constant-bandwidth filter bank that averages spectral content over time, often generating broader, overlapping frequency responses. The CWT, employing wavelets whose length varies inversely with frequency, corresponds to a logarithmic filter bank and achieves improved temporal localization, reducing but not eliminating this mixing. The MPD, on the other hand, adaptively selects individual wavelets from a predefined dictionary—functioning as a dynamic, nonlinear filter bank—and models only the most energetic events. By iteratively subtracting these from the signal, it minimizes redundancy and

produces a sparse representation in which each reflection is described by a single, well-defined frequency component (Fig. 17).

The reduction of redundancy in MPD translates into both superior temporal resolution and enhanced spectral definition: frequency components overlap less, and thin-bed or channel-related anomalies appear sharper and more isolated. Linear transforms such as the STFT and CWT reconstruct the signal by summing all frequency components with equal weight, which provides robustness but limits contrast between neighbouring events. The nonlinear, adaptive nature of the MPD emphasizes dominant features and attenuates background interference, producing cleaner time–frequency images and more continuous stratigraphic expressions. However, this same sensitivity makes MPD more susceptible to noise and small amplitude variations, which can introduce spurious lateral variability in the resulting attributes. In addition, because it relies on an iterative and computationally intensive process, MPD is generally restricted to smaller volumes—typically cropped around the reservoir interval—whereas STFT and CWT can be applied efficiently to full-field seismic cubes, providing rapid generation of frequency maps used to identify depositional elements.

Despite these practical limitations, MPD remains the preferred method when the objective is to derive geobodies (Fig. 18) or quantitative frequency-based volumes, as its high temporal resolution and minimal mixing produce more compact and realistic representations of the subsurface. Conversely, STFT and CWT are often favored for regional-scale reconnaissance, where the balance between processing efficiency and spectral fidelity provides an effective first-pass interpretation. These differences are readily apparent in spectrograms and RGB frequency blends, where STFT images show diffuse frequency patches, CWT results display smoother, scale-dependent patterns, and MPD volumes highlight discrete, high-contrast anomalies that better correspond to stratigraphic boundaries or thin-bed interference zones.

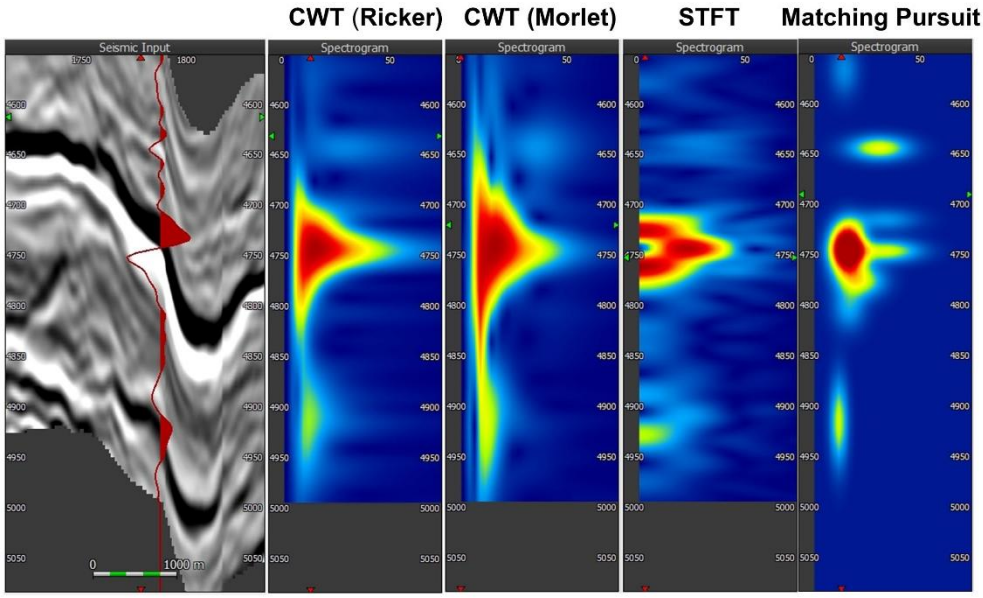

Figure 16. Comparison of the spectrogram responses obtained from the spectral decomposition of the seismic trace indicated in red on the section. The Matching Pursuit method provides the most accurate representation in the spectrogram, both in time and in frequency.

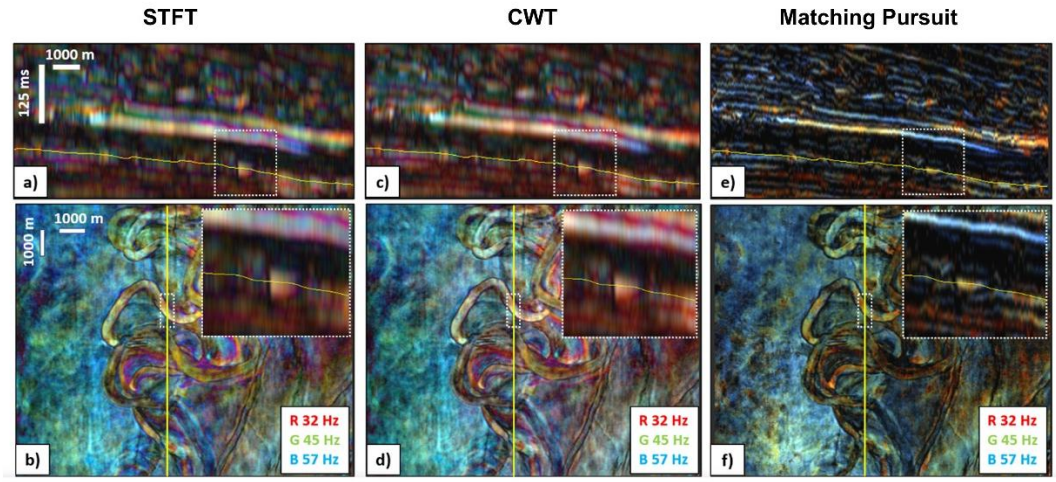

Figure 17. RGB-blended comparison between STFT, CWT, and Matching Pursuit spectral decomposition results, shown in both volume and horizon views for the same frequency range. STFT and CWT present similar vertical smearing effects, whereas Matching Pursuit delivers more sharply defined features in volume and reduced colour blending on the horizon slice (after Evano and Cubizolle, 2022).

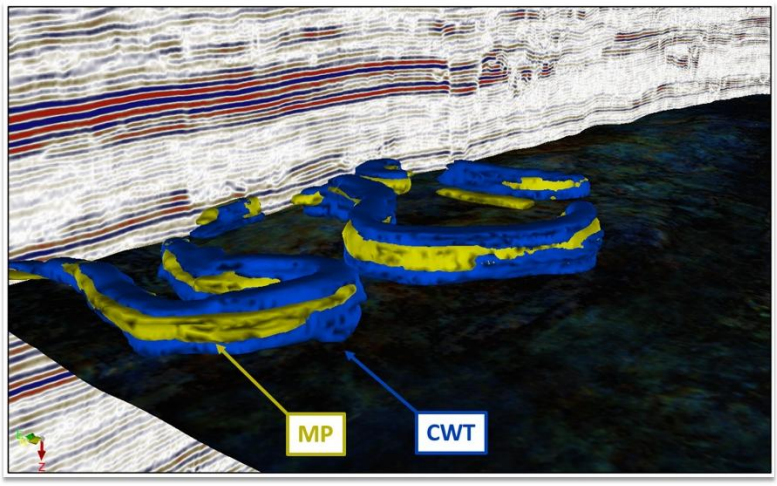

Figure 18. Comparison between two channel geobodies extracted from spectral decomposition attributes. The CWT-derived geobody (blue) is more voluminous than the one obtained from Matching Pursuit (yellow), a difference attributed to the lower temporal resolution inherent to the CWT method (after Eliis material).

3.5 RGB and HSV/HSL Blending

RGB blending is traditionally used to visualize the results of spectral decomposition. It consists of three colour filters — R (red), G (green), and B (blue) — each assigned to a different spectral component. Typically, low frequencies are mapped to red, intermediate frequencies to green, and high frequencies to blue. Each filter contains values ranging from low to high magnitudes, which are displayed through a saturation scale representing spectral magnitude at each spatial location. The blended image separates spectral components by colour, with the overlap of two components producing intermediate hues between the primary red, green, and blue filters, and the combination of all three yielding white (Fig. 19). Conversely, when no significant magnitude is present in any of the three components, the area appears dark. This simple yet powerful blending technique allows interpreters to analyse depositional systems — such as fluvial channels — with visual clarity, revealing subtle details of internal architecture. Moreover, it provides a qualitative indication of relative bed thickness, with thicker geological features commonly highlighted in red and thinner ones in blue.

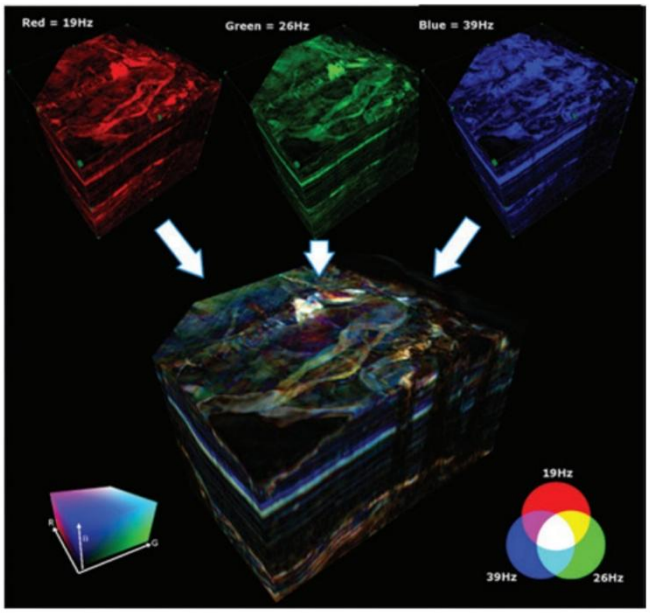

Figure 19. Example of three spectral-component volumes blended using RGB visualization, successfully enhancing the expression of channel features (after McArdle et al., 2011).

While the RGB model is most suitable for displaying three attributes of the same family and comparable value ranges, other colour models can represent attributes of different nature or dimensionality. Although the HSV (Hue–Saturation–Value) blending method is not traditionally applied to spectral decomposition, it is introduced here as part of the workflow implemented for the Matching Pursuit decomposition used in this study. The HSV model is a cylindrical colour space in which hue (H) represents the base colour along a circular scale — progressing from red through yellow, green, cyan, blue, and magenta before looping back to red — making it ideal for cyclic attributes such as azimuth. Saturation (S) defines colour intensity or purity, controlling the transition from vivid tones to grey, while value (V) describes the overall brightness of the colour. Together, these three parameters determine the visual expression of the combined attributes (Chopra & Marfurt, 2024) (Fig. 20a).

In seismic interpretation, HSV blending is commonly used to visualize relationships between dependent attributes. A typical example is dip azimuth and dip magnitude: when the dip magnitude approaches zero, the azimuth value becomes unreliable. In such cases, the colour associated with the azimuth is

desaturated toward grey, indicating low confidence (Chopra & Marfurt, 2024). Practically, hue corresponds to the primary attribute (e.g., azimuthal direction), saturation modulates colour intensity based on a secondary attribute (e.g., dip strength or confidence), and value controls brightness (from dark to light) according to a third variable.

A closely related model, HSL (Hue–Saturation–Lightness), functions in a similar way but replaces brightness with lightness, which adjusts the luminance of the combined attributes, limiting the final colour toward black or white (PaleoScan User guide) (Fig. 20b).

The HSV blending applied to igneous rock detection using the Matching Pursuit decomposition offers an alternative to RGB visualization and will be discussed in the next chapter, *Methodologies*.

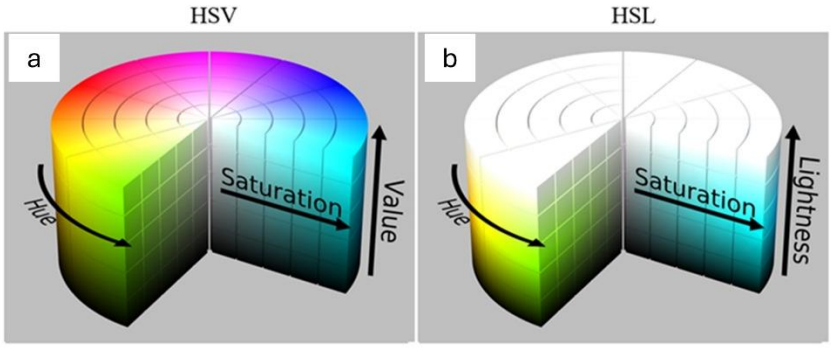

Figure 20. Representation of the HSV (Hue–Saturation–Value) and HSL (Hue–Saturation–Lightness) blending models as cylindrical colour spaces (figure modified from Wikipedia).

4. Methodologies

4.1 Dataset

For the purposes of this study, a Reverse Time Migration (RTM) seismic volume reprocessed by Viridien in 2016 and made public in 2021 was used. It encompasses the Libra Block but was later cropped around the Mero Field for the implementation of the workflow described in the following sections. The dataset is provided in depth domain, with a bin size of 25 m in both inline and crossline directions and a sampling interval of 5 m. A corresponding interval velocity model in depth was also employed, enabling the conversion of the seismic volume into the time domain when required.

In addition, five previously interpreted depth horizons were available: Top of Salt, Intra-Alagoas (K44), Pre-Alagoas (K38), Pre-Jiquiá (K36), and Top of Basement. Twenty-five public exploration and production wells, drilled by Petrobras—most of them located within the Mero Field—were incorporated primarily as control points for assessing the spatial and stratigraphic distribution of igneous rocks, supporting the correlation between well data, seismic attributes, and extracted geobodies.

Conventional well logs typically used to recognize igneous intervals in sedimentary basins—such as density (RHOB), sonic, neutron porosity (NPHI), resistivity, and gamma ray (GR)—prove to be insufficient within the pre-salt interval. This limitation arises from the fact that carbonates often exhibit physical properties close to those of magmatic rocks, particularly in terms of acoustic impedance. Moreover, upward-migrating hydrothermal fluids, which are widespread in the pre-salt, may either enhance or degrade carbonate properties through cementation or dissolution, further complicating the geological interpretation of the logs.

In addition to intrusive bodies, extrusive and volcaniclastic facies may also occur, introducing further variability in density. Igneous intrusions themselves may be fractured or altered at their bases, affecting the log signatures. Given this diversity of factors influencing the log responses, the identification of magmatic rocks based solely on conventional logs in the pre-salt sequence can be challenging.

For these reasons, the use of lithogeochemical profiles provided a more effective means of lithological discrimination. The DWAL, DWCA, and DWFE logs represent elemental concentrations of aluminium, calcium, and iron, respectively. These lithogeochemical curves proved particularly valuable for distinguishing characteristic signatures of igneous lithologies, such as basalts and diabases—marked by elevated aluminium and iron contents and a pronounced decrease in calcium concentration—from the surrounding carbonates. In most cases, the lithogeochemical profiles showed very good consistency with the composite logs.

For production wells, composite logs were not available, consequently the interpretation relied exclusively on lithogeochemical data. Most of these wells, however, did not display clear signatures comparable to those observed in wells with log composites, where igneous rocks are typically characterized by distinctive lithogeochemical responses. In uncertain cases, core description reports were occasionally consulted when possible. As this study focuses on igneous bodies detectable in seismic data, small-scale variations observed in well logs were not considered particularly relevant. For quality-control purposes, only wells exhibiting clear lithogeochemical signatures of igneous rocks could be reliably used as control points for their detection. Consequently, wells lacking composite logs and without clear lithogeochemical responses were regarded as not having penetrated *significant* igneous intervals—a classification that also served as quality-control for the interpretation of attributes and geobodies.

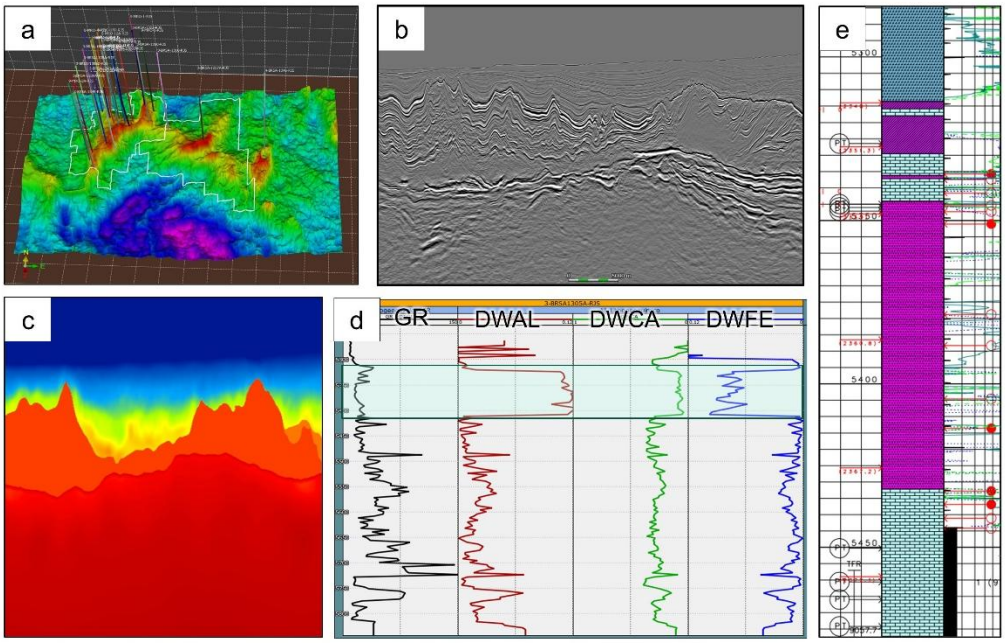

Figure 21. Dataset used in this study. (a) Structural map showing the base of salt and well locations; (b) RTM seismic volume; (c) velocity model; (d) lithogeochemical logs, where the typical igneous rock signature is highlighted in light blue; (e) composite log.

Well name	Top B.V	Within B.V	Within Itapema	Within Piçarras
2-ANP-2A-RJS				
3-BRSA-1255-RJS				
3-BRSA-1267A-RJS				
3-BRSA1305A-RJS				
3-BRSA-1310-RJS				
3-BRSA-1322-RJS				
3-BRSA-1339A-RJS				
3-BRSA-1342A-RJS				
3-BRSA-1343-RJS				
3-BRSA-1345-RJS				
3-BRSA-1350-RJS				
3-BRSA-1353D-RJS				
3-BRSA-1355D-RJS				
3-BRSA-1356D-RJS				
4-BRSA-1346-RJS				
8-MRO-4-RJS				
9-MRO-1-RJS				
9-MRO-2A-RJS				
9-MRO-5-RJS				
7-MRO-3-RJS				
7-MRO-6DB-RJS				
8-MRO-11-RJS				
8-MRO-14D-RJS				
8-MRO-13D-RJS				
9-MRO-9DA-RJS				

Table 1. List of wells in the database with composite logs and/or lithogeochemical data. Orange cells indicate the presence of igneous rocks in the corresponding interval. The pale orange shading denotes intervals where igneous rocks are inferred only from lithogeochemical trends, with no clear diagnostic signature, and therefore remain uncertain.

4.2 Data Conditioning of the Post-stack Volume

The present study was carried out primarily using PaleoScan™ software, developed by Eliis.

Workflow applied to the post-stack depth volume

The following conditioning steps were applied to the original seismic volume with the objective of improving data quality within the pre-salt interval—by reducing noise, equalizing the frequency content, and broadening the bandwidth. Finally, the lowest frequencies inherited from the deconvolution process were removed (Fig. 22).

This conditioning was essential to optimize the result of the spectral decomposition using the Matching Pursuit method—a high-resolution technique that, however, is highly sensitive to noise.

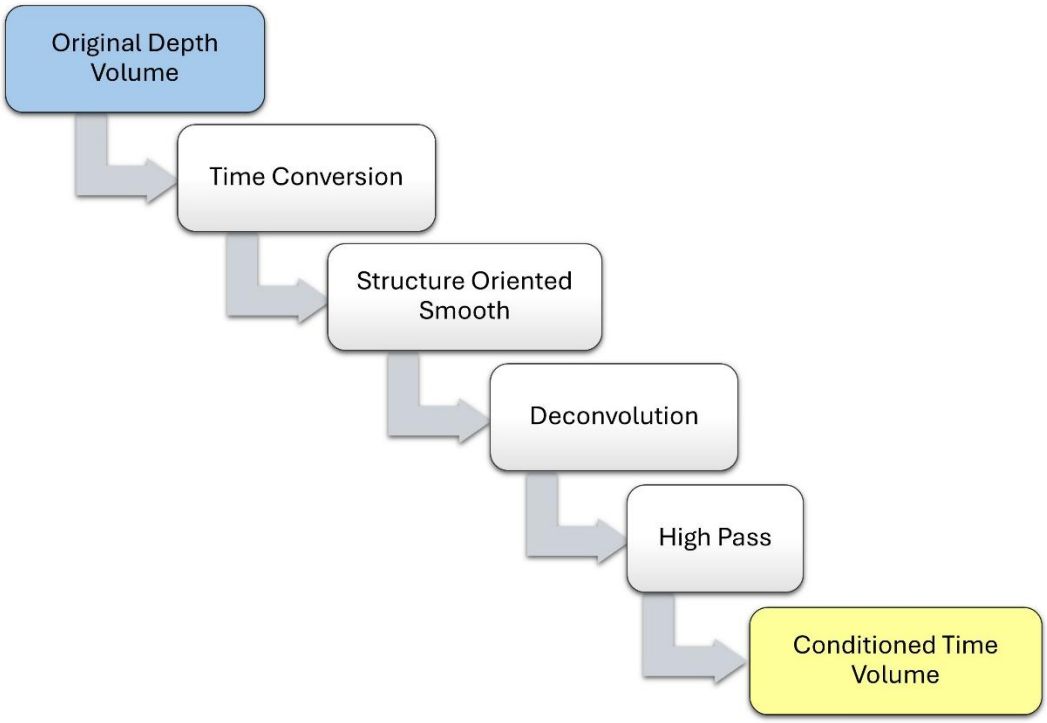

Figure 22. Main steps of the workflow applied to convert the original depth-migrated volume into a conditioned time-domain volume.

Structure Oriented Smooth

The Structure-Oriented Smoothing (SOS) technique is designed to enhance seismic data by reducing noise while preserving the integrity of structural and stratigraphic features. Unlike conventional filters that apply uniform smoothing in all directions, this method adapts the filtering process to the orientation of the seismic reflectors.

In practice, a 3D vector field is computed throughout the seismic volume, representing the local dip and azimuth of the reflections. The smoothing operation is then applied along these structural directions, ensuring that amplitudes are averaged following the reflector geometry rather than across it. This approach minimizes the blurring of discontinuities such as faults or stratigraphic boundaries.

The Structure-Oriented Smoothing implemented in PaleoScan™ is based on the approach described by Hale (2009), as reported by Wu and Hale (2015). The software allows the user to adjust two parameters before applying the filter: spatial deviation (px) and vertical deviation (px). In this study, the default values—7.00 and 3.00, respectively—were adopted (Fig. 23).

By applying smoothing guided by the dip of seismic amplitudes, this method is particularly well suited to minimize noise while preserving the integrity of seismic events. Its application prior to the deconvolution process was essential to prevent further amplification of noise and to ensure a more stable input for subsequent spectral decomposition.

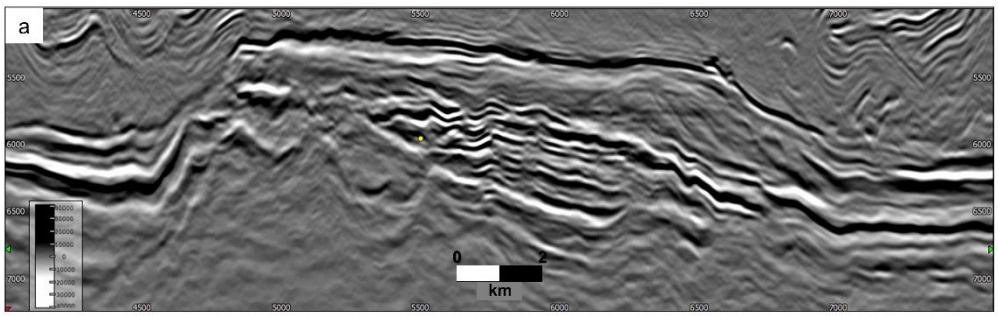

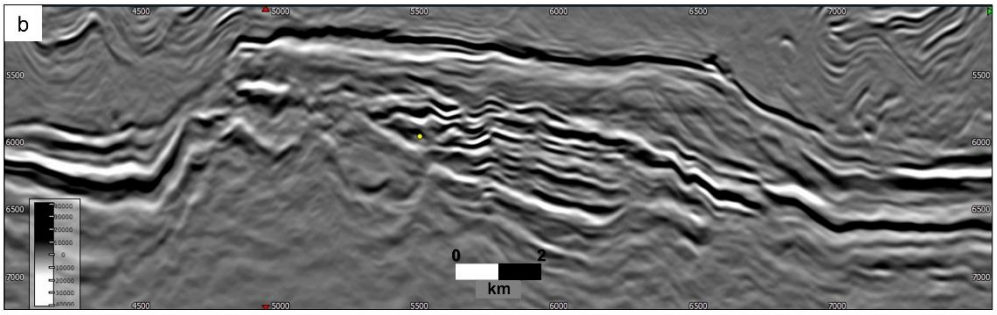

Figure 23. (a) Original seismic volume; (b) volume after application of the Structure-Oriented Smoothing filter.

Deconvolution

Seismic traces can be represented as the convolution between a wavelet and the subsurface reflectivity series, expressed as:

$$s(t) = w(t) * r(t)$$

where s(t) is the recorded seismic signal, w(t) the source wavelet, and r(t) the sequence of reflection coefficients (Goupillaud, 1961; Wuenschel, 1960). This convolutional model results in the recorded trace being a band-limited version of the earth's reflectivity, as the finite frequency bandwidth of the seismic wavelet smears and overlaps adjacent reflection events.

Deconvolution is the inverse process of convolution, aiming to remove the wavelet effect and recover an estimate of the reflectivity series (Fig. 24a). In practice, it enhances the vertical resolution of seismic data by compressing the wavelet and broadening the effective frequency bandwidth (Yilmaz, 2001, cited in Madrinovella & Pranowo, 2022) (Fig. 24b). The procedure involves estimating or assuming a representative wavelet and applying an inverse filter that minimizes its imprint on the seismic trace. The ultimate goal is to obtain a signal that more closely approximates the true reflectivity of the subsurface by reducing the noise and distortions introduced by the source and acquisition system. As a result, reflection events become sharper and more continuous, and thin beds or subtle stratigraphic features can be more readily identified, improving the overall interpretability of the seismic dataset.

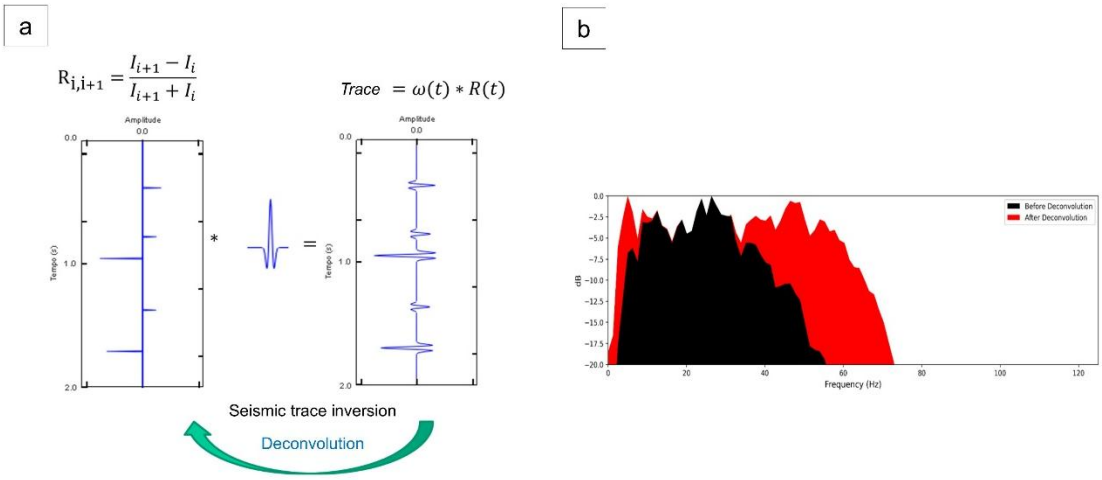

Figure 24. (a) Seismic trace inversion concept (after Lupinacci); (b) Typical Amplitude spectrum before (black) and after (red) deconvolution (after Madrinovella and Pranowo, 2022).

The deconvolution algorithm applied in this study is the Fast Iterative Shrinkage-Thresholding Algorithm (FISTA), originally proposed by Beck and Teboulle (2009). FISTA belongs to the class of iterative shrinkage-thresholding algorithms designed to solve linear inverse problems commonly encountered in signal and image processing. It preserves the computational simplicity of the classical ISTA (Iterative Shrinkage-Thresholding Algorithm) while achieving a substantially faster rate of convergence, both theoretically and practically (Beck & Teboulle, 2009).

The deconvolution was applied to the seismic volume after conversion from depth to time and the application of the Structure-Oriented Smoothing filter. For wavelet estimation, a vertical analysis window between 4500 and 6100 ms was defined. Two parameters were systematically tested—the stabilization term and the number of iterations—to evaluate their influence on the deconvolution output and to determine the configuration that produced the most reliable result.

The stabilization term (ε) is a small positive constant added to the denominator of the inverse filter to prevent divisions by very small values close to zero that would cause numerical instabilities. In practice, it acts as a regularization factor, limiting excessive amplification of noise at frequencies with low signal energy. If chosen too small, the filter becomes unstable and amplifies noise; if too large, it behaves like a smoother, reducing sharpness and frequency content. Therefore,

the stabilization term must not be too small nor too large, as the optimal value represents a trade-off between sharpness and stability. In this study, the optimal stabilization term was set to 2×10^{-2} (Fig. 25).

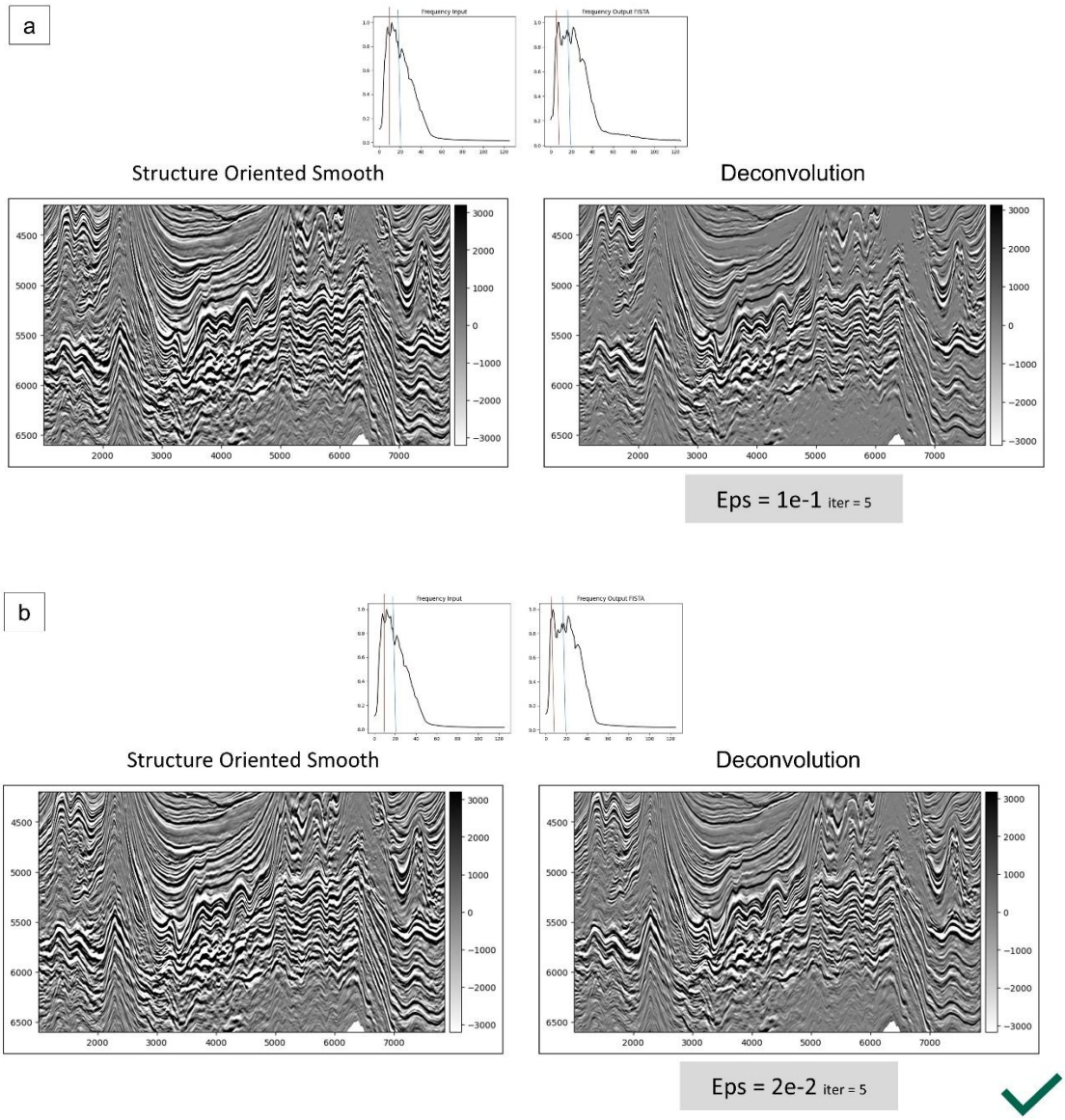

Figure 25. Tests of the stabilization term. Comparison between the input volume (Structure-Oriented Smoothing, SOS) and the output volume (Deconvolution), shown in seismic section and corresponding amplitude spectrum. (a) Eps = 1×10^{-1} (b) Eps = 2×10^{-2}.

The number of iterations defines how many times the algorithm refines the solution by minimizing the misfit between the observed and reconstructed traces. Too

few iterations lead to under-corrected results, whereas an excessive number causes the algorithm to overfit noise, producing spurious high-frequency artifacts and unrealistically sharp reflectors. We set the number of iterations to five. Increasing the value to ten did not produce a noticeable difference in the visual appearance of the deconvolved volume. However, the amplitude spectrum indicated a noticeable boost of the high-frequency content (Fig. 26). This increase, however, is associated with the amplification of high-frequency noise rather than a genuine gain in resolution.

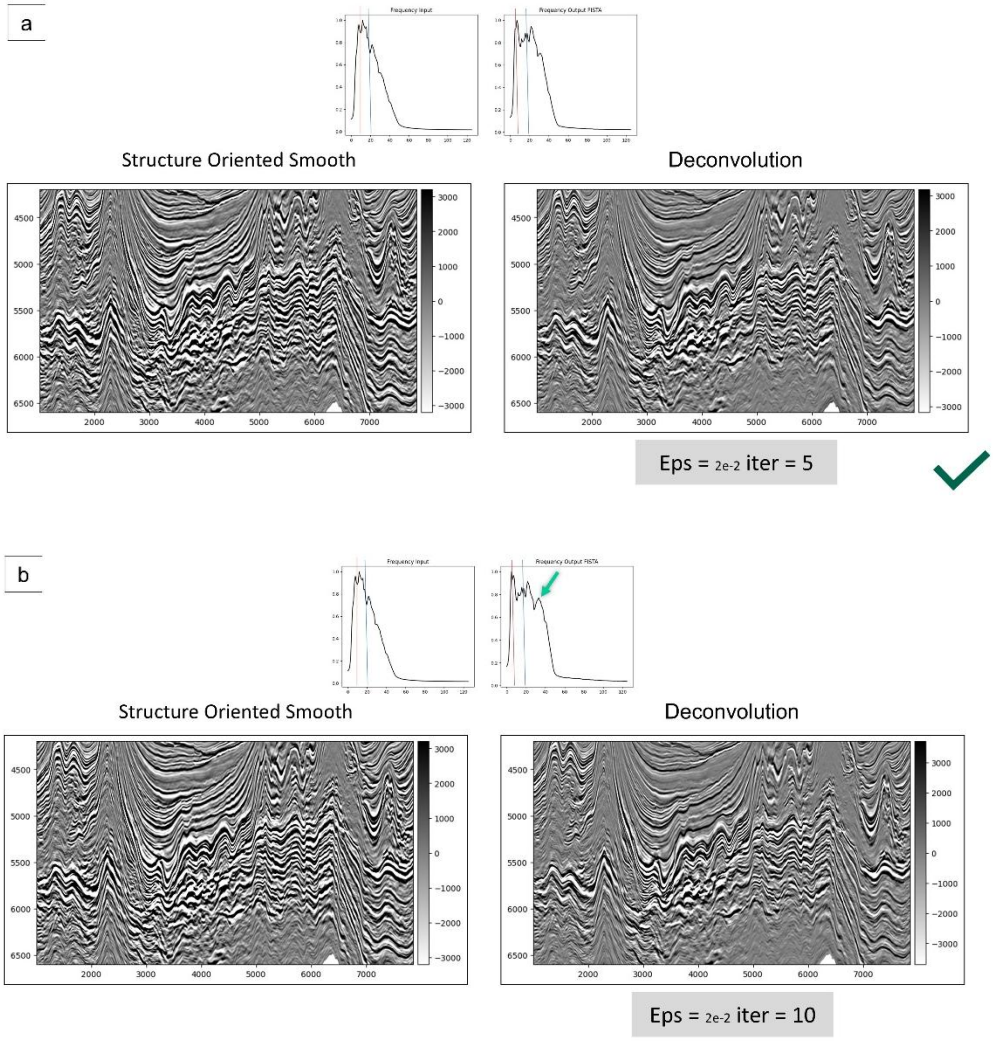

Figure 26. Tests of the iteration number. Comparison between the input volume (Structure-Oriented Smoothing, SOS) and the output volume (Deconvolution), shown in seismic section and corresponding amplitude spectrum. (a) Iter = 5 (b) Iter = 10.

High Pass

A high-pass filter allows high-frequency components of a signal to pass through while attenuating those below a defined cut-off frequency (Fig. 27). The degree of attenuation applied to lower frequencies depends on the specific characteristics and design of the filter.

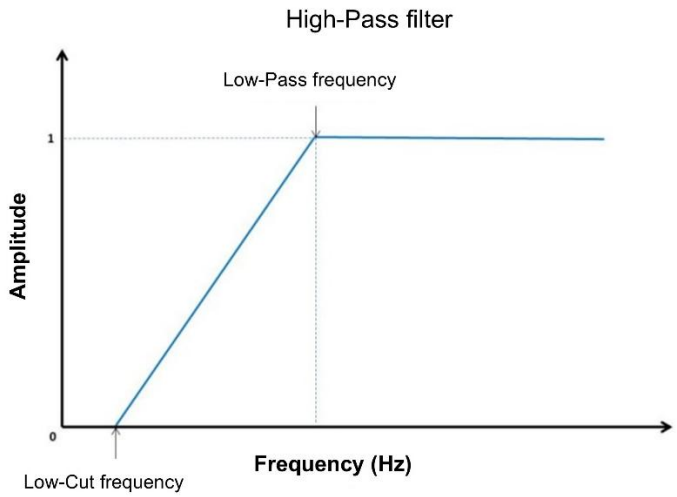

Figure 27. High-Pass filter defined by its Low-Cut frequency and Low-Pass frequency (after PaleoScan User guide).

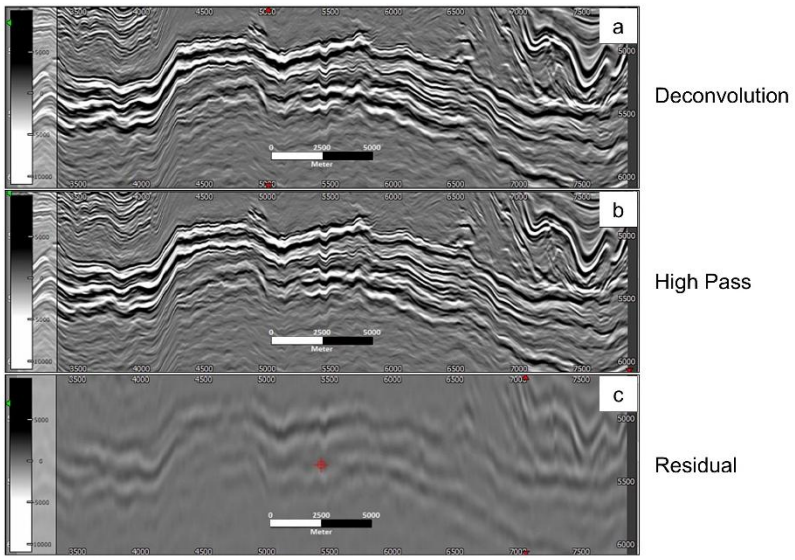

Figure 28. Seismic sections showing (a) the deconvolved volume, (b) the high-pass–filtered volume, and (c) the residual volume.

After the deconvolution was applied to the seismic volume, an increase in low-frequency energy was observed, as expected from this type of processing. Because this frequency range can introduce artefacts into the data, a Ricker-type high-pass filter with a cut-off frequency of 5 Hz was subsequently applied to suppress undesired low-frequency components.

Comparison of Conditioning Results

The conditioning sequence applied to the original seismic volume—comprising Structure-Oriented Smoothing, Deconvolution, and High-Pass Filtering—progressively improved data quality. The first step removed random noise, the second broadened the frequency spectrum through deconvolution, and the final step attenuated the low-frequency noise introduced during this process. The amplitude spectrum at each stage of the conditioning workflow is shown in Figure 29.

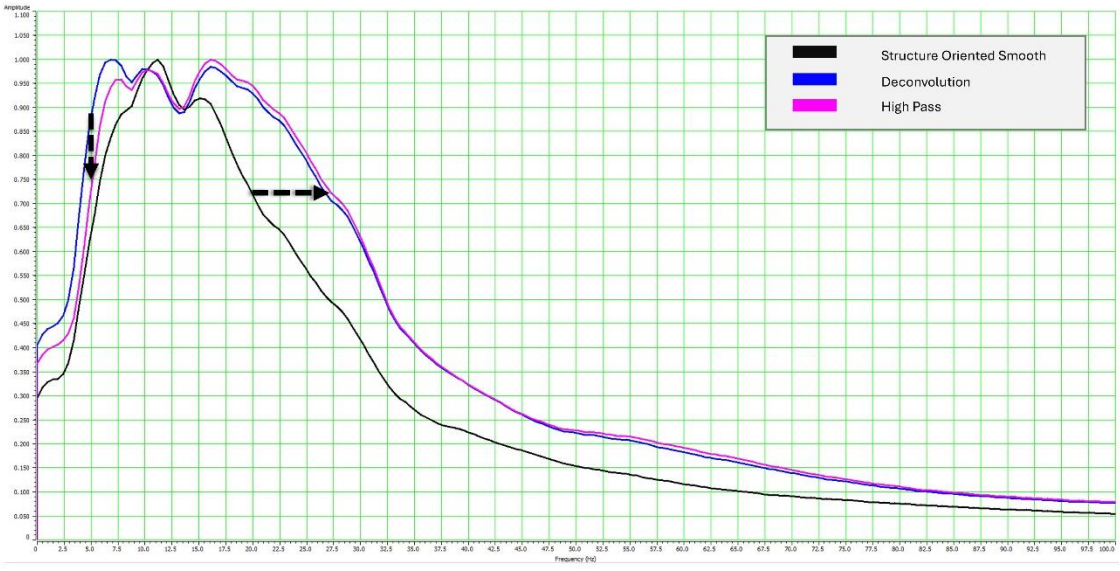

Figure 29. Amplitude spectrums extracted from cropped volumes of the pre-salt section. In black: SOS volume. In pink: volume after deconvolution. In blue: final volume with High-Pass applied.

The conditioned seismic volume served as the input for the subsequent Matching Pursuit decomposition. Figure 30 compares the results of the Matching Pursuit for selected frequency components (medium and high) applied to the original volume, the deconvolved volume, and the final high-pass-filtered dataset. The conditioning significantly enhanced seismic reflections, yielding improved lateral

continuity and definition of thin events, particularly within the higher-frequency band (around 30 Hz). A noticeable reduction in the density of short, low-coherence reflections—previously associated with noise—was also observed. Overall, the conditioned volume appears cleaner and more coherent, providing a more reliable input for the Matching Pursuit workflow and enhancing the interpretability of the resulting spectral attributes.

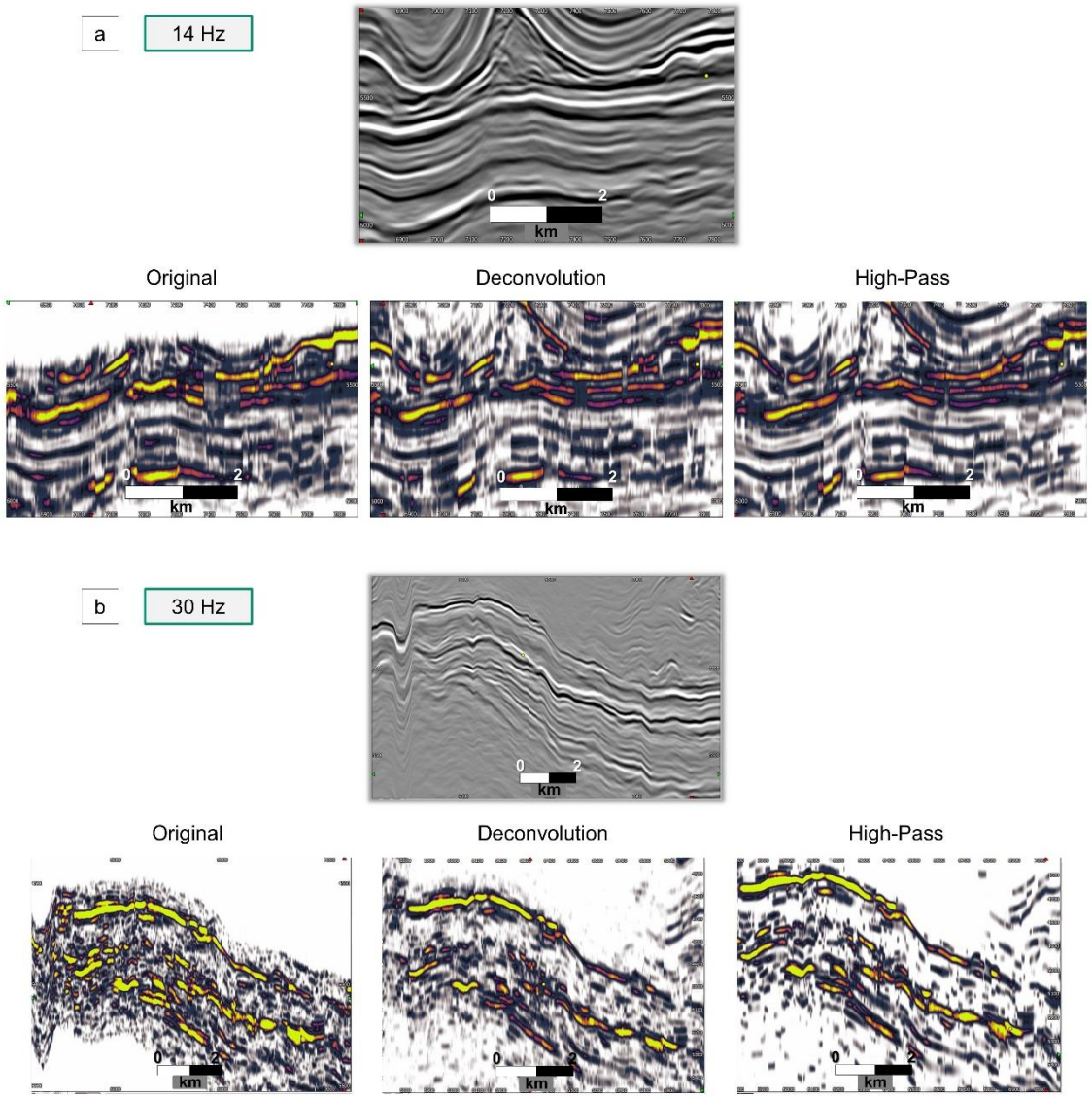

Figure 30. Comparison of the Matching Pursuit spectral components at 14 Hz (a) and 30 Hz (b), obtained from the original, deconvolved, and high-pass–filtered seismic volumes.

4.3 Workflow applied with Matching Pursuit Decomposition

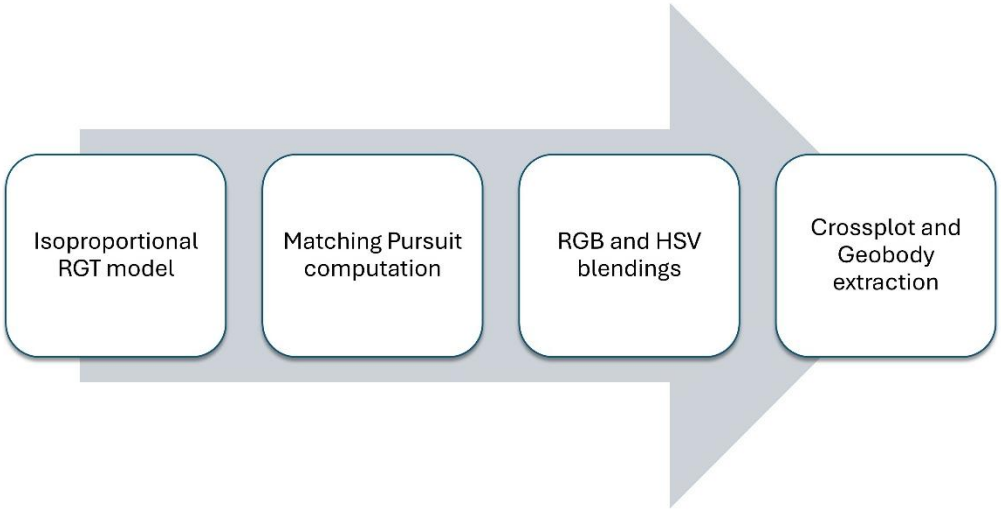

Figure 31. Schematic workflow applied to the analysis and implementation of the Matching Pursuit methodology.

Isoproportional RGT Model Creation

Firstly, the interpreted surfaces were used to construct an isoproportional Relative Geological Time (RGT) model in PaleoScan (Fig. 32). Although the software provides advanced technology capable of tracking every seismic trace and correlating them to build a signal-based Relative Geological Time model, an isoproportional approach was adopted in this study to ensure consistency with previous interpretations. The resulting model, which assigns a relative geological age to each voxel within the seismic volume, enabled the generation of a continuous set of intermediate surfaces between the main unconformities used as input. This was achieved through the creation of a native PaleoScan object known as the Horizon Stack. The Horizon Stack consists of a sequence of horizons extracted from the geomodel and provides a powerful framework for rapid and comprehensive screening of seismic attributes when mapped onto it. In this study, a Horizon Stack comprising 41 surfaces was generated. These surfaces were initially analysed through spectral decomposition maps, but their primary role was to serve as the basis for geobody extraction.

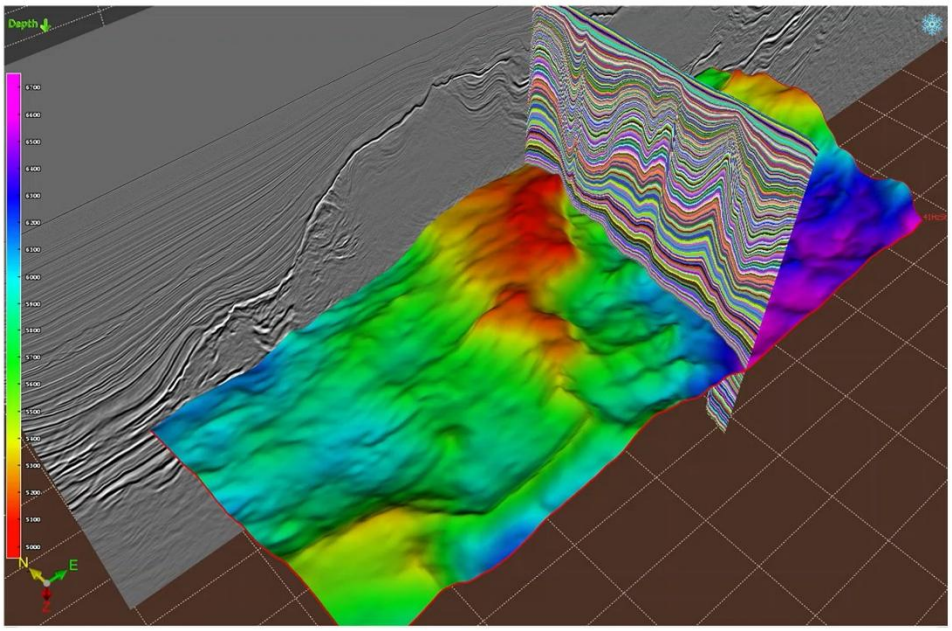

Figure 32. 3D visualization combining an amplitude seismic line, a seismic line from the isoproportional RGT model, and the uppermost surface from the Horizon Stack.

Matching Pursuit Volume Computation

After the conditioning of the seismic volume in the time domain, the Matching Pursuit algorithm (following the classical formulation of Mallat and Zhang, 1993) was applied, resulting in the generation of twelve spectral decomposition volumes. Each volume corresponds to a specific frequency, selected based on the analysis of the spectrogram. As discussed in the dedicated chapter, Matching Pursuit is a high-resolution spectral decomposition technique in which frequency components exhibit minimal overlap compared to conventional algorithms. Spectral anomalies are represented in the spectrogram by narrow frequency ranges—typically 4 to 6 Hz for low-frequency anomalies and 15 to 20 Hz for high-frequency ones. The selected frequencies—6, 8, 10, 12, 14, 16, 18, 20, 25, 30, 35, and 40 Hz—were chosen according to the spectral signature of the main features of interest. For instance, the diabase bodies overlying the Barra Velha Formation, which commonly generate a thick composite reflector due to interference between strong amplitudes at the base of the anhydrite, the top of the tight carbonate, and the igneous intrusion itself, display a pronounced response in the very low-frequency range (typically between 6 and 10 Hz). The characteristic

frequency ranges associated with each key feature are further discussed at the beginning of the next chapter.

Once the spectral decomposition volumes were generated, each was converted to the depth domain using the velocity model, which had previously been transformed from depth to time. This step was essential for enabling the analysis of results within seismic sections, facilitating the recognition of features previously interpreted in the depth domain and allowing direct correlation with well data.

RGB and HSV Blending

The Matching Pursuit volumes converted to depth were subsequently mapped onto the Horizon Stack and used to generate arbitrary seismic lines intersecting the wells. Initially, RGB blending was applied to visualize the results of the spectral decomposition by combining frequency components over a broad range (10, 20, and 30 Hz). Thereafter, HSV blending was preferred, as it proved more effective for highlighting features associated with specific, narrower frequency bands. In addition, RMS (Root Mean Square) amplitude volumes and maps were generated to provide a complementary analysis based solely on amplitude contrasts. A fixed vertical analysis window of seven samples was used for this purpose.

Volume Cross plot and Geobody extraction

Several factors limit the effectiveness of horizon-based mapping for the identification and spatial delineation of igneous features. Spectral decomposition is not a windowed attribute, meaning that each mapped horizon represents only the attribute value at a specific vertical position. In addition, horizon mapping involves interpolation, which may locally introduce inaccuracies. This limitation is further compounded by the fact that igneous intrusions frequently crosscut the stratigraphy. As a result, a single spectral map often fails to provide a faithful depiction of the full geometry of such features.

To better capture an entire feature of interest, spectral decomposition can be mapped onto a dense Horizon Stack rather than on a limited set of discrete horizons; however, this still prevents the simultaneous visualization of the full

geometry of the feature. To overcome this limitation, geobody extraction was performed over several broader stratigraphic intervals—for example, within the Upper Barra Velha Formation. Geobodies were derived from an HSV blending of three spectral components, followed by cross plot analysis.

The cross plot is an effective tool for displaying the distribution of three input attribute volumes in a two-dimensional space. Typically, the X-axis represents the low-frequency values, the Y-axis corresponds to the medium frequencies, and the high-frequency component is displayed through a colour scale ranging from blue to red via yellow. By interactively painting selected areas on the blended volume, the corresponding data points appear on the cross plot, allowing the creation of classes based on specific frequency combinations. The range of the third input can be further refined using a histogram. Once a class is defined, it can be extracted as a geobody. Several spatial constraints can be applied during extraction; in this study, the Horizon Stack option was used to stratigraphically restrict the extraction to the interval of interest. After extraction, the resulting geobodies can be split and filtered by size, which is particularly useful for removing small, isolated artifacts considered as noise (Fig. 33).

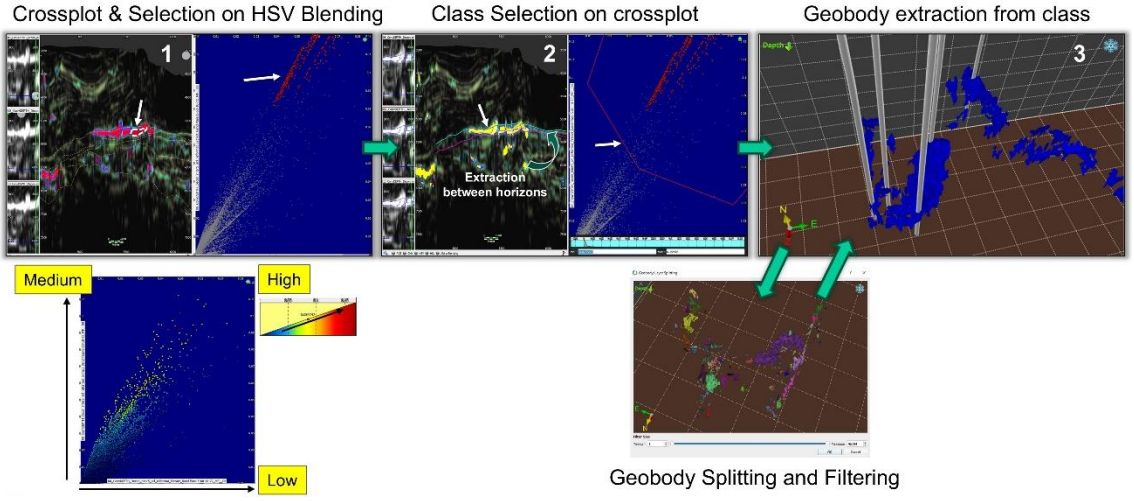

Figure 33. Step-by-step cross plot methodology for extracting geobodies from an HSV blend of three spectral attribute volumes.

5. Results and Discussion

In this chapter, the results of the spectral decomposition obtained using the Matching Pursuit method are presented. First, the different frequency signatures corresponding to each seismic element of interest are shown and discussed. Then, the Matching Pursuit results are compared in seismic sections combining three frequency components, using both RGB and HSV blending, as well as the RMS amplitude attribute. This is followed by the presentation of map-based results at the base of the salt, where certain limitations are discussed and then illustrated. Finally, the geobodies extracted from the volumes are presented and discussed for a series of intervals.

5.1 Typical Signatures on Spectrogram

Igneous rocks occurring within the pre-salt interval, when they have sufficient thickness to be at least detectable in the seismic data, are generally characterized by a strong amplitude contrast. However, as previously described, such a strong amplitude contrast may also be associated with other rock types that exhibit high acoustic impedance values, such as the cemented carbonates typical of the Barra Velha Formation and the anhydrite layer that defines the lower portion of the Ariri Formation. The objective here is therefore to characterize, through their frequency signatures on the spectrogram, the different types of magmatic elements present in the Mero Field–both within the reservoir interval and throughout the pre-salt section as a whole.

The first and most easily identifiable and characterizable elements are the intrusive bodies with a thickness equal to or greater than the vertical resolution of the data (~75 m) (Fig. 34 a). In addition to their strong contrast and size, these bodies tend to cut across the stratigraphy and develop branching patterns, which makes them particularly conspicuous on seismic sections. Due to their thickness, they are defined on the spectrogram by low-frequency responses (6–10 Hz), while their terminations or branches can be captured by intermediate frequencies (12–16 Hz).

Figure 34 b illustrates the frequency signature of most diabase intrusions located at the top of the Barra Velha Formation, between the reservoir top and the base of the salt. The superposition of amplitudes produced by these three high-impedance lithologies results in a strong positive reflector followed by a thicker negative one (Fig. 35). Consequently, the spectrogram exhibits a low-frequency signature (6–10 Hz). However, depending on the relative thickness of the anhydrite and diabase layers, if these are slightly thinner, the frequency interval may broaden and shift toward the mid-frequency range (12–16 Hz).

In contrast, in areas where the base of the salt is in direct contact with the reservoir carbonates—without any igneous intrusion present—the impedance contrast remains high, but the total thickness is comparatively smaller. The frequency signature of the salt base is therefore characterized by higher frequencies on the spectrogram (20–35 Hz) (Fig. 34 c).

Another magmatic element of interest that can be identified by its frequency signature is the basaltic flow located at the base of the Itapema Formation (Fig. 34 d). These flows are primarily concentrated within structural lows, where the Jiquiá Shale is also deposited. The superposition of these two lithologies results in a strong thick negative reflector, underlain by a strong positive reflector of moderate thickness. On the spectrogram, this corresponds to a low-frequency anomaly (6–10 Hz). Thus, the occurrence of lava flows at the base of the Itapema Formation can be inferred in this manner.

Flows interbedded within the Piçarras Formation, on the other hand, are characterized on seismic sections by thin, high-amplitude, subparallel reflections. The frequencies that best capture these reflections are generally high (20–35 Hz), although some may also be better represented by intermediate frequencies (Fig. 34 e).

Finally, intrusions associated with the Piçarras Formation—generally located in its lower part—are characterized by moderate-amplitude reflections that still contrast clearly with the surrounding background. They tend to display typical saucer-shaped geometries and are captured on the spectrogram by low frequencies (6–10 Hz) (Fig. 34 f).

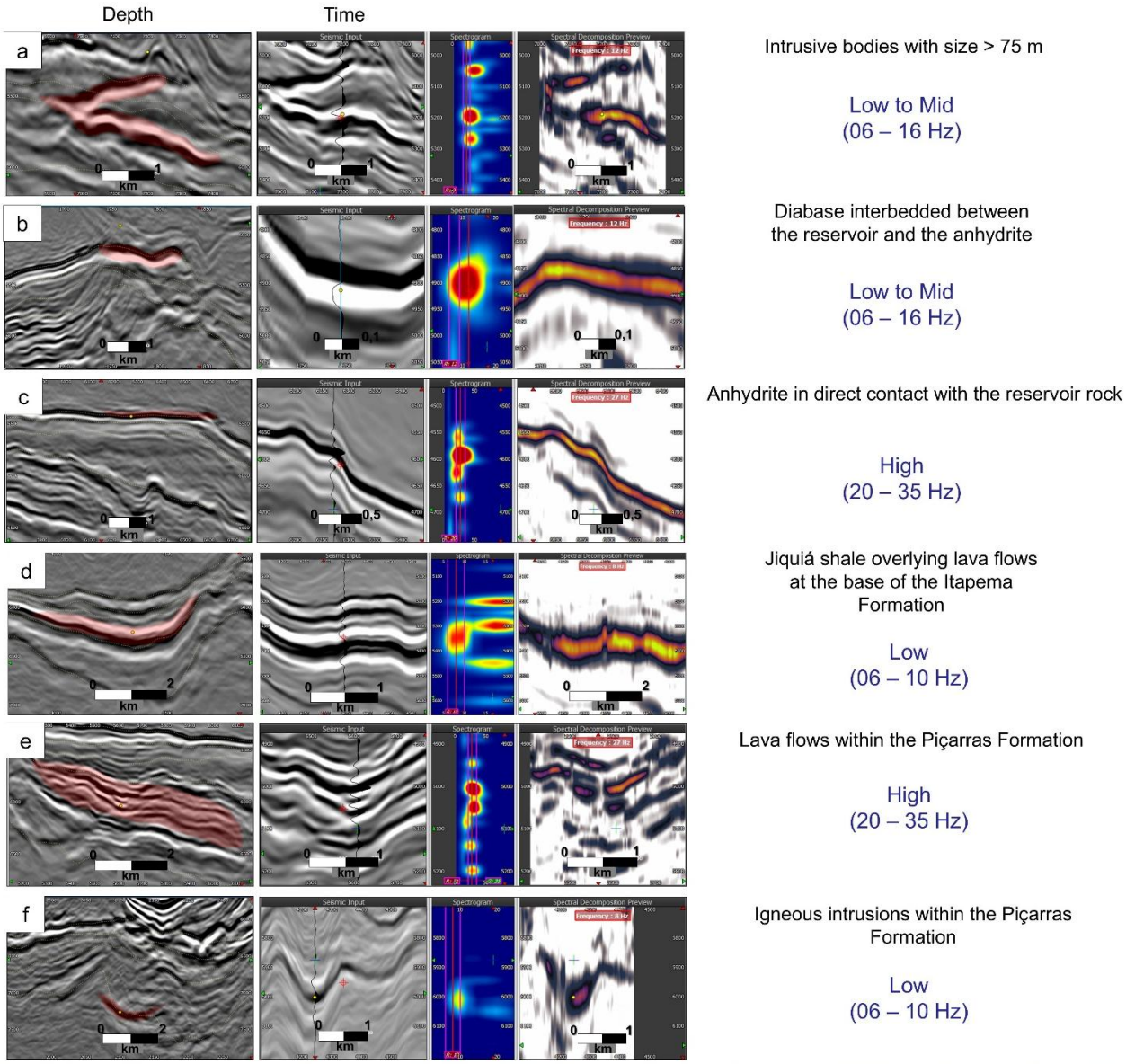

Figure 34. Spectral signatures of the main features of interest in this study. For each case, the seismic section is displayed in both depth and time domains, along with the corresponding spectrogram of the seismic trace shown on the time section and the preview of the magnitude response at the selected frequency.

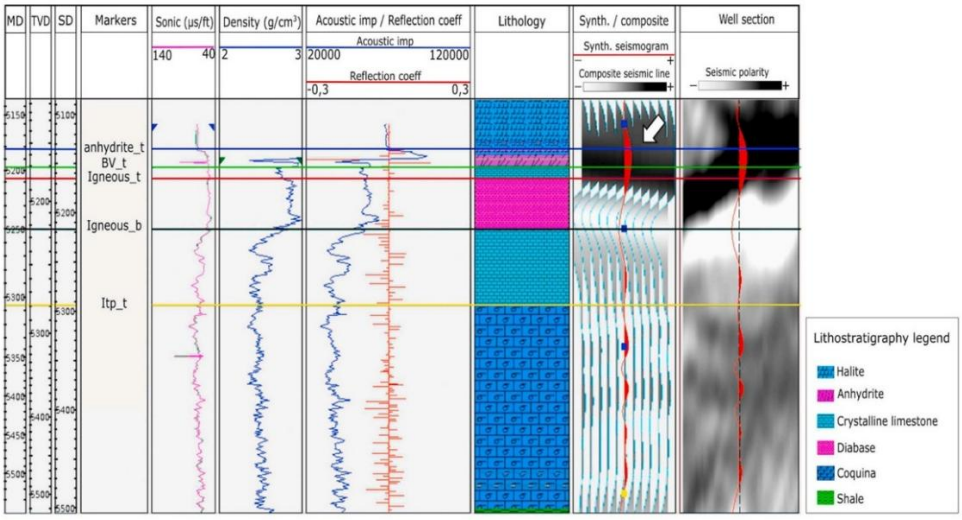

Figure 35. Amplitude response in the seismic data showing two thick reflectors of opposite polarity, resulting from the overlapping impedance contrasts of the anhydrite, diabase, and the top of the reservoir rock (after Oliveira et al., 2024).

5.2 Comparison of attributes and display in seismic volume

Figure 36 compares the same arbitrary seismic line passing through wells 3-BRSA-1322-RJS, 3-BRSA-1255-RJS, 3-BRSA-1305-RJS, 3-BRSA-1356D-RJS, and 3-BRSA-1343-RJS, using different attributes and visualization types. The RMS attribute (Fig. 36 b) highlights all amplitude contrasts, regardless of their spectral components. The RGB blending (Fig. 36 c) separates the contribution of each frequency component into distinct colours. This type of blend is useful when working with widely spaced frequency ranges—in this case, 10, 20, and 30 Hz. It is worth noting that the Matching Pursuit algorithm, designed to minimize redundancy, tends to produce sharp and well-differentiated colour contrasts when displayed in an RGB blend, with little colour mixing. A low-frequency–related noise (in red) can also be observed, which may result from the way the software handles those frequencies.

The figure 36 d shows an HSV blend created from three closely spaced frequencies (12, 14, and 16 Hz). In this line, the features that fall within the mentioned range appear in pink, while the rest of the section appears dark, in subdued green tones. Working with this type of blend—using a frequency range specifically selected for a given feature—has the advantage of enhancing and isolating those

features. For optimal performance, a narrow frequency range must be chosen. Moreover, this approach delineates the limits of features more clearly and geologically, reducing much of the noise observed in the RGB blending and, consequently, improving seismic-line interpretability.

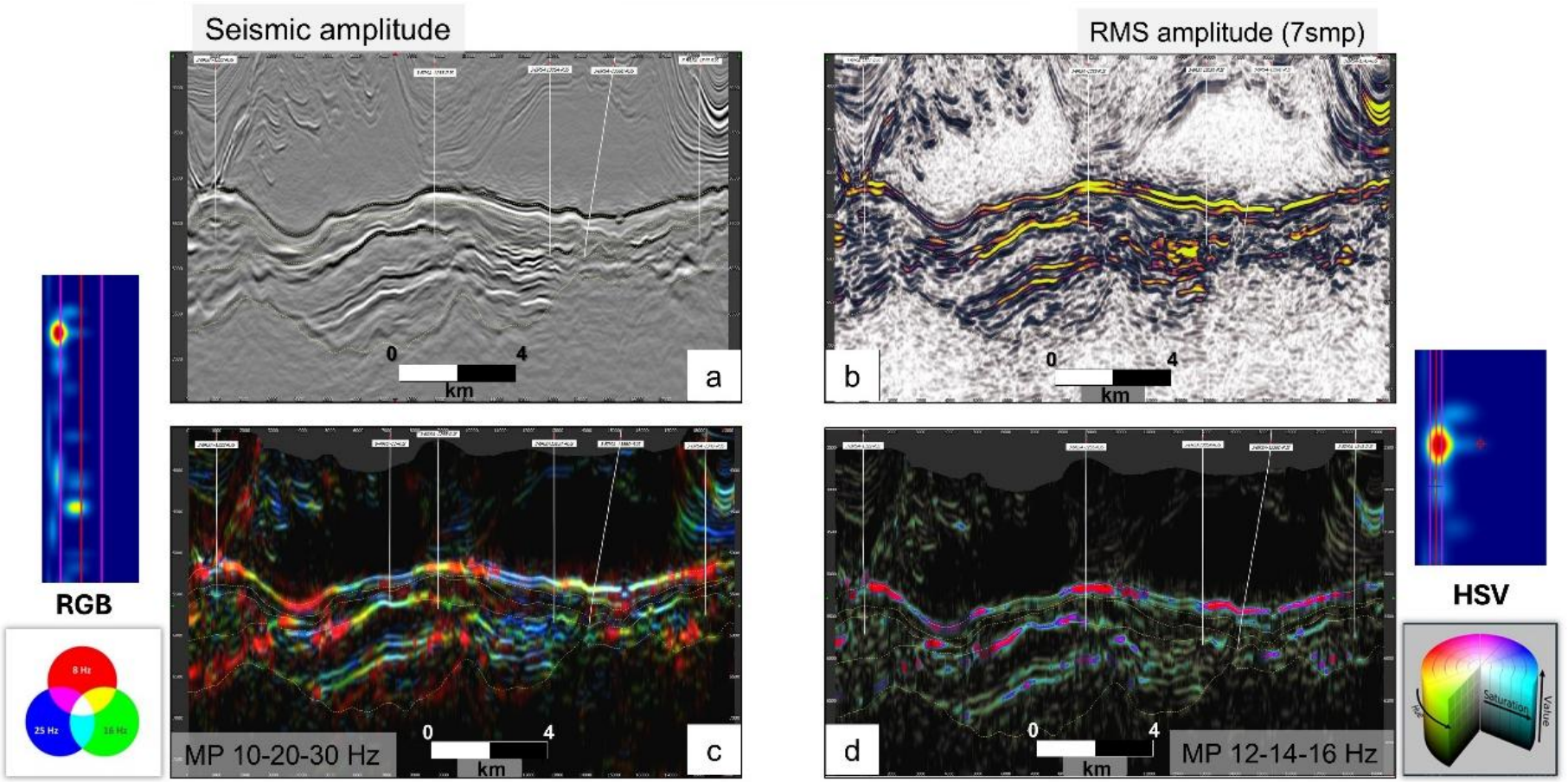

Figure 36. Comparison in seismic section between the amplitude volume, the RMS amplitude attribute (vertical window: 7 samples), Matching Pursuit RGB blend (10–20–30 Hz), and Matching Pursuit HSV blend (12–14–16 Hz), along with their associated spectrograms.

The following figure (Fig. 37) illustrates how a specific frequency range used with HSV blending can either enhance or, conversely, attenuate the top of the Barra Velha (BVE), depending on the presence or absence of diabase. Around well 3-BRSA-1343-RJS, which contains a diabase body of 75 m in thickness, the top of the BVE is enhanced by low frequencies (6, 8, and 10 Hz) (Fig. 37 a), while around well 2-ANP-2A-RJS it becomes dim. Conversely, using a higher-frequency range (20, 25, and 30 Hz) highlights the latter area and suppresses the one containing the diabase (Fig. 37 b).

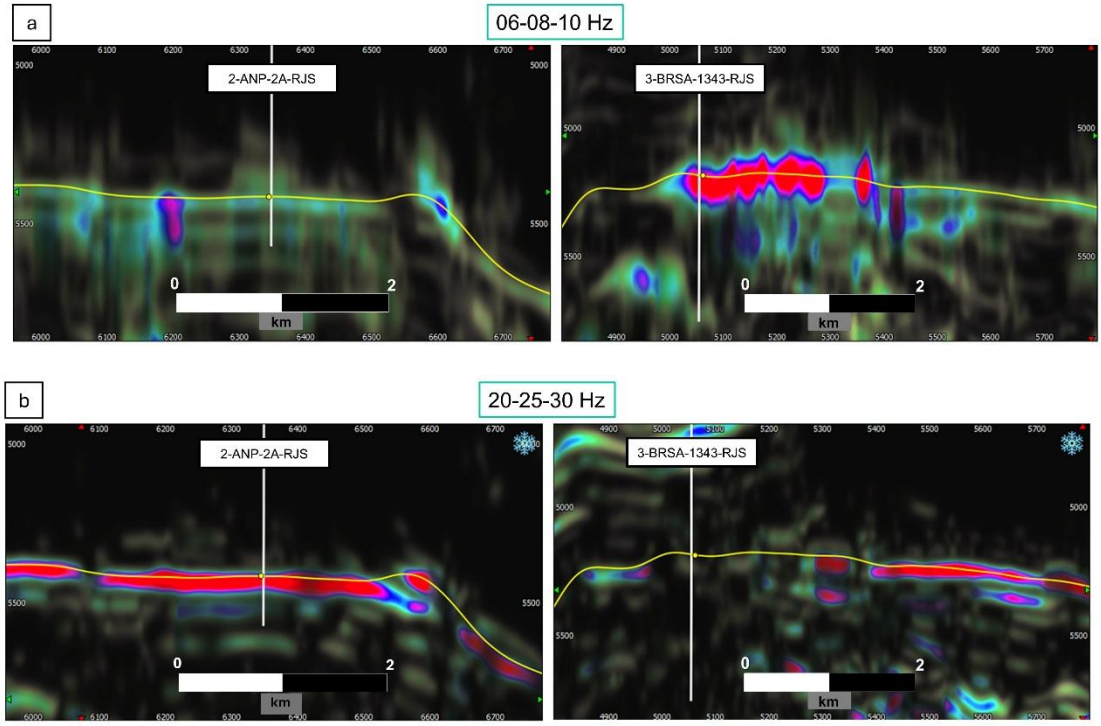

Figure 37. HSV blending of three frequency components at well locations 2-ANP-2A-RJS and 3-BRSA-1343-RJS, illustrating the contrast between (a) low- (6-8-10 Hz) and (b) high- (20-25-30 Hz) frequency responses. Interpretation of the base of salt is represented by the yellow horizon.

5.3 Comparison of attributes and display in horizon

Figure 38 now shows the same attributes than in figure 36 but mapped along the base of the salt horizon. The RMS amplitude map (7 smp vertical window) (Fig. 38 a) highlights a strong and extensive anomaly that cannot be attributed solely to the presence of diabase. The RGB blend (Fig. 38 b), using frequencies of 10, 20, and 30 Hz, introduces a marked heterogeneity compared with the RMS map. When viewed as a whole, within the structural contour polygon, several distinct regions can be identified: areas dominated by red tones, consistent with the occurrence of igneous rocks along this surface; areas dominated by blue or green tones, which may correspond to low-porosity reservoir entry points directly beneath the anhydrite; and darker, more chaotic zones, at the northern and southern extremes, corresponding to carbonate mounds.

The third map (Fig. 38 c) captures the anomalies observed in the previous seismic line, corresponding to the HSV blend using frequencies of 12, 14, and 16 Hz. The combination of these frequencies, where their magnitude is highest, appears as bright, saturated pink-red colours, while the rest of the map—where these frequencies have very low magnitude—appears largely homogeneous, in subdued greenish-grey tones. The position of the wells indicating the presence of igneous rocks intercalated between the reservoir top and the base of the salt shows good consistency with the anomalies on the map. However, the extent of these anomalies does not cover the entire area where diabase occurs, particularly in the central sector. This discrepancy can be attributed to several factors.

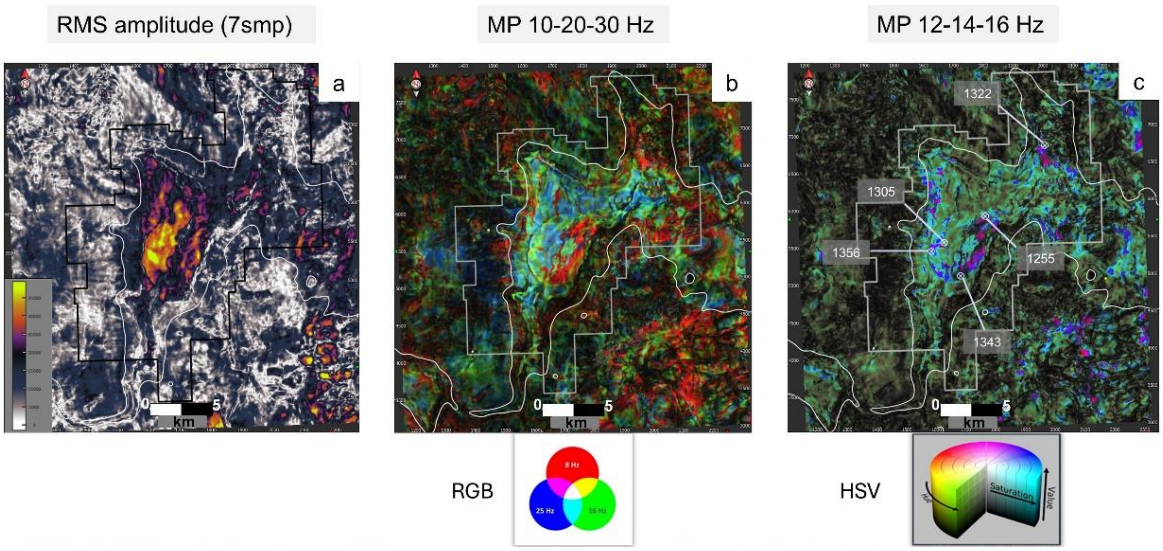

Figure 38. Comparison of base-of-salt maps derived from the previous attribute volumes.

The first factor is that part of the region where diabase occurs is better highlighted at lower frequencies (6–10 Hz). The second is that the spectral decomposition attribute is not windowed—that is, it represents only the voxel through which the mapped horizon passes—making the map highly sensitive to minor positional inaccuracies. The third factor, illustrated in Figure 39, is that the presence of diabase at the top of the reservoir does not always produce the same seismic signature. In some cases, it consists of two very strong and thick reflectors (Fig. 39 a), whereas in others, the amplitudes of the anhydrite–diabase–carbonate sequence do not overlap, resulting in distinct reflectors and, consequently, distinct frequency ranges on the spectrogram (Fig. 39 c).

At well 3-BRSA-1305-RJS, an igneous layer with a thickness of approximately 90 meters was recorded, whereas at well 3-BRSA-1255-RJS, the corresponding layer is about 43 meters thick. The difference in amplitude behaviour between these two wells may be due to the significant thickness of the igneous intrusion at well 3-BRSA-1305-RJS, which probably causes the amplitudes of the three lithologies not to completely overlap. Nevertheless, the spectrogram associated with this well shows a low-frequency anomaly corresponding to the base of the igneous interval.

A way to overcome this limitation and to represent the occurrence of igneous rocks within an interval—rather than only around a single horizon—is through the extraction of geobodies.

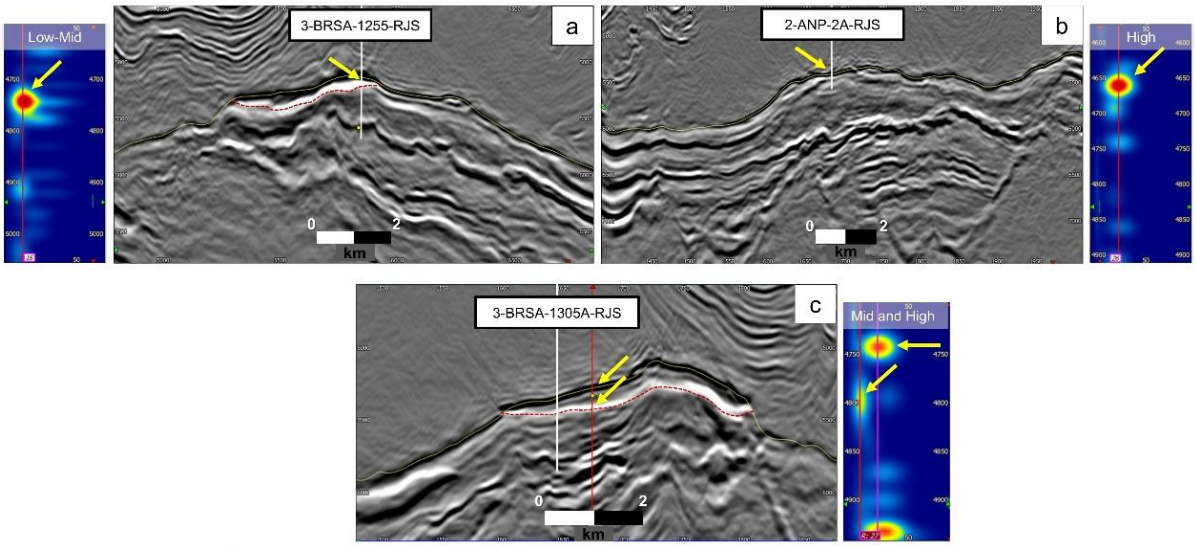

Figure 39. Seismic sections crossing key wells in the Mero Field, illustrating the typical seismic amplitude response and its associated frequency signature on the spectrogram: (a) when a diabase sill occurs at the top of the Barra Velha Formation, and (b) when it does not. Some limitations are observed at well 3-BRSA-1305A-RJS, where a thick diabase body is interbedded, but the seismic amplitude still produces distinct reflectors. This is further supported by the spectrogram, which clearly shows the separation between lithologies.

5.4 Geobody extraction

Upper Barra Velha

The geobody extraction was limited to the Mero reservoir area and constrained between two horizons from the horizon stack: one located slightly above the base of the salt, and another between the Intra-Alagoas unconformity and the base of the salt. The resulting geobody corresponds to a merge of volumes extracted from the low-frequency range (6, 8, and 10 Hz) and the mid-frequency range (12, 14, and 16 Hz). Figure 40 a shows the wells that contain igneous rocks at the top of the reservoir, whereas Figure 40 b displays those without, serving as a quality control for the extracted geobody. Overall, the result shows a good correspondence with what was expected from most wells.

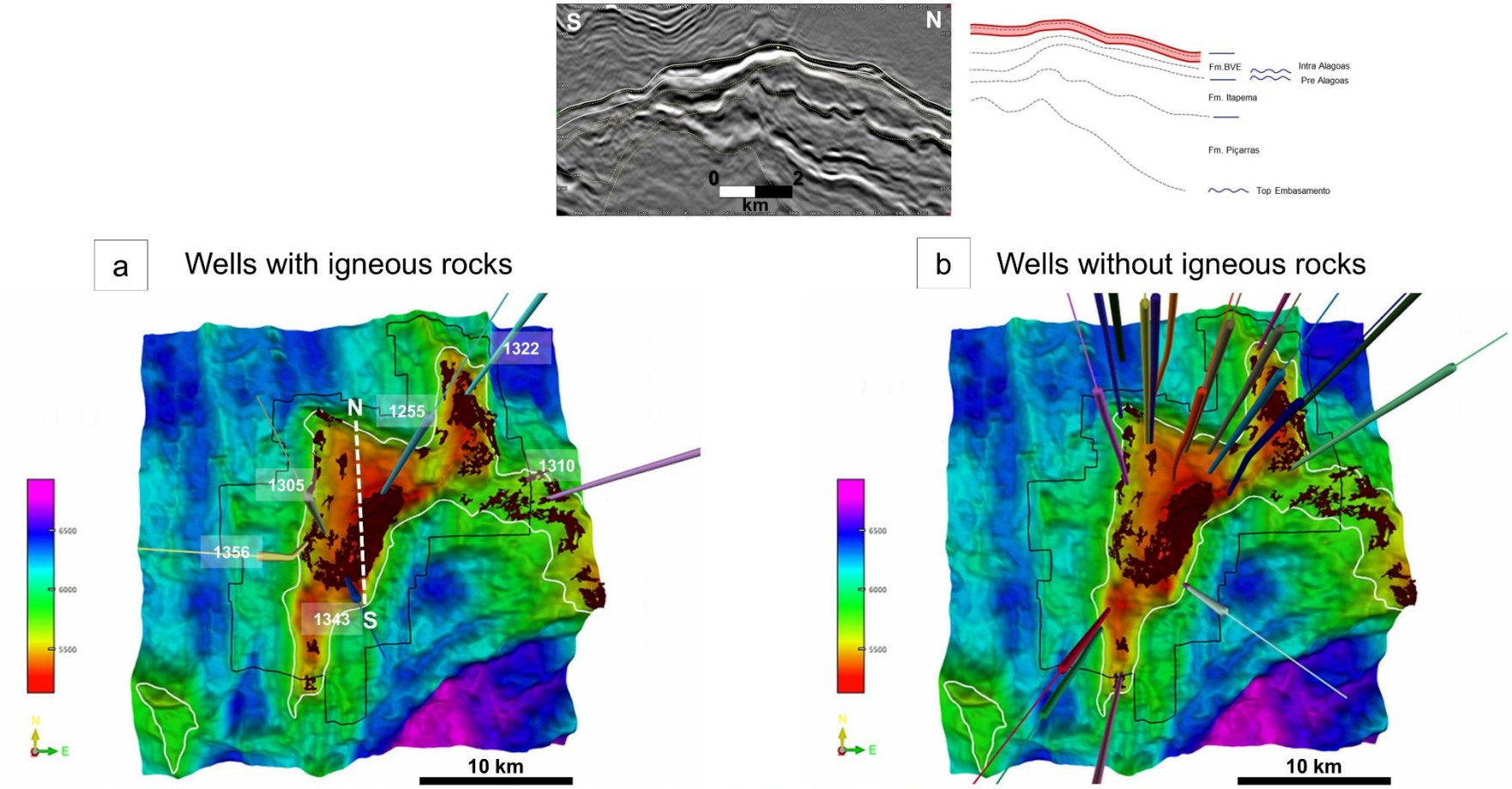

Figure 40. Results of the merged geobody, extracted from the low-frequency range (6, 8, and 10 Hz) and the mid-frequency range (12, 14, and 16 Hz), for the upper Barra Velha Formation. Displayed with wells reporting igneous rocks within this interval (a) and wells reporting no igneous rocks - or only bodies below seismic detection - (b).

Lower Barra Velha and Upper Itapema

Few igneous intrusions are known to occur within the lower Barra Velha and upper Itapema formations, but one of them is among the most prominent in the field and was confirmed by well 3-BRSA-1322-RJS, which drilled through it. Figure 41 a shows the result of the extraction limited to the Mero reservoir area, performed between the Intra-Alagoas and Pre-Alagoas unconformities. Figure 41 b presents the result of the extraction carried out for the upper part of the Itapema Formation, using an intermediate horizon from the horizon stack together with the Pre-Alagoas Unconformity.

The resulting geobody corresponds to a merge of volumes extracted from the low-frequency range (6, 8, and 10 Hz) and the mid-frequency range (12, 14, and 16 Hz); the latter was used to capture the extremities of the igneous body, which tend to thin out. Visualization in a 3D viewer (Fig. 41 c) reveals how the bodies—described as igneous sheets by Marins et al. (2025)—are constrained by the structural framework and associated faults.

Most of the geobody fragments distributed across the field are not associated with actual igneous bodies and can be considered as noise. This is particularly true for those located in the southern part of the field that were incorporated even though they are, in fact, related to the top of the Piçarras Formation. The proximity of the extraction horizon to this surface gives rise to this interference.

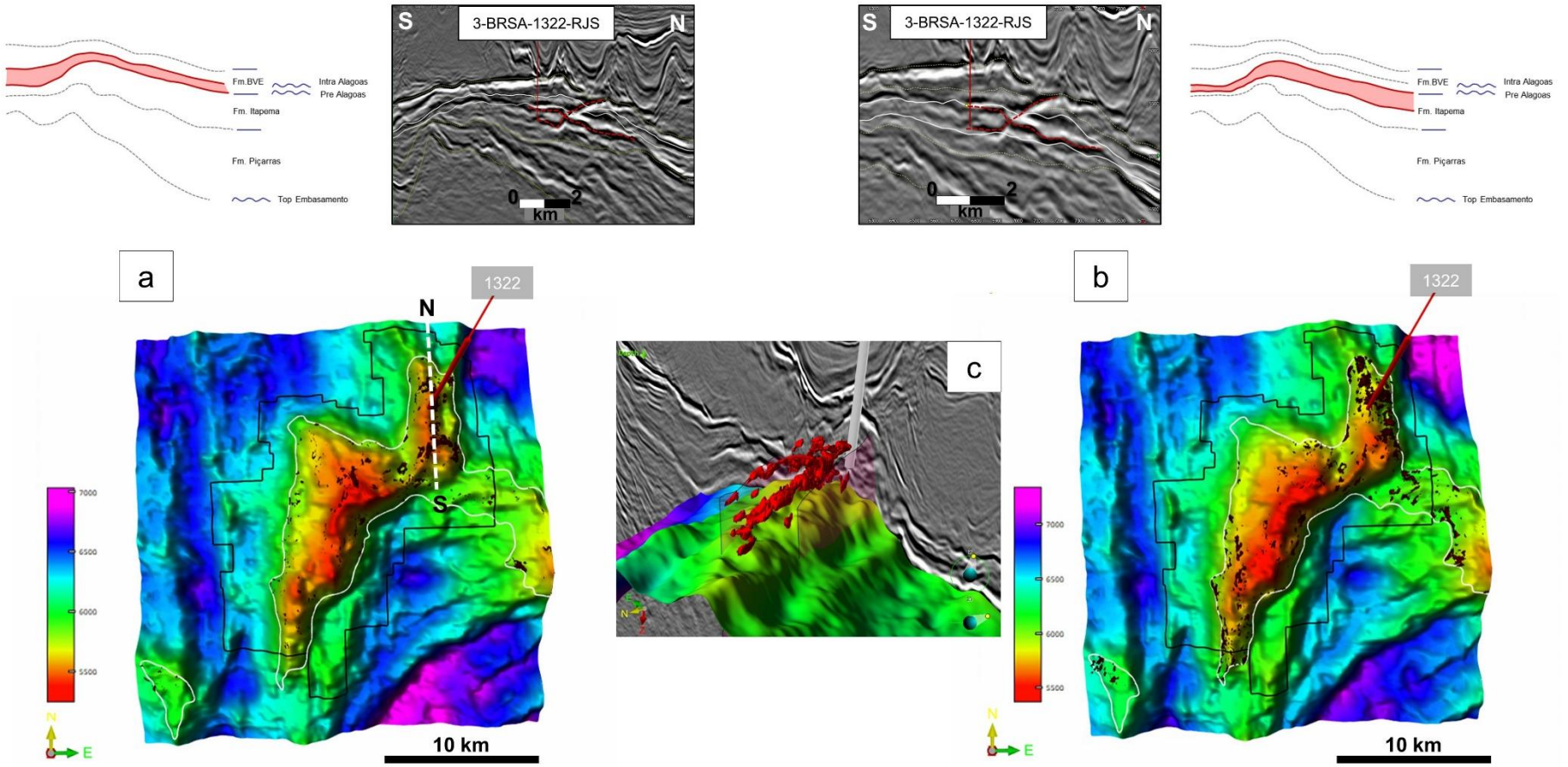

Figure 41. Results of the merged geobody, extracted from the low-frequency range (6, 8, and 10 Hz) and the mid-frequency range (12, 14, and 16 Hz), for the lower Barra Velha Formation (a) and the upper Itapema interval (b). 3D visualization of the geobody in well 3-BRSA-1322-RJS location (c).

Lower Itapema

As discussed at the beginning of this chapter, subaerial basaltic flows of Barremian-Aptian age are recognized at the base of the Itapema Formation. Immediately above, the main pre-salt source rock, the Jiquiá Shale, was deposited in the structural lows. The superposition of these two lithologies produces a very thick and bright negative reflector, followed by a strong positive one. This configuration can be used in spectral decomposition to approximate the occurrence of basaltic flows at the base of the Itapema Formation.

The geobody extraction was not limited to the Mero reservoir area, as these features mainly occur in the structural lows. It was constrained between the top of the Itapema Formation (Pre-Jiquiá Unconformity) and an intermediate horizon from the horizon stack within the formation. The geobody was extracted from the low-frequency range (6, 8, and 10 Hz).

Figure 42 shows a seismic line crossing the field in a north–south direction, illustrating the absence of the geobody in the southern part of the area, even though a structural low is present. According to the data, the amplitude contrast does not occur in this sector; therefore, the geobody extraction did not capture any feature there, as indicated by the yellow arrows.

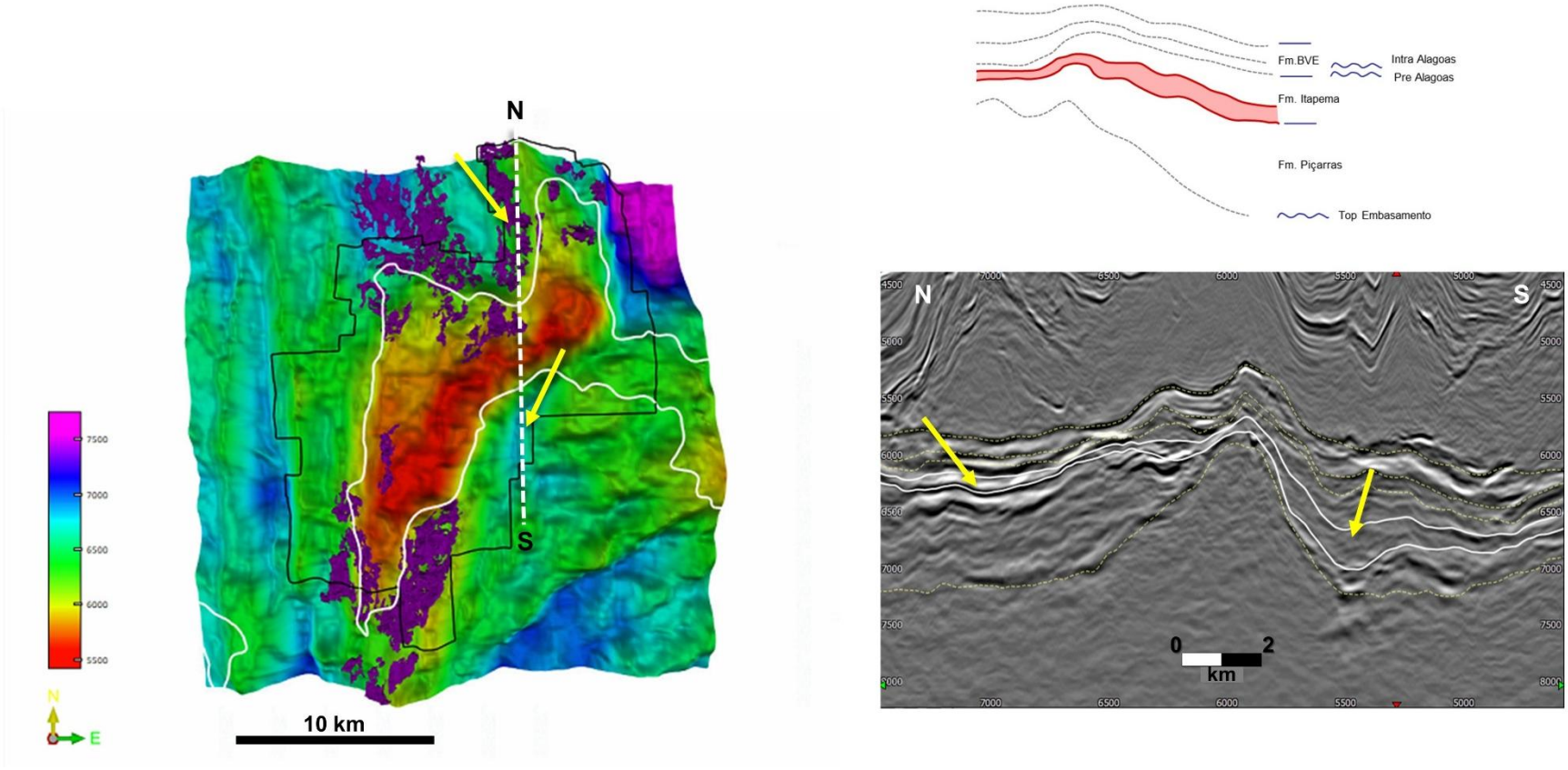

Figure 42. Result of the geobody extraction from the low-frequency range (6, 8, and 10 Hz), for the lower Itapema interval. Yellow arrows indicate the relationship between the extracted geobody and the seismic amplitude response within the interval of interest.

Upper and Lower Piçarras

For the Piçarras Formation, the extraction was also performed in two separate intervals. The first geobody is bounded at the top by a horizon from the horizon stack that lies slightly below the Top Piçarras, in order to minimize the inclusion of strong amplitudes related to the Itapema Formation. An intermediate horizon from the horizon stack was also used to constrain the extraction to the upper part of the Piçarras Formation.

Two geobodies were generated: one from the low-frequency range (6, 8 and 10 Hz) (fig. 43 a), aimed at capturing features interpreted as intrusive bodies, and another from the high-frequency range (20, 30 and 35 Hz) (Fig. 43 b), designed to extract features associated with subaerial basaltic flows largely recognized as lava-delta–type deposits. This interpretation is supported by the presence of a prominent volcanic edifice located upstream (Fig. 44).

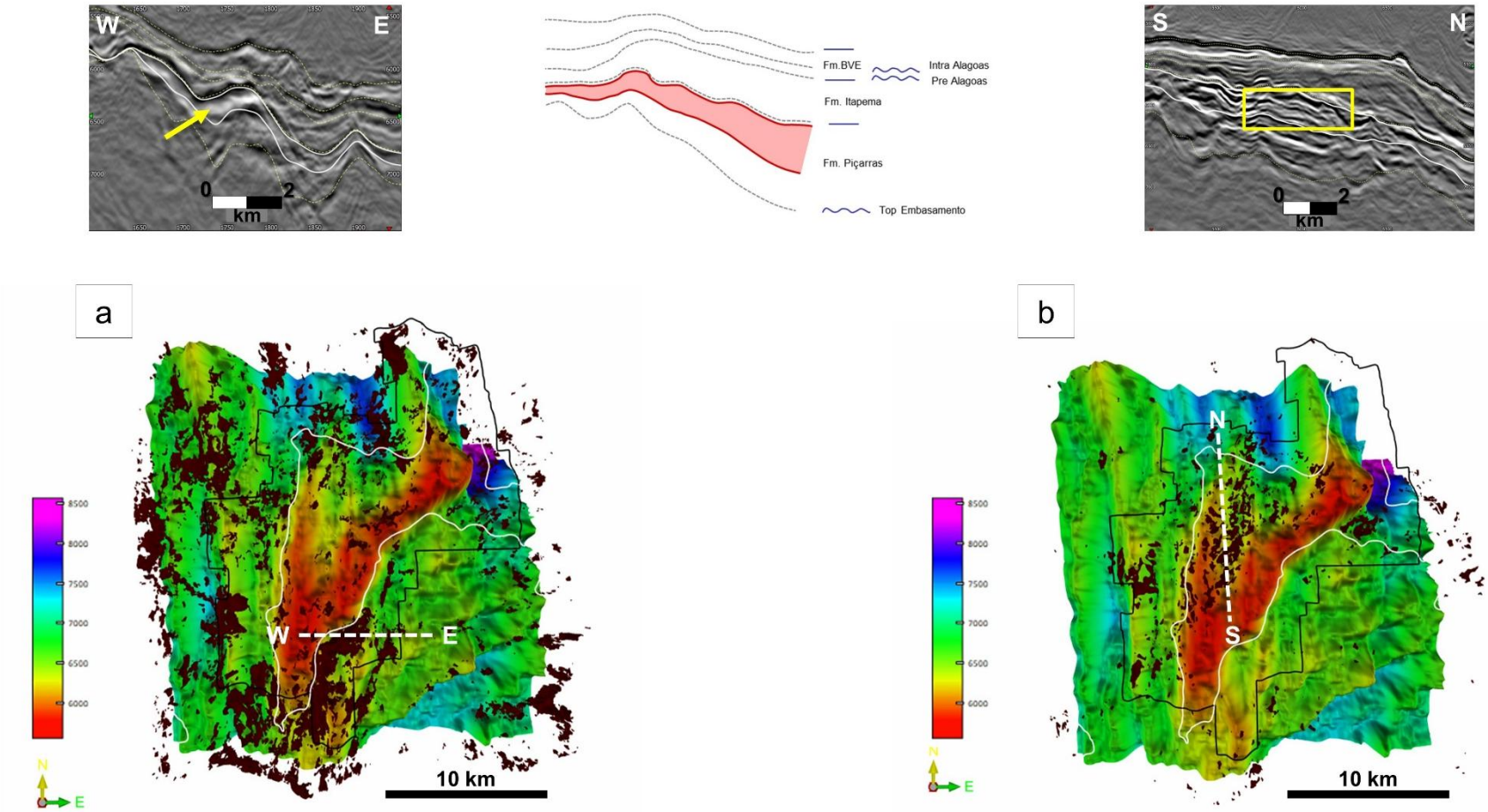

Figure 43. Result of the geobody extraction for the upper Piçarras interval, from (a) low-frequency range (6, 8 and 10 Hz) and (b) high-frequency range (25, 30 and 35 Hz).

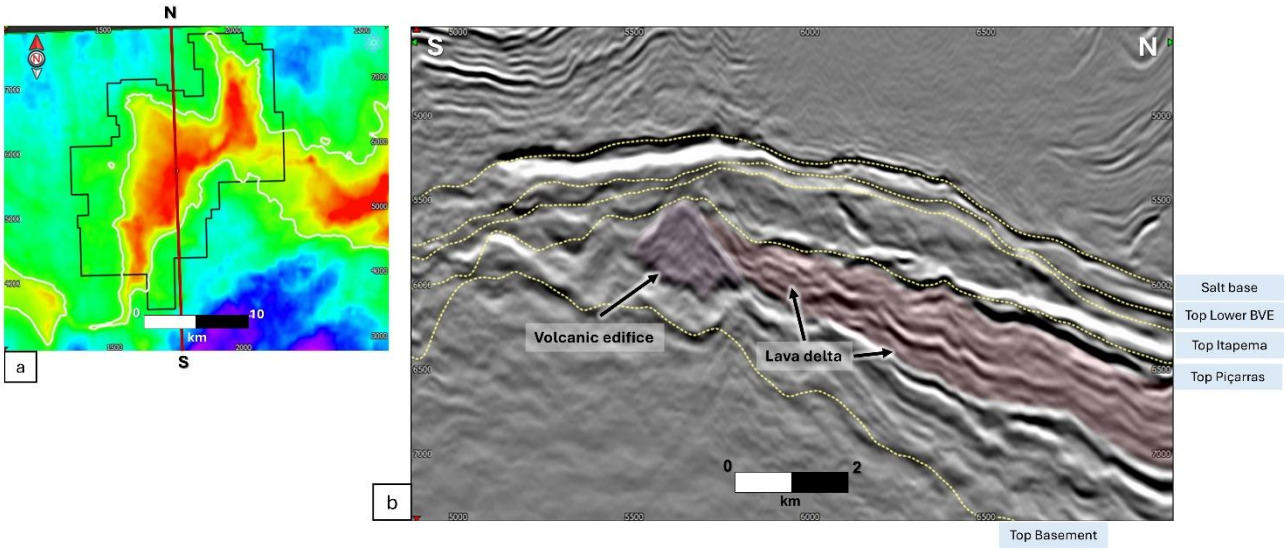

Figure 44. Location map (a) and seismic section (b) with interpretation of a volcanic edifice and the associated lava delta within the Piçarras Formation, inspired by Oliveira et al., 2024.

The same frequency ranges were used for the extraction within the lower interval. The horizon used as the lower boundary for the upper Piçarras geobody was employed this time as the upper boundary, while another horizon from the horizon stack—located slightly above the top of the basement—served to define the base of the geobody. This approach slightly improved the result by preventing low-frequency features from being truncated by the interpreted horizon. The geobody shown in Figure 45 a displays a strong structural control, as most of its extent aligns with the main basement fault trends.

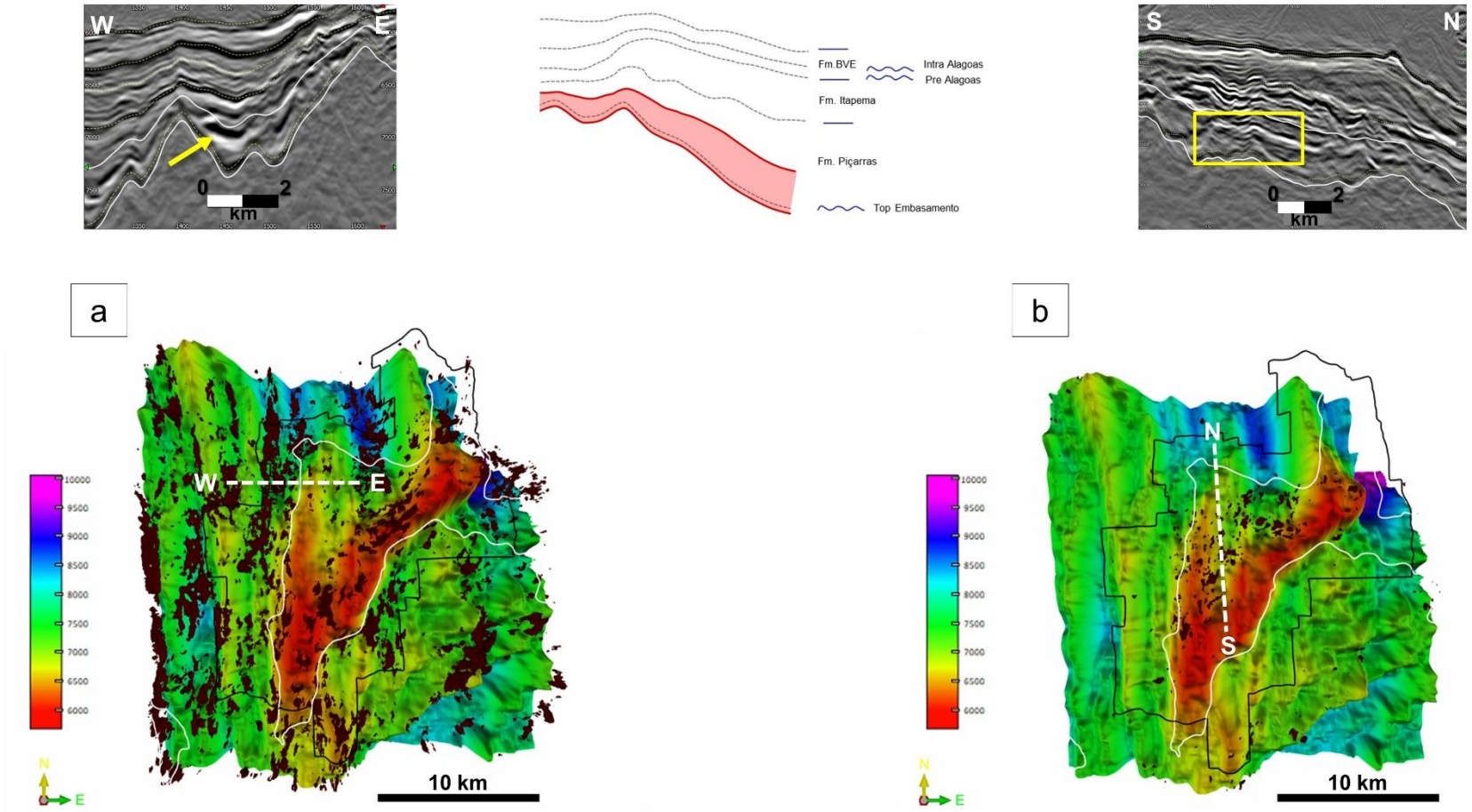

Figure 45. Result of the geobody extraction for the lower Piçarras interval, from (a) low-frequency range (6, 8 and 10 Hz) and (b) high-frequency range (25, 30 and 35 Hz).

5.5 Comparison with Other Work

The geobody extracted at the top of the Barra Velha Formation is the one for which the largest number of wells was available to validate the result. In addition, previous studies provide a useful basis for comparison. Penna et al. (2019) used seismic inversion to produce probabilistic occurrence maps of intrusive rocks within the upper Barra Velha Formation, proposing both optimistic and pessimistic scenarios (Fig. 46). Our results are broadly consistent with theirs, although some differences are observed. These discrepancies can be attributed to the inherent limitations of each method.

Overall, the workflow proposed in this study proves to be useful in an exploratory context—particularly when well data required for seismic inversion are still insufficient for the area under investigation—but also as an alternative approach for obtaining a preliminary assessment in a faster and more efficient manner.

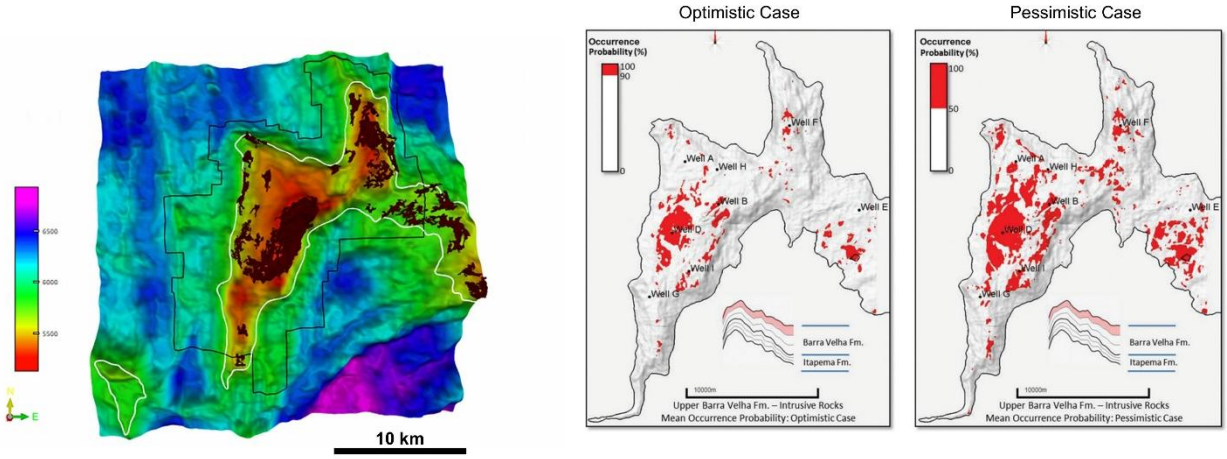

Figure 46. Comparison of the extracted geobody in the upper Barra Velha interval, representing the occurrence of diabase sills, with the occurrence probability maps (optimistic and pessimistic cases) presented by Penna et al., 2019.

6. Conclusions

In summary, this study employed a high-resolution spectral decomposition technique to capture the seismic signatures of the main magmatic features within the Mero Field, with the aim of detecting and delineating them within the seismic data. The initial focus was on differentiating between carbonates, the base of the anhydrite, and diabase bodies. The applied method proved effective in distinguishing areas where this group of lithologies occurs from those where it does not.

Overall, the Matching Pursuit decomposition can be regarded as an attribute sensitive to reflector thickness. This property can be effectively exploited in pre-salt environments, where overlapping amplitude responses from rocks with high acoustic impedance may generate apparent reflector-thickness anomalies. Concordant diabase sills at the base of the salt typically exhibit low- to medium-frequency responses (approximately 6–16 Hz), whereas areas without diabase show higher-frequency signatures (20–35 Hz). Intrusions exceeding the seismic resolution (~75 m) can be recognized by their strong acoustic impedance, discordance with stratigraphy, and low- to medium-frequency spectral responses that capture their edges. The combination of shale layers overlying lava flows at the base of the Itapema Formation is marked by low-frequency signatures. Within the Piçarras Formation, intrusive bodies tend to display low-frequency characteristics, while lava flows are characterized mainly by high-frequency responses.

A complementary aspect of the study involved evaluating the most suitable display method for frequential attribute visualization. Both RGB and HSV colour models were tested. Although the HSV model is conventionally used for blending attributes of different natures, it proved effective in this case for emphasizing features corresponding to a specific narrow frequency range when applied in conjunction with the Matching Pursuit decomposition method.

To spatially represent the occurrence of igneous rocks within the investigated intervals, geobody extraction proved to be the most suitable approach. The process relied on blended frequency volumes, from which specific combinations of spectral attributes were selected through cross plot analysis to define classes corresponding to the desired geological targets. These classes were then extracted

from the seismic volumes to generate three-dimensional geobodies. However, the vertical extent of these geobodies must be carefully constrained to avoid misleading interpretations. The construction of an isoproportional geomodel—based on interpreted horizons and enabling the generation of multiple intermediate surfaces—was particularly useful for defining consistent extraction intervals.

While the methodology just described improved the results, the resulting geobody maps should be interpreted as trend representations rather than definitive lithological boundaries. They still contain residual noise, and the resolution of the mapped intervals influences whether certain features are over- or underrepresented. Therefore, their interpretation should always take these intrinsic limitations into account.

Post-stack seismic conditioning represented a crucial step for noise attenuation and frequency broadening within the pre-salt section. These enhancements significantly improved the performance of the Matching Pursuit decomposition, particularly by increasing the definition and continuity of medium- and high-frequency features. This step was essential, as Matching Pursuit, while providing high spectral resolution, is inherently very sensitive to noise.

To further develop the workflow proposed in this study, we first suggest that future work should include a multi-attribute analysis combining Matching Pursuit spectral decomposition with additional structural and textural attributes, among others. We also recommend testing the workflow on a seismic volume to which Relative Acoustic Impedance has been applied. Secondly, further efforts should focus on refining the discrimination between intrusive and extrusive magmatic events. Finally, to advance reservoir characterization, future studies should investigate the impact of these magmatic events on reservoir quality—particularly their effects on porosity, permeability, and CO_2 content—by integrating additional rock and petrophysical data.

References

Anderson A. Pinheiro Chagas, Carlos César de Araújo, & Luiz Alberto Santos. (2024). *As grandes descobertas do Pré-sal no Atlântico Sul*. Petrobras.

Baptista, R. J., Ferraz, A. E., Sombra, C., dos Santos Neto, E. V., Plawiak, R., Lops Silva, C. L., Ferrari, A. L., Kumar, N., & Gamboa, L. A. P. (2023). The presalt Santos Basin, a super basin of the twenty-first century. *AAPG Bulletin*, *107*(8), 1369–1389. https://doi.org/10.1306/04042322048

Barnes, A. E. (2016). Handbook of Poststack Seismic Attributes. In *Handbook of Poststack Seismic Attributes*. Society of Exploration Geophysicists. https://doi.org/10.1190/1.9781560803324

Beck, A., & Teboulle, M. (2009). A fast iterative shrinkage-thresholding algorithm for linear inverse problems. *SIAM Journal on Imaging Sciences*, *2*(1), 183–202. https://doi.org/10.1137/080716542

Brito, J. P. S., Santos, R. v., Gonçalves, G. O., Barbosa, P. F., Souza Cruz, C. E., Ushirobira, C. A., Souza, V. S., Richter, F., & Abreu, C. J. (2024). U-Pb dating of Barra Velha carbonates reveals the influence of Santos Basin sedimentary and tectonothermal history on pre-salt carbonate ages. *Marine and Petroleum Geology*, *168*. https://doi.org/10.1016/j.marpetgeo.2024.107035

Carminatti, M., Dias, J. L., & Wolff, B. (2009). From Turbidites to Carbonates: Breaking Paradigms in Deep Waters. *OTC 20124*.

Carvalho, R., Gonzalez, M., & Lupinacci, W. (2022). Characterizing seismic facies in a carbonate reservoir, using machine learning offshore Brazil. *G&G TECHNOLOGY*.

Chafetz, H., Barth, J., Cook, M., Guo, X., & Zhou, J. (2018). Origins of carbonate spherulites: Implications for Brazilian Aptian pre-salt reservoir. *Sedimentary Geology*, *365*, 21–33. https://doi.org/10.1016/j.sedgeo.2017.12.024

Chang, H. K., Kowsmann, R. O., Figueiredo, A. M. F., & Bender, A. A. (1992). Tectonics and stratigraphy of the East Brazil Rift system: an overview. *Tectonophysics*, *213*, 97–138.

Correia, U. M. da C., Honório, B. C. Z., Kuroda, M. C., Melani, L. H., & Vidal, A. C. (2019). Geometric characterization of igneous intrusions: 3-D seismic insights from the Campos Basin, SE Brazil. *Marine and Petroleum Geology*, *102*, 725–739. https://doi.org/10.1016/j.marpetgeo.2019.01.022

de Freitas, V. A., Vital, J. C. dos S., Rodrigues, B. R., & Rodrigues, R. (2022). Source rock potential, main depocenters, and CO2 occurrence in the pre-salt section of Santos Basin, southeast Brazil. *Journal of South American Earth Sciences*, *115*. https://doi.org/10.1016/j.jsames.2022.103760

de Mahiques, M. M., Schattner, U., Riccomini, C., de Assis Janasi, V., Lobo, F. J., Vasconcelos, P., Thiede, D. S., Ramos, R. B., & Felicio dos Santos, R. (2023). Submarine basalt xenoliths confirm the occurrence of post-rift volcanism in the Southern Santos Basin, SW Atlantic. *Journal of South American Earth Sciences*, *132*. https://doi.org/10.1016/j.jsames.2023.104661

Dorobek, S., Piccoli, L., Coffey, B., & Adams, A. (2012). Carbonate Rock-Forming Processes in the Pre-salt “Sag” Successions of Campos Basin, Offshore Brazil: Evidence for Seasonal, Dominantly Abiotic Carbonate Precipitation, Substrate Controls, and Broader Geologic Implications. *AAPG Search and Discovery Article #90153©2012*, 3–8.

Eide, C. H., Schofield, N., Lecomte, I., Buckley, S. J., & Howell, J. A. (2018). Seismic interpretation of sill complexes in sedimentary basins: implications for the sub-sill imaging problem. *Journal of the Geological Society*, *Vol. 174*, 23–40. https://doi.org/10.6084/m9.figshare.5607160

Eustáquio Moreira Lima Petróleo Brasileiro, B. S., Costa de Oliveira Petróleo Brasileiro, L. S., Farias Petróleo Brasileiro, F. S., & Fernando De Ros, L. (2022). *The role of magmatism in the deposition, diagenesis, and hydrothermal alteration of Aptian Pre-Salt reservoirs from Brazilian offshore basins*. https://www.researchgate.net/publication/361250501

Farias, F., Szatmari, P., Bahniuk, A., & França, A. B. (2019). Evaporitic carbonates in the pre-salt of Santos Basin – Genesis and tectonic implications. *Marine and Petroleum Geology*, *105*, 251–272. https://doi.org/10.1016/j.marpetgeo.2019.04.020

Ferreira, L. C., Stanton, N., Gordon, A. C., & Schmitt, R. (2023). The Magmatic Rifting of Santos Basin: Aeromagnetic Mapping of Dykes, Terranes and Marginal Structures and the Interplay Between Tectonism and Volcanism. *Tectonics*, *42*(4). https://doi.org/10.1029/2022TC007560

Fodor, R. v, Mckee, E. H., & Asmus, H. E. (1983). K-At AGES AND THE OPENING OF THE SOUTH ATLANTIC OCEAN: BASALTIC ROCK FROM THE BRAZILIAN MARGIN. *Marine Geology*, *54*, 1–8.

Fornero, S. A., Marins, G. M., Lobo, J. T., Freire, A. F. M., & Lima, E. F. de. (2019). Characterization of subaerial volcanic facies using acoustic image logs: Lithofacies and log-facies of a lava-flow deposit in the Brazilian pre-salt, deepwater of Santos Basin. *Marine and Petroleum Geology*, *99*, 156–174. https://doi.org/10.1016/j.marpetgeo.2018.09.029

Gamboa, L., Ferraz, A., Baptista, R., & Santos Neto, E. v. (2019). Geotectonic controls on CO2 formation and distribution processes in the Brazilian pre-salt basins. *Geosciences*, *9*(252), 1–14. https://doi.org/10.3390/geosciences9060252

Gomes, J. P., Bunevich, R. B., Tedeschi, L. R., Tucker, M. E., & Whitaker, F. F. (2020). Facies classification and patterns of lacustrine carbonate deposition of the Barra Velha Formation, Santos Basin, Brazilian Pre-salt. *Marine and Petroleum Geology*, *113*. https://doi.org/10.1016/j.marpetgeo.2019.104176

Gomes, P. O. (2008). The Outer High of the Santos Basin, Southern São Paulo Plateau, Brazil: Pre-Salt Exploration Outbreak, Paleogeographic Setting, and Evolution of the Syn-Rift Structures. *Search and Discovery Article #10193 (2009)*. https://www.researchgate.net/publication/242701965

Gomes, P. O., Parry, J., & Martins, W. (2002). Hydrocarbon Habitat of Volcanic Rifted Passive Margins. *AAPG Search and Discovery Article #90022*.

Gordon, A. C., Mohriak, W. U., Stanton, N., & Santos, A. C. (2023). Magmatic cycles in Santos Basin (S.E. Brazil): Tectonic control in the temporal-spatial distribution and geophysical signature. *Journal of South American Earth Sciences*, *121*. https://doi.org/10.1016/j.jsames.2022.104111

Gordon, A. C., Santos, A. C., Caitano, G. R., Stanton, N., & Mohriak, W. U. (2023). Magmatic cycles in Santos Basin (S.E. Brazil): Geochemical characterization and magmatic sources. *Journal of South American Earth Sciences*, *126*. https://doi.org/10.1016/j.jsames.2023.104323

Goupillaud Pierre L. (1961). An approach to inverse filtering of near-surface layer effects from seismic records. *GEOPHYSICS*, *Vol. XXVI*(NO. 6), 754–760.

He, W., Wang, H., Su, J., Wang, W., Zhao, J., Zuo, G., Wang, T., Yang, L., Ren, K., Wang, C., Zhao, J., Guo, Y., Zhang, Y., & Sun, J. (2025). Magma evolution during the post-rift phase of the Santos Basin, Brazil: petrogenesis and geochemistry of ~126–121 ma basalts and diabases. *Frontiers in Earth Science*, *12*. https://doi.org/10.3389/feart.2024.1497913

Hudec, M. R., & Jackson, M. P. A. (2007). Terra infirma: Understanding salt tectonics. *Earth-Science Reviews*, *82*(1–2), 1–28. https://doi.org/10.1016/j.earscirev.2007.01.001

Hunt, D., Virmond Juk, K., Troth, I., Guillien, A., Luna, C., Masiero, I., Matos, G., & Jetlund Hansen, L. (2022). The Bacalhau field: New Insights into Lacustrine Carbonate Platform Development, Santos Basin, Brazil. *3rd EAGE Conference on Pre Salt Reservoirs*. https://doi.org/10.3997/2214-4609.202288028

Jesus, C., Lupinacci, W. M., Takayama, P., Almeida, J., & Ariza Ferreira, D. J. (2020). An approach to reduce exploration risk using spectral decomposition, prestack inversion, and seismic facies classification. *AAPG Bulletin*, *104*(5), 1075–1090. https://doi.org/10.1306/10161918065

Louback, V. S., de Castro Valente, S., de Almeida, C. N., Ross, J., & Borghi, L. (2021). Petrogenesis and geodynamics of Eocene alkaline intrusions in the pre-salt sedimentary sequence of Santos Basin, Brazil. *Lithos*, *400–401*. https://doi.org/10.1016/j.lithos.2021.106400

Louback, V. S., de Castro Valente, S., Neysi De Almeida, C., Ross, J., Borghi, L., De, S., & Valente, C. (2023). *Aptian flood basalts in Bacalhau field: petrogenesis and geodynamics of post-rift tholeiites in the Pre-Salt of Santos Basin, Brazil*.

Maas, M. V. R., Bedle, H., & de Matos, M. C. (2023). Seismic identification of carbonate reservoir sweet spots using unsupervised machine learning: A case study from Brazil deep water Aptian pre-salt data. *Marine and Petroleum Geology*, *151*. https://doi.org/10.1016/j.marpetgeo.2023.106199

Madrinovella, I., & Pranowo, W. (2022). THE DIRECT-INVERSION DECONVOLUTION AND ITS APPLICATION IN SEISMIC DATA. *JGE (Jurnal Geofisika Eksplorasi)*, *8*(1), 31–43. https://doi.org/10.23960/jge.v8i1.187

Magee, C., Pichel, L. M., Madden-Nadeau, A. L., Jackson, C. A. L., & Mohriak, W. (2021). Salt–magma interactions influence intrusion distribution and salt tectonics in the Santos Basin, offshore Brazil. *Basin Research*, *33*(3), 1820–1843. https://doi.org/10.1111/bre.12537

Mallat, S. G., & Zhang, Z. (1993). Matching Pursuits With Time-Frequency Dictionaries. *IEEE TRANSACTIONS ON SIGNAL PROCESSING*, *41*(12), 3397–3415.

Marins, G. M., Lima, N. M., Oliveira, L. C., Gangá, A. O., Monnerat de Oliveira, C. M., Rocha, Y. M., Abrantes, F., Rossetti, L. M. M., Costa, J., Millet, J. M., Fornero, S. A., & Iwata, S. A. (2025). The deep roots and emplacement of Santonian intrusions in the Pre-Salt reservoirs of the Mero Field, Santos Basin, Brazil. *Marine and Petroleum Geology*, *174*. https://doi.org/10.1016/j.marpetgeo.2025.107291

Martinho Souto Muniz Da Cruz, N. (2023). *MAPEAMENTO DE ELEMENTOS DEPOSICIONAIS E DIAGENÉTICOS, ATRAVÉS DE ESTUDOS PETROGEOFÍSICOS E DE IDENTIFICAÇÃO E ANÁLISE DE FEIÇÕES SÍSMICAS NA FORMAÇÃO BARRA VELHA DA BACIA DE SANTOS: IMPACTO NOS MODELOS DE RESERVATÓRIO E NAS ESTRATÉGIAS DE DESENVOLVIMENTO DE CAMPOS DO PRÉ-SAL*.

Milani, E. J., & Zalán, P. V. (1999). An outline of the geology and petroleum systems of the Paleozoic interior basins of South America. *Episodes*, *Vol. 22*(3).

Mitchell, R. N., Thissen, C. J., Evans, D. A. D., Slotznick, S. P., Coccioni, R., Yamazaki, T., & Kirschvink, J. L. (2021). A Late Cretaceous true polar wander oscillation. *Nature Communications*, *12*(1). https://doi.org/10.1038/s41467-021-23803-8

Mohriak, W. U. (2001). *South Atlantic Ocean Salt tectonics, volcanic centers, fracture zones and their relationship with the origin and evolution of the South Atlantic Ocean: geophysical evidence in the Brazilian and West African margins*.

Mohriak, W. U., de Almeida, J. C. H., & Gordon, A. C. (2021). South Atlantic Ocean: postbreakup configuration and Cenozoic magmatism. In *Meso-Cenozoic Brazilian Offshore Magmatism: Geochemistry, Petrology, and Tectonics* (pp. 1–45). Elsevier. https://doi.org/10.1016/B978-0-12-823988-9.00007-1

Mohriak, W. U., Gordon, A., & Mello, M. R. (2022). Chapter 11: Origin and Petroleum System of the Cabo Frio High Between the Santos and Campos Basins: Reviewed Integration of Structural and Paleogeographic Reconstruction with the Oil and Gas Systems. In *Memoir 124: The Supergiant Lower Cretaceous Pre-Salt Petroleum Systems of the Santos Basin, Brazil* (pp. 273–324). AAPG. https://doi.org/10.1306/13722323msb.11.1853

Mohriak, W. U., Szatmari, P., & Anjos, S. (2012). Salt: Geology and tectonics of selected Brazilian basins in their global context. *Geological Society Special Publication*, *363*(1), 131–158. https://doi.org/10.1144/SP363.7

Mohriak, W. U., Zélia, A., & de Barros, N. (1990). NOVAS EVIDÊNCIAS DE TECTONISMO CENOZÓICO NA REGIÃO SUDESTE DO BRASIL: O GRÁBEN DE BARRA DE,SÃO JOÃO NA PLATAFORMA DE CABO FRIO, RJ. *Revista Brasileira de Geociências*.

Moreira Pinheiro, J. L., Esteves, C. A., Rodrigues Gonçalves, J. J., & Vasconcelos Severiano, C. (2006). Magmatismo, sedimentação e estratigrafia de

porção norte da Bacia Santos. *B. Geoci. Petrobras*, *v. 14*, 161–170. https://www.researchgate.net/publication/303784114

Moreira Pinheiro, J. L., Madeira, C. V., Gil, J. A., Antonio, M., & Machado, P. (2007). Bacia de Santos. *B. Geoci. Petrobras*, *v. 15*(n. 2), 531–549.

Oliveira, L. C. de, Penna, R. M., Rancan, C. C., Carmo, I. de O., & Marins, G. M. (2024). Seismic interpretation of the Mero Field igneous rocks and its implications for pre- and post-salt CO2 generation – Santos Basin, offshore Brazil. *Marine and Petroleum Geology*, *163*. https://doi.org/10.1016/j.marpetgeo.2024.106775

Oliveira, L. C. de, & Rancan, C. C. (2019). Sill emplacement mechanisms and their relationship with the Pre-Salt stratigraphic framework of the Libra Area (Santos Basin, Brazil). *LASI 6 Conference*, 83–84. https://www.researchgate.net/publication/337683465

Oreiro, S. G., Cupertino, J. A., Szatmari, P., & Filho, A. T. (2008). Influence of pre-salt alignments in post-Aptian magmatism in the Cabo Frio High and its surroundings, Santos and Campos basins, SE Brazil: An example of non-plume-related magmatism. *Journal of South American Earth Sciences*, *25*(1), 116–131. https://doi.org/10.1016/j.jsames.2007.08.006

Penna, R., Araújo, S., Geisslinger, A., Sansonowski, R., Oliveira, L., Rosseto, J., & Matos, M. (2019). Carbonate and igneous rock characterization through reprocessing, FWI imaging, and elastic inversion of a legacy seismic data set in Brazilian presalt province. *Leading Edge*, *38*(1), 11–19. https://doi.org/10.1190/tle38010011.1

Penna, R., Costa de Oliveira, L., & Souza Rodrigues, L. (2024). Seismic quantitative interpretation of diagenetic processes: A study in Brazilian pre-salt carbonate reservoirs. *Marine and Petroleum Geology*, *170*. https://doi.org/10.1016/j.marpetgeo.2024.107134

Penna, R., & Moreira Lupinacci, W. (2021). 3D modelling of flow units and petrophysical properties in brazilian presalt carbonate. *Marine and Petroleum Geology*, *124*. https://doi.org/10.1016/j.marpetgeo.2020.104829

Petersohn, E., Morelatto, R., Batista, C. M. A., & Vital, J. C. S. (2021). Chapter 13: The Giant Mero Oil Field: Geological and Petrophysical Settings of One of the Largest Pre-Salt Fields of the Santos Basin, Southern Brazil. In *Memoir 124: The Supergiant Lower Cretaceous Pre-Salt Petroleum Systems of the Santos Basin, Brazil* (pp. 351–374). AAPG. https://doi.org/10.1306/13722325msb.13.1853

Pongwapee, S., Won-In, K., & Morley, C. K. (2020). Synrift magmatism in a Cenozoic rift basin, from 3D seismic data, Wichianburi Sub-Basin, Phetchabun Basin, Thailand: Part 1. Distribution and timing of intrusions and forced folds. *Journal of the Geological Society*, *177*(1), 189–210. https://doi.org/10.1144/jgs2019-046

Rancan, C. C., Oliveira, L. C. de, Carmo, I. de O., Marins, G. M., Pessoa, V. C. de O., Andrade, H. de, Penatti, A. P. R., Borges, T. A., Silva, R. C. B. da, Carlotto, M. A., Bassetto, M., & Zanatta, A. S. (2018). ROCHAS ÍGNEAS DO BLOCO DE LIBRA, BACIA DE SANTOS. *49º Congresso Brasileiro de Geologia*.

Rancan, C. C., Oliveira, L. C. de, Pessoa, V. C. de O., Andrade, H. de, Penatti, A. P. R., Borges, T. A., Silva, R. C. B. da, Carlotto, M. A., Bassetto, M., Sartorato, A. C. L., Mizuno, T. A., & Oliveira, M. J. R. (2018). ASPECTOS GEOLÓGICOS DO CAMPO DE MERO, BACIA DE SANTOS. *49º Congresso Brasileiro de Geologia*.

Ren, K., Lages de Oliveira, M. J., Costa de Oliveira, L., & Rancan, C. C. (2019). Metamorphism of pre-salt limestones produced by Santonian-Campanian alkaline sills in the Libra Block, Santos Basin. *LASI 6 Conference*, 131–132. https://www.researchgate.net/publication/358478896

Ren, K., Zhao, J., Liu, Q., & Zhao, J. (2020). Hydrocarbons in igneous rock of Brazil: A review. *Petroleum Research*, *5*. https://doi.org/10.1016/j.ptlrs.2020.06.001

Rigoti, C. A. (2015). *Evolução tectônica da Bacia de Santos com ênfase na geometria crustal: Interpretação integrada de dados de sísmica de reflexão e refração, gravimetria e magnetometria*.

Saller, A., Rushton, S., Buambua, L., Inman, K., McNeil, R., & Dickson, J. A. D. T. (2016). Presalt stratigraphy and depositional systems in the Kwanza Basin, offshore Angola. *AAPG Bulletin*, *100*(7), 1135–1164. https://doi.org/10.1306/02111615216

Sartorato, A. C. L., Tonietto, S. N., & Pereira, E. (2020). Silicification and dissolution features in the brazilian Pre-salt Barra Velha formation: impacts in the reservoir quality and insights for 3D geological modeling. *Rio Oil and Gas Expo and Conference*, *20*(2020), 68–69. https://doi.org/10.48072/2525-7579.rog.2020.068

Satinder Chopra, & Kurt J. Marfurt. (2024). *Essentials of Seismic Attributes and Impedance Inversion* (U. bin Waheed & T. J. Moser, Eds.). Society of Exploration Geophysicists.

Schattner, U., & Michaelovitch de Mahiques, M. (2020). Post-rift regional volcanism in southern Santos Basin and the uplift of the adjacent South American coastal range. *Journal of South American Earth Sciences*, *104*. https://doi.org/10.1016/j.jsames.2020.102855

Schlanger, S. O., & Jenkyns, H. C. (1976). Cretaceous Oceanic Anoxic Events: Causes and consequences. *Geologie En Mijnbouw*. https://www.researchgate.net/publication/27710997

Schofield, N., Holford, S., Millett, J., Brown, D., Jolley, D., Muirhead, D., Grove, C., Magee, C., Murray, J., Jackson, C., & Stevenson, C. (2015). *Regional Magma Plumbing and emplacement mechanisms of the Faroe-Shetland Sill Complex: 2 Implications for magma transport and petroleum systems within sedimentary basins 3 4*.

Sun, S., Castagna, J. P., & Siegfried, R. W. (2002). Examples of wavelet transform time-frequency analysis in direct hydrocarbon detection. *72nd Annual International Meeting, SEG, Expanded Abstracts, 457–460*. http://onepetro.org/SEGAM/proceedings-pdf/SEG02/SEG02/SEG-2002-0457/1880240/seg-2002-0457.pdf/1

Svensen, H., Planke, S., Malthe-Sørenssen, A., Jamtveit, B., Myklebust, R., Eidem, T. R., & Rey, S. S. (2004). Release of methane from a volcanic basin

as a mechanism for initial Eocene global warming. *Nature*, *429*(6991), 538–542. https://doi.org/10.1038/nature02575

Szatmari, P., & Milani, E. J. (2016). Tectonic control of the oil-rich large igneous-carbonate-salt province of the South Atlantic rift. *Marine and Petroleum Geology*, *77*, 567–596. https://doi.org/10.1016/j.marpetgeo.2016.06.004

Terra, G., Spadini, A., & França, A. (2010). Classificação de rochas carbonáticas aplicável às bacias sedimentares brasileiras. *B. Geoci. Petrobras*, *v. 18*(n. 1), 9–29.

Wright, V. P., & Barnett, A. J. (2015). An abiotic model for the development of textures in some South Atlantic early Cretaceous lacustrine carbonates. *Geological Society Special Publication*, *418*(1), 209–219. https://doi.org/10.1144/SP418.3

Wu, X., & Hale, D. (2015). 3D seismic image processing for unconformities. *GEOPHYSICS*.

Wuenschel P.C. (1960). SEISMOGRAM SYNTHESIS INCLUDING MULTIPLES AND TRANSMISSION COEFFICIENTS. *GEOPHYSICS*, *25(1)*, 106–129.

Zalan, P. (2016, April 3). Five kilometers of Paleozoic sediments beneath the pre-salt of Santos basin. *Search and Discovery Article #10915 (2017)*. https://doi.org/10.1190/ice2016-6365881.1

Zalán, P., Rodriguez, K., & Cvetkovic, M. (2019, August 18). Extraordinary Remaining Potential in the Pre-Salt of Santos Basin. *Sixteenth International Congress of the Brazilian Geophysical Society*. https://doi.org/10.22564/16cisbgf2019.128

Zalán, P. V. (2015). Similarities and Differences between Magma-Poor and Volcanic Passive Margins – Applications to the Brazilian Marginal Basins . *Fourteenth International Congress of the Brazilian Geophysical Society*.

Zalán, P. v, do Carmo Severino, M. G., Augusto Rigoti, C., Portugal Magnavita, L., Alberto Bach de Oliveira, J., & Roessler Vianna, A. (2011). An Entirely New 3D-View of the Crustal and Mantle Structure of a South Atlantic

Passive Margin-Santos, Campos and Espírito Santo Basins, Brazil*. *Search and Discovery Article #30177 (2011)*, *30177*.

Zhao, J., José, M., Oliveira, R., Zhao, J., Ren, K., Leonardo, C. ;, Oliveira, C., Carmo, I. O., Rancan, C. C., & Deng, Q. (2019). Fault Activity and its Influences on Distribution of Igneous Rocks in Libra Block, Santos Basin: Semi-Quantitative to Quantitative Assessment of Fault Activity Based on High-Resolution 3D Seismic Data. *Offshore Technology Conference Brasil*.